University of Stuttgart
Germany

Mixed-Dimensional Modeling of Flow in Porous Media

Samuel Burbulla

Mixed-Dimensional Modeling of Flow in Porous Media

Von der Fakultät Mathematik und Physik sowie
dem Stuttgarter Zentrum für Simulationswissenschaft
an der Universität Stuttgart zur Erlangung der Würde
eines Doktors der Naturwissenschaften (Dr. rer. nat.)
genehmigte Abhandlung

vorgelegt von

Samuel Burbulla

aus Reutlingen

Hauptberichter:	Prof. Dr. Christian Rohde
Mitberichter:	Prof. Dr. Peter Bastian (Ruprecht-Karls-Universität Heidelberg)
Mitberichterin:	Associate Professor Dr. Anna Scotti (MOX Politecnico di Milano)

Tag der mündlichen Prüfung: 20. Dezember 2022

Institut für Angewandte Analysis und Numerische Simulation
Universität Stuttgart

2023

Acknowledgements
Funded by the Deutsche Forschungsgemeinschaft (DFG, German Research Foundation) – Project Number 327154368 – SFB 1313.

Contents

Abstract

Modeling flow in dynamically fracturing porous media is of high interest for a wide range of natural and technical applications, for instance, geothermal energy production or carbon capture and storage. In this work, we present new mixed-dimensional models for flow in porous media including fractures with time- and space-dependent geometries. The models are implemented using our new grid implementation Dune-MMesh which is tailored for the discretization of mixed-dimensional partial differential equations with fully conforming interface of codimension one. First, we propose a mixed-dimensional model for capillarity-free two-phase flow in dynamically fracturing porous media. The model is discretized by a fully conforming finite-volume moving-mesh algorithm that explicitly tracks the fracture geometry. Further, generalizing an earlier model for single-phase flow in fractured porous media, we derive a dimensionally reduced model including spatially varying apertures. In several numerical examples, using a mixed-dimensional discontinuous Galerkin discretization, the model demonstrates significant improvements for curvilinear fracture geometries. Finally, we propose a mixed-dimensional phase-field model for fracture propagation in poro-elastic media combining discrete fracture and phase-field modeling approaches. The corresponding discontinuous Galerkin discretization tracks the fracture geometry by adding facets to the fracture triangulation according to the phase-field indicator and is validated with results known from literature.

Zusammenfassung

Die Modellierung der Strömung in dynamisch aufbrechenden porösen Medien ist für eine Vielzahl natürlicher und technischer Anwendungen von großem Interesse, z. B. für die geothermische Energieerzeugung oder die Speicherung von CO_2 im Untergrund. In dieser Arbeit stellen wir neue gemischt-dimensionale Modelle für Strömungen in porösen Medien vor, die Risse mit zeit- und raumabhängigen Geometrien enthalten. Die Modelle werden unter Verwendung unserer neuen Gitterimplementierung Dune-MMesh implementiert, die für die Diskretisierung von gemischt-dimensionalen partiellen Differentialgleichungen mit vollständig konformen Grenzflächen von Codimension eins zugeschnitten ist. Zunächst schlagen wir ein gemischt-dimensionales Modell für kapillarfreie Zweiphasenströmungen in dynamisch aufbrechenden porösen Medien vor. Das Modell wird durch einen vollständig konformen Finite-Volumen Algorithmus mit bewegtem Gitter diskretisiert, der die Rissgeometrie explizit verfolgt. Darüber hinaus leiten wir in Verallgemeinerung eines früheren Modells für einphasige Strömung in geklüfteten porösen Medien ein dimensionsreduziertes Modell her, das räumlich variierende Öffnungsweiten einbezieht. In mehreren numerischen Beispielen, bei denen eine gemischt-dimensionale diskontinuierliche Galerkin-Diskretisierung verwendet wird, zeigt das Modell signifikante Verbesserungen für kurvenförmige Rissgeometrien. Schließlich schlagen wir ein gemischt-dimensionales Phasenfeldmodell für die Rissausbreitung in poro-elastischen Medien vor, das diskrete Riss- und Phasenfeldmodellierungsansätze kombiniert. Die zugehörige diskontinuierliche Galerkin-Diskretisierung verfolgt die Rissgeometrie entsprechend dem Phasenfeldindikator durch das Hinzufügen von Kanten zur Triangulation des Risses und wird mit aus der Literatur bekannten Ergebnissen validiert.

1 Introduction

1.1 Motivation

In several physical and environmental processes that concern multi-phase flows, biological systems, and geophysical phenomena, important physical phenomena occur along thin physical interfaces. In the context of subsurface engineering, many applications and issues are strongly influenced, if not dominated, by physical interfaces like thin heterogeneities or fractures. Groundwater flow, geothermal energy production, enhanced oil recovery, carbon sequestration or nuclear waste disposal are strongly influenced by geologically or artificially induced fractures. As more specific example, fracture propagation plays a significant role in the exploitation of geothermal energy resources. Indeed, layers of hot rock in the subsurface are not far below the earth's surface, but they cannot be exploited because of the rock formation low permeability. For instance, the Cooper Basin in Australia contains hot granite rocks in just 3.5 km depth, with temperatures up to 240 °C. One approach to increase the permeability of the rock is to create an Enhanced Geothermal System (EGS) by pumping high-pressure cold water down an injection well into the rock, cf. Figure 1.1. This technique would increase the permeability of the formation by creating an engineered fracture network and could make the production of such renewable energies economically feasible.

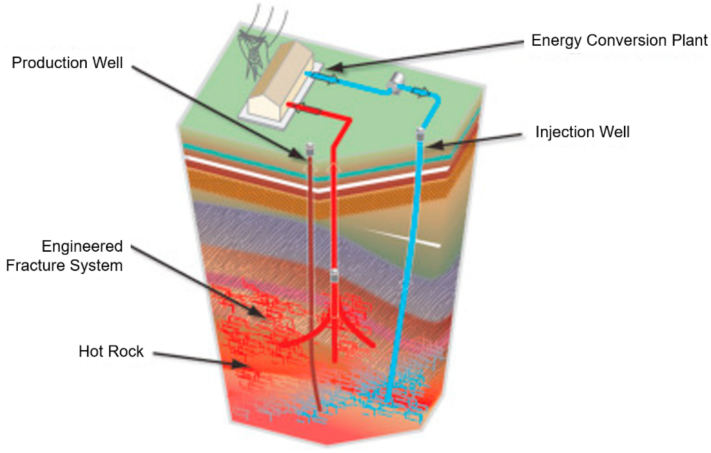

Figure 1.1: Enhanced Geothermal System [56].

In order to understand the ongoing processes, to make predictions and estimate risks, it is crucial to construct mathematical and numerical models of these systems, and to develop efficient numerical schemes that solve the corresponding mathematical models in a feasible amount of time.

1.2 Modeling Fractures in Porous Media

Almost every porous medium formation in the subsurface contains fractures or thin heterogeneities. The interaction between the dynamics of multi-phase flows in porous media and propagating fractures is of paramount interest for the understanding of these systems' behavior. Fractures can serve either as conduits or barriers for fluid flow depending on their detailed geometrical and hydrological properties. For the fundamentals on fracture modeling in porous media we refer to, e.g., [1, 12, 62].

In this thesis, we target at problems whose fracture configurations do not allow to represent them implicitly by an effective single- or multi-continuum model. Rather we consider dominant fractures which must be kept explicit in the mathematical description of the process at the macroscopic Darcy scale. However, in this full-dimensional approach, fractures result in geometric objects with an extreme length-to-width ratio, which is challenging for any direct numerical approach. Various numerical methods based on fundamentally different modeling concepts have been introduced to face this problem. An important class of numerical methods relies on the discrete fracture matrix approach (see [51], and [13, 14] for recent surveys) where fractures are considered as lower-dimensional manifolds. Various approaches to derive such dimensionally reduced models have been proposed in [3, 19, 47, 50]. In this way, the discrete fracture matrix approach leads to a reduced computational effort and less geometrical issues, especially when dealing with very thin fractures. Furthermore, it can be useful to have an explicit representation of the fracture geometry, either if the fracture network is equipped with its own flow model, or its geometry becomes an unknown of the problem itself as in fracture propagation. Notably, the approach leads to mixed-dimensional models.

One of the first numerical methods developed in the realm of discrete fracture matrix ideas is the embedded discrete fracture method (EDFM). These methods employ two different (non-conforming) meshes for the fractures and the bulk porous medium domain [49, 67] and applies finite volumes. Another non-conforming discretization based on the finite element method is the extended finite element method (XFEM) that employs an enriched ansatz space encoding the fracture geometry (see, e.g., [31] or [33, 45] in a more general context). These non-conforming discretizations have the advantage to be independent of the background porous medium grid geometry, but the coupling of the discrete solutions in the bulk porous medium and in the fractures is more complicated to realize.

On the other hand, in conforming methods, the discretizations are easier coupled and it is straightforward to equip the resulting lower-dimensional fracture

domain with some flow model and a numerical discretization technique which accounts for coupling with the bulk. Of course, the construction of the fracture and bulk meshes looses the flexibility of the non-conforming approach. Starting from [4, 51] there has been a rapid development of the numerical modeling based on conforming finite element, finite volume and finite difference techniques. In the case of saturated single-phase flow we refer to [10, 16, 63]. For what concerns the coupling with other processes, [19] deals with poro-elastic media, [3, 59] with two-phase flows, and [33] with reactive flows, to mention just a few. Moreover, we refer to [8] for the formal derivation of a reduced-dimensional model for reactive flows, and [54, 55, 57] for the mathematically rigorous approach for unsaturated flow and reactive transport. A recently published work derives a mixed-dimensional discrete fracture-matrix model, including fracture intersections, of flow and thermal transport in fractured thermo-poroelastic media [65]. This model is also extended to the case of fracture propagation with fracture growth along existing cell faces [66]. Up to now, we mainly addressed work on single-phase flow models. The modeling and numerics have also been extended to two-phase flow in fractured porous media. For different model formulations (pressure-related or fractional flow) and regimes (saturated and unsaturated) we can refer to the work in [2, 18, 32, 37, 43, 59]. To derive reduced models, in [47, 50] homogenization techniques have been proposed for a wide range of settings.

Some approaches for modeling of fractures in porous media employ phase-field representations of the fractures (see, e.g., [17, 40]). These approaches introduce a phase-field variable that represents the fracture by a smooth indicator function. The phase-field function is used to alter the physical properties of the medium like permeability, and thus influences the flow process in the fractured porous medium. All complexity is shifted from the geometry into the model, and therefore, any standard finite element discretization can be applied for discretization. Phase-field models are generally used for modeling fracture propagation as they are capable of capturing general fracture network geometries. In particular, in contrast to discrete fracture models, it is not necessary to explicitly know and discretize the fracture network. However, phase-field models are compu-

Figure 1.2: Fractures in porous media.

tationally rather expensive because a sufficient grid resolution is needed to resolve the phase-field gradient. For this reason, one usually resorts to local mesh adaptation.

In this work, we will propose new mixed-dimensional models based on the discrete fracture matrix approach for single- or two-phase flow in porous media. We will follow a fully conforming discretization approach on the basis of finite volume and discontinuous Galerkin discretizations. Ultimately, we couple our mixed-dimensional flow models with a phase-field model in order to study fracture propagation. Let us start with a general description of some mathematical models for flow in porous media.

1.3 Mathematical Models

In this section, we describe the fundamental mathematical models for flow in porous media that are used in this work. We start with incompressible single-phase flow on the Darcy scale. Then, we consider convection-dominated two-

phase flow in porous media, and finally present the quasi-static Biot's equations for linear poro-elasticity.

1.3.1 Single-Phase Flow

The following model describes the steady-state flow of an incompressible fluid through a porous medium, also called single-phase flow. It consists of Darcy's law and mass conservation and is formulated in terms of homogenized quantities on the Darcy scale, see [41]. Let $\Omega \subset \mathbb{R}^n, n \in \{2, 3\}$, be an open and bounded set which is assumed to be filled with porous media. Then, single-phase flow in Ω can be described by

$$\begin{aligned} \operatorname{div}(\mathbf{v}) &= q, \\ \mathbf{v} &= -\frac{\mathbf{K}}{\eta}\nabla p \qquad \text{in } \Omega. \end{aligned} \tag{1.1}$$

In (1.1), $p : \Omega \to \mathbb{R}$ [Pa] is the pressure, $\mathbf{v} : \Omega \to \mathbb{R}^n$ [m s^{-1}] is the Darcy velocity and $q : \Omega \to \mathbb{R}$ [s^{-1}] denotes a source term. The permeability matrix $\mathbf{K} = \mathbf{K}(\mathbf{x}) \in \mathbb{R}^{n\times n}$ [m^2] is a symmetric and positive-definite tensor and $\eta \in \mathbb{R}^{>0}$ [Pa s] is the dynamic viscosity of the fluid. The system (1.1) is well-posed with appropriate boundary conditions as elliptic system of partial differential equations.

1.3.2 Two-Phase Flow

The time-dependent dynamics of two incompressible and immiscible fluids in porous media can be described by the subsequent model. It can be derived by generalized, phase-dependent Darcy's laws and the according continuity equations for each of the phases, denoted as wetting (w) and non-wetting (nw)

phase. For some end time $T > 0$, the two fluids are governed by a system of partial differential equations given by

$$\begin{aligned} (\phi\rho_\alpha S_\alpha)_t + \operatorname{div}(\rho_\alpha \mathbf{v}_\alpha) &= \rho_\alpha q_\alpha, \\ \mathbf{v}_\alpha &= -\lambda_\alpha(S_\alpha)\mathbf{K}(\nabla p_\alpha - \rho_\alpha \mathbf{g}) \end{aligned} \qquad \text{in } \Omega \times (0,T), \quad \alpha \in \{w, nw\}. \tag{1.2}$$

Here, $S_\alpha : \Omega\times(0,T) \to [0,1]\,[-]$ is the saturation of the α-phase, $p_\alpha : \Omega\times(0,T) \to \mathbb{R}$ [Pa] is the corresponding phase pressure and $\mathbf{v}_\alpha : \Omega \times (0,T) \to \mathbb{R}^n\,[\mathrm{m\,s^{-1}}]$ is the phase velocity. The subscript t denotes the time derivative. The system (1.2) can be closed by the relations

$$S_w + S_{nw} = 1, \tag{1.3a}$$

$$p_{nw} = p_w. \tag{1.3b}$$

The second closing relation corresponds to the assumption of zero capillary pressure and allows us to derive a hyperbolic-elliptic system of equations, see (1.4) below. The given parameters in (1.2)-(1.3b) are the porosity $\phi = \phi(\mathbf{x}) > \delta\,[-]$ for all $\mathbf{x} \in \Omega$ with some $\delta \in (0,1]$, the constant phase density $\rho_\alpha \in \mathbb{R}^{>0}\,[\mathrm{kg\,m^{-3}}]$, and the gravitational acceleration vector $\mathbf{g} \in \mathbb{R}^n\,[\mathrm{m\,s^{-2}}]$. The phase mobility function is given by

$$\lambda_\alpha(S_\alpha) = \frac{k_\alpha(S_\alpha)}{\eta_\alpha},$$

where $k_\alpha = k_\alpha(S_w)$ is the smooth monotone relative permeability with $k_w(0) = 0, k_w(1) = 1$ and $k_{nw}(0) = 1, k_{nw}(1) = 0$. For each phase α, the dynamic viscosity is denoted by η_α [Pa s]. The function $q_\alpha : \Omega\times(0,T) \to \mathbb{R}\,[\mathrm{s^{-1}}]$ is a phase-dependent source or sink term.

The two-phase flow model (1.2) reduces to the single-phase system (1.1) for the wetting phase if $S_w \equiv 1$ or, respectively, for the non-wetting phase if $S_{nw} \equiv 1$.

1.3.2.1 Fractional Flow Formulation

From (1.2) we can derive the equivalent fractional flow formulation. This formulation is more appropriate for convection-dominated or capillarity-free regimes because the system decomposes into equations of elliptic and hyperbolic type.

Let us select the wetting phase saturation $S = S_w$ eliminating S_{nw} by using (1.3a). Introducing the fractional-flow function

$$f(S) := \frac{\lambda_w(S)}{\lambda(S)},$$

with $\lambda(S) := \lambda_w(S) + \lambda_{nw}(S)$ being the total mobility, we can reformulate the two-phase flow system (1.2)-(1.3b). For zero capillary pressure it is equivalent to

$$\begin{aligned} (\phi S)_t + \operatorname{div} \mathbf{F}(S, \mathbf{v}) &= q_w, \\ \mathbf{v} + \lambda(S)\mathbf{K}(\nabla p - G(S)\mathbf{g}) &= \mathbf{0}, \qquad \text{in } \Omega \times (0, T). \\ \operatorname{div}(\mathbf{v}) &= q_w + q_{nw} \end{aligned} \tag{1.4}$$

In (1.4), the flux function $\mathbf{F} = \mathbf{F}(S, \mathbf{v})$ is defined as

$$\mathbf{F}(S, \mathbf{v}) := f(S)\mathbf{v} - f(S)\lambda_{nw}(S)\mathbf{K}(\rho_{nw} - \rho_w)\mathbf{g}.$$

The term $G(S)$ is given by

$$G(S) := \frac{\lambda_w(S)\rho_w + \lambda_{nw}(S)\rho_{nw}}{\lambda(S)}.$$

In (1.4), the unknowns are the (wetting phase) saturation $S = S_w$, the total velocity $\mathbf{v} = \mathbf{v}_w + \mathbf{v}_{nw}$ and the global pressure $p = p_{nw} = p_w$. Note that S_{nw} is computable from (1.3a).

It remains to state initial conditions for S and appropriate boundary conditions for S and $\mathbf{v}$ or p. Let us emphasize that the capillarity-free model (1.4) is of mixed hyperbolic-elliptic type admitting discontinuous fronts as weak solutions for the saturation equation. The well-posedness of the model is only known for the case that $\mathbf{v}$ is sufficiently regular, but this regularity does not hold for general mobility functions.

1.3.3 Linear Poro-Elasticity

An extension of the single-phase model (1.1) describing viscous fluid flow including elastic solid deformation leads to Biot's model of linear poro-elasticity. The quasi-static Biot equations describe the behavior of an elastic porous medium that is fully saturated with an incompressible fluid. They can be stated by the subsequent system of partial differential equations which are derived in [15]. The pressure $p : \Omega \times (0,T) \to \mathbb{R}$ and displacement $\mathbf{u} : \Omega \times (0,T) \to \mathbb{R}^n$ in the porous matrix Ω satisfy

$$\begin{aligned} -\operatorname{div}(\sigma(\mathbf{u}) - \alpha p \mathbf{I}) &= 0, \\ \left(\frac{p}{M} + \alpha \operatorname{div}(\mathbf{u})\right)_t - \operatorname{div}\left(\frac{\mathbf{K}}{\eta}\nabla p\right) &= q \end{aligned} \qquad \text{in } \Omega \times (0,T). \tag{1.5}$$

The first equation in (1.5) expresses static equilibrium in the absence of external loads and the second governs the fluid mass conservation in a deformable porous medium. Indeed, the fluid content in the porous medium depends on pressure through the Biot modulus and the volumetric deformation of the solid. In system (1.5), we have Biot's coefficient $\alpha \in [0,1]$ and the Biot modulus $M > 0$ [Pa]. The matrix $\mathbf{I} \in \mathbb{R}^{n\times n}$ denotes the unit matrix.

We define the effective stress tensor σ in (1.5) using Hooke's law, i.e.,

$$\sigma(\mathbf{u}) := \lambda \operatorname{div}(\mathbf{u})\mathbf{I} + 2\mu\epsilon(\mathbf{u}),$$

where the symmetric gradient is

$$\epsilon(\mathbf{u}) := \frac{1}{2}\big(\nabla\mathbf{u} + (\nabla\mathbf{u})^\top\big),$$

and $\mu, \lambda > 0$ [$\mathrm{N\,m^{-2}}$] are Lamé's parameters, cf. [15]. Given the elasticity modulus E and Poisson's ratio ν, one can express Lamé's parameters also as

$$\lambda = \frac{E\nu}{(1+\nu)(1-2\nu)} \quad \text{and} \quad \mu = \frac{E}{2(1+\nu)}.$$

The effective stress and the total stress $\sigma_{\text{total}}(\mathbf{u})$ are linked by

$$\sigma_{\text{total}}(\mathbf{u}) = \sigma(\mathbf{u}) - \alpha p\mathbf{I},$$

which is the stress that is used for the static equilibrium in Equation (1.5).

Biot's equations for linear poro-elasticity (1.5) constitute a strongly coupled system of partial differential equations of parabolic-elliptic type. The well-posedness of this model has been carried out in [64].

1.4 Outline

This work is structured as follows. In the beginning, we present our specialized grid module Dune-MMesh that has been tailored for the flexible implementation of mixed-dimensional models on moving meshes in Chapter 2. Then, we proceed to study the modeling of flow in fracturing porous media. Starting from incompressible two-phase flow in porous media we present a corresponding mixed-dimensional model with prescribed fracture propagation in Chapter 3. For fractures with non-constant aperture, we developed a reduced model that takes into account the fracture geometry, and we proposed a corresponding mixed-dimensional discontinuous Galerkin method, see Chapter 4. In Chapter 5, a phase-field model is integrated to compute the evolution of the fractures. This leads to a new mixed-dimensional phase-field model for fracture propagation in poro-elastic media. Finally, the work concludes with a summary of the results in Chapter 6.

The Dune Grid Implementation Dune-MMesh

2

The content of the following chapter led to the publication ”Dune-MMesh: The Dune Grid Module for Moving Interfaces” in ”Journal of Open Source Software” [21]. All source code of the presented grid implementation Dune-MMesh is open source and can be accessed in public repositories[1][2]. I came up with the presented ideas, implemented the source code and performed the computations of the numerical examples.

2.1 Introduction

In this chapter, we present our Dune grid module Dune-MMesh that is tailored to numerical applications with moving physical interfaces. This software is the basis for the implementation of the discretization schemes in the subsequent chapters.

Dune-MMesh is an implementation of the well-developed Dune [11] grid interface and is well-suited for the numerical discretization of partial differential equations (PDEs). The package wraps two and three dimensional CGAL [68] triangulations in high-level Dune objects like intersections of grid entities, index

[1]https://gitlab.dune-project.org/samuel.burbulla/dune-mmesh
[2]https://github.com/samuelburbulla/dune-mmesh

and id sets and geometry transformations. Furthermore, it exports a predefined set of facets as a separate interface grid. In two dimensions, the arbitrary movement of vertices is enhanced with a re-meshing algorithm that implements non-hierarchical adaptation procedures. Besides the adaptation of the triangulation, Dune-MMesh provides the necessary data structures to adapt discrete functions defined on the bulk grid or the interface. This adaptation approach complements existing grid implementations within the Dune framework that strictly rely on hierarchical adaptation. Various examples in Python have been implemented based on the discretization module Dune-Fem [27] that demonstrate the versatile applicability of Dune-MMesh. Due to the ability to handle custom PDEs in their weak from written in Unified Form Language (UFL) and the mesh adaptation capabilities, we believe Dune-MMesh provides a useful tool for solving mixed-dimensional PDEs on moving interfaces that arise from various fields of modeling.

Dune-MMesh has been made available via PyPI (the Python Package Index[3]) in order to make installation as easy as possible. For this purpose, we implemented packaging support for the Dune framework configuring and compiling the C++ backend during package installation. In fact, the new possibility to install, e.g., Dune-Fem via *pip install dune-fem* is a great simplification for setting up a new installation of Dune.

2.2 Concepts

In this section, we introduce the concepts behind the implementation of Dune-MMesh. The main concepts are the CGAL triangulation wrapper, the interface grid implementation and the non-hierarchic adaptation functionality.

[3]https://pypi.org

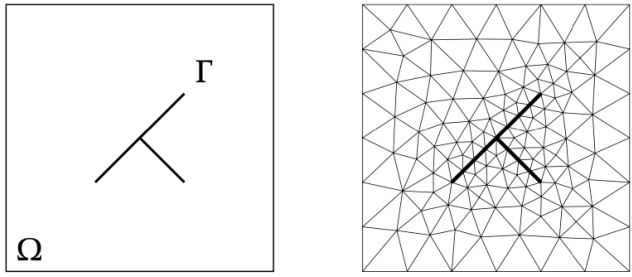

Figure 2.1: Left: The domain Ω contains a T-shaped interface Γ. Right: An example for a triangulation of Ω conforming to the interface Γ.

2.2.1 Triangulation

Let us start with the definition of a triangulation of a domain. We consider a (polytopal) domain $\Omega \subset \mathbb{R}^n$ that includes an $(n-1)$-dimensional hypersurface $\Gamma \subset \Omega$, also called interface.

Definition 2.1 (Triangulation)**:** *A triangulation of Ω is given by a family of n-dimensional simplexes $\mathcal{T}$ and a family of $(n-1)$-dimensional simplexes $\mathcal{F}$ satisfying the following properties:*

- $\overline{\bigcup_{K\in\mathcal{T}} K} = \overline{\Omega}$,
- $\forall K \in \mathcal{T}\ \exists \mathcal{F}_K \subset \mathcal{F} \ : \ \partial K = \bigcup_{F\in\mathcal{F}_K} \overline{F}$,
- $\forall K, K' \in \mathcal{T} \ : \ $ *either* $K = K'$ *or* $|K \cap K'| = 0$ *or* $\exists F \in \mathcal{F}$ *with* $\overline{K} \cap \overline{K'} = F$.

Here, we use the notation $|\cdot|$ for the corresponding Lebesgue measure.

Definition 2.1 likewise defines the triangulation of the interface hypersurface Γ with some families of $(n-1)$-, $(n-2)$-dimensional simplexes $\mathcal{T}_\Gamma$ and $\mathcal{F}_\Gamma$. In the next step, we combine bulk triangulation and interface triangulation by clarifying what we mean by a triangulation that is conforming to the interface.

Definition 2.2 (Conforming to the interface)**:** *We call a triangulation* $(\mathscr{T}, \mathscr{F})$ *of* Ω *conforming to an interface triangulation* $(\mathscr{T}_\Gamma, \mathscr{F}_\Gamma)$ *of* Γ *if the following condition holds:*

$$\forall K_\Gamma \in \mathscr{T}_\Gamma \; \exists F \in \mathscr{F} \; : \; \overline{K}_\Gamma = \overline{F}.$$

If a triangulation $(\mathscr{T}, \mathscr{F})$ is conforming to the interface triangulation $(\mathscr{T}_\Gamma, \mathscr{F}_\Gamma)$, a subset $\mathscr{F}^\Gamma \subset \mathscr{F}$ of facets can be identified with $\mathscr{T}_\Gamma$. In order to distinguish, we introduce the notation $\mathscr{F}^I := \mathscr{F} \setminus \mathscr{F}^\Gamma$ to denote inner, non-interface facets. Moreover, let us denote $\mathscr{F}(K)$ as the set of facets of cell K.

An example of a triangulation conforming to the interface is visualized in Figure 2.1 (right). Note that we also consider interfaces Γ that consist of a set of lower-dimensional hypersurfaces and, therefore, network junctions can occur. Dune-MMesh implements such triangulations with conforming network interfaces for dimensions $n = 2, 3$, and we will describe in the following, how this is implemented.

2.2.2 CGAL Wrapper

In its core, Dune-MMesh is a wrapper of CGAL triangulations in $\mathbb{R}^n, n = 2, 3$, that implements the Dune grid interface. A CGAL triangulation is a set of simplicial cells and vertices where each cell gives access to its $n + 1$ incident vertices and cells. Facets are not explicitly represented: a facet is given by the pair of a cell c and an index i and has two implicit representations. For $n = 3$, edges are represented by triples of a cell c and two indices i and j that indicate the two vertices of the edge.

In order to match the Dune grid reference cell numbering we apply an index mapping, cf. Figure 2.2. Here, the edges of tetrahedrons are equipped with indices according to the Dune reference element numbering. Dune intersections, i.e., intersections of mesh entities of codimension 0 with a neighboring element

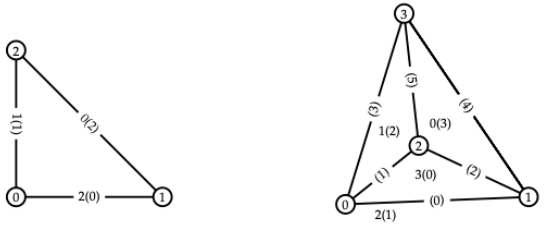

Figure 2.2: CGAL representation of cells and corresponding Dune numbering in brackets. The vertex numbering is maintained, facets are renumbered, and the edges of tetrahedrons are equipped with indices according to the Dune reference element numbering.

or with the domain boundary, can directly be represented by CGAL cell-index representations of facets which are already equipped with an orientation. The index and id sets of the Dune grid interface are realized by consecutive numbering of cells and vertices. Each higher dimensional entity id is defined by the sorted tuple of corresponding vertex ids. The geometrical representation of entities that are not intrinsically CGAL entities (e.g., codimensions $1, \dots, n-1$) is made unique by an ascending order of vertex ids. In addition, this prevents twists of intersections and we obtain a twist free grid implementation. Various iterators of CGAL triangulations can directly be used to construct the Dune grid range generators. Additional (non-standard Dune) iterators have been added, e.g., iterating over incident cells of a vertex.

In the next section, we describe how we extended the wrapping of the CGAL triangulation to export a set of facets as interface grid.

2.2.3 Interface Grid

Consider a domain $\Omega \subset \mathbb{R}^n, n \in \{2, 3\}$, that includes a $(n-1)$-dimensional interface $\Gamma \subset \Omega$, as depicted in Figure 2.1 (left), cf. Definition 2.2. We assume the

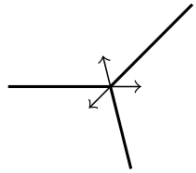

Figure 2.3: The outer normal vectors at junctions are independent of the neighbor.

domain is triangulated by a triangulation $\mathcal{T}$ that is conforming to the interface triangulation $\mathcal{T}_\Gamma$ of Γ. Dune-MMesh features a second implementation of the Dune grid interface that represents the interface triangulation $\mathcal{T}_\Gamma$. The interface grid can be used like any other Dune grid as it implements all necessary functionality. For this purpose, facets are marked as belonging to the interface. Usually, this is done when parsing the mesh file, but it can also be adding grid facets to the interface manually. A codim-0 entity of the interface grid (an entity with the same dimension as the interface grid) is represented by a CGAL cell-index pair, as it is used for the codim-1 entities (having one dimension lower than the grid) of the wrapper implementation. This representation is made unique by taking the representation where the cell has the lower index. This side is also considered as the positive side of the facet. All sub-entity objects can be generated by this representation using the right indexing of vertices. The geometry representations and element ids are made unique by ascending order of vertex ids as it is done in the full-dimensional wrapper implementation. For iteration of the interface grid's entities, `finite_edges_iterator` or `finite_facets_iterator` is used skipping all facets not belonging to the interface. Intersections and neighbor relationships are obtained by CGAL's `incident_edges` or `incident_facets` iterators. Index sets are implemented by mappings of vertex ids. The interface grid also supports networks. For this purpose, the intersection iterator returns all common intersections with adjacent cells. Note that this can be more than one for a single codim-1 sub-entity. However, the intersection outer normal is

always independent of the neighbor entity, cf. Figure 2.3.

Each bulk grid intersection can be identified as belonging to the interface or not. It is also possible to convert bulk intersections to interface grid elements and vice versa as the underlying representation is the same. When converting an interface grid entity to a bulk intersection, Dune-MMesh returns the intersection as seen from the cell with the lower index.

2.3 Moving Mesh

Most interface driven-problems have time-dependent interfaces $\Gamma = \Gamma(t)$. Therefore, Dune-MMesh features capabilities of moving and re-meshing in two spatial dimensions.

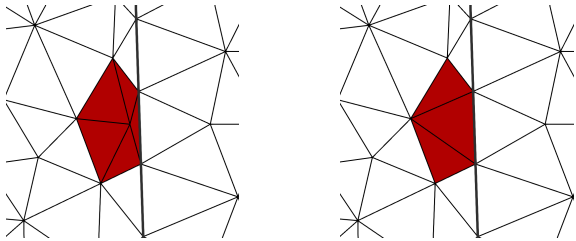

Figure 2.4: The movement of the interface can lead a degeneration of the triangulation. Therefore, Dune-MMesh provides the necessary procedures for adaptation.

2.3.1 Moving Vertices

We assume that movement is given by a shift of interface (or all) vertices, e.g., as in Figure 2.5. This movement can be performed by simply changing the coordinates

of the vertices. Dune-MMesh provides the method `moveInterface(shifts)` that takes as input a vector of shift coordinates indexed by interface vertex indices. A second `method moveVertices(shifts)` is available for moving all vertices of the triangulation indexed by bulk vertex indices. Note that moving vertices might lead to degeneration of the triangulation, cf. Figure 2.4. To prevent this, i.e., to ensure cells have positive volume, Dune-MMesh is equipped with re-meshing routines that will be described in the subsequent.

2.3.2 Adaptation

Adaptation in Dune is hierarchical by definition as it is useful for the adaptation of discrete functions. Whenever a grid element is supposed to be refined, it is split into smaller cells belonging to a higher level of the grid hierarchy. If all children in the highest refinement level of a grid element are supposed to be coarsened, the children cells are merged to form a parent cell one level lower. The procedure is as follows.

1. Mark: Grid cells are marked for coarsening or refinement.

2. Adapt: The cells are modified and discrete functions are restricted or prolongated.

In Dune-MMesh, due to the moving mesh, non-hierarchic adaptation is unavoidable. However, we will try to follow the general Dune approach and separate the adaptation into two stages.

Stage 1: Mark
Dune-MMesh provides utility functions to mark cells in expectation of a movement of the interface or regarding to their current geometrical properties. As an example, in Figure 2.5, two cells are marked for refinement because their edge length will exceed the desired maximum edge length. One cell is marked for coarsening because it would have negative volume after moving the interface and, therefore, it has to be removed. To be more precise,

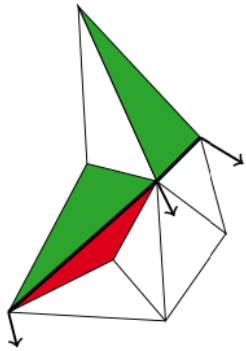

Figure 2.5: Moving the interface is performed by shifting vertices. The cells are marked either for refinement (green) or coarsening (red).

the method `ensureInterfaceMovement(shifts)` (respectively `ensureVertexMovement(shifts)`) can be called to prepare Dune-MMesh for moving the vertices. The routine takes the vertex shifts as argument and marks presumably degenerate cells for coarsening. Hence, they will be somehow removed during adaptation.

A second method for marking elements is `markElements()`. This method uses a default indicator that marks elements depending on their current geometrical properties. This indicator considers primarily maximal and minimal edge length and aims at an objective edge length between $h_{\min}$ and $h_{\max}$. If an edge is longer (shorter) than maximum length $h_{\max}$, the cell will be marked for refinement (coarsening). The minimal and maximal edge lengths are initialized automatically when constructing a mesh by determining the range of edge lengths occurring the grid. Additionally, if the ratio of longest to shortest edge is larger than 4, the cell is marked for coarsening. The number 4 stems from the fact that we will use bisection, and a triangle where two edges are longer then $h_{\max}$ should not be split into smaller triangles where an edge is shorter than $h_{\min}$. Finally, a maximal

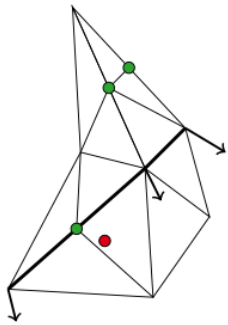

Figure 2.6: Marking cells leads to insertion and removal of vertices. In this example, the green points will be inserted to cut the long edges and the red one will be removed to ensure positive cell volume.

radius ratio is taken into account to remove badly shaped cells. Coarsening has always priority before refinement because refinement would not remove the badly shaped cells.

Remark that `markElements()` also checks the elements of the interface grid. Therefore, the interface will be refined and coarsened as well if edges of the interface get too long or too short. As an alternative to the built in methods, it is possible to use a proprietary procedure marking cells manually, or insert and remove vertices directly.

Stage 2: Adapt
After marking cells an adapt routine performs the actual adaptation process. The adaptation is performed by insertion and removal of points. In each cell that is marked for refinement, we bisect the longest edge, cf. Figure 2.6 for an example. In all cells marked for coarsening, one vertex is removed. Here, we choose the vertex incident to the shortest edges of the cell, but first remove non-interface and non-boundary vertices. When a vertex is removed, the resulting star-shaped hole is re-triangulated with respect to the interface. For the purpose

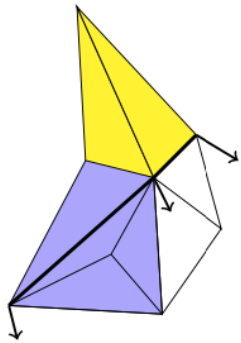

Figure 2.7: Two connected components are created (purple and yellow) that consist of cells of the initial triangulation and are used for the projection of discrete functions.

of projection, we introduce the concept of *connected components*. A connected components is defined as the minimal set of cells from the triangulation before adaptation covering the same connected area as a set of cells in the triangulation after adaptation. The easiest representatives of these connected components are the incident cells when bisecting an edge and the incident cells to a vertex that is removed. However, we have to combine overlapping sets of these representatives.

In Figure 2.7, the two connected components of our adaptation example are visualized in purple and yellow as sets of cells of the initial triangulation. For a conservative projection of discrete functions we compute a cut-set triangulation which enables evaluation with agglomerated quadrature rules on triangles. Here, we prolong from an old cell onto such a cut triangle and restrict onto the new cell, cf. Figure 2.8. This whole projection is performed under the hood and just requires the use of the callback adaptation in Dune-Fem. On the interface grid, we use a similar concept that enables projection of discrete functions on the interface.

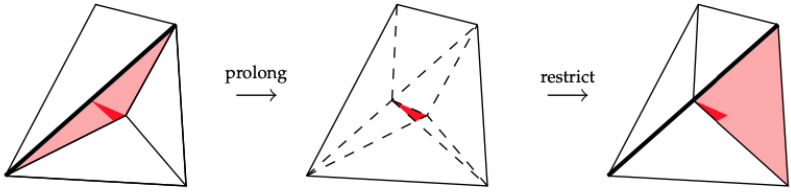

Figure 2.8: Non-hierarchic projection with cut-set triangulation.

2.4 Mixed-Dimensional Problems

2.4.1 Trace and Skeleton

Dune-MMesh exports both traces of bulk discrete functions on the interface and skeleton representations of interface discrete functions on bulk edges. The trace is a discrete function on the interface grid that evaluates a given bulk discrete function. It can be restricted to both sides of the interface and can be used in UFL forms. Analogously, the skeleton function is a discrete function that returns an interface discrete function on interface bulk facets. Both `trace` and `skeleton` can be used to couple bulk and interface problems. Such couplings occur, e.g., in mixed-dimensional PDEs. For an example of such a coupling, see Section 2.5.1 below.

2.4.2 Coupled Solve

We provide two auxiliary functions to solve bulk and interface schemes in a coupled way. The method `iterativeSolve` uses an iterative solution strategy which alternately solves both schemes until the two norm between two iterates is below an objective tolerance. A second auxiliary function `monolithicSolve` solves bulk and interface scheme coupled monolithically. A Newton method is

implemented by assembling the underlying Jacobian matrix where the coupling Jacobian blocks are evaluated by finite differences.

2.5 Examples

We implemented a few examples to demonstrate how Dune-MMesh can be used in different contexts. All examples can be found on the documentation page of Dune-MMesh.[4] The documentation page is considered as part of the accompanying publication [21] and features a description of the installation of Dune-MMesh, a class documentation of the C++ and Python API and a presentation of the main concepts with examples.

2.5.1 Solving a Mixed-Dimensional Problem

To give a brief insight into the technical implementation, we want to present one code example that uses the Python interface of Dune-MMesh. We consider a domain that contains a T-shaped interface Γ embedded in domain $\Omega = (0, 1)^2$, cf. Figure 2.1 (left).

The grid creation from a mesh file works as follows.

```
from dune.grid import reader
from dune.mmesh import mmesh
gridView = mmesh((reader.gmsh, "grids/tjunction.msh"), 2)
igridView = gridView.hierarchicalGrid.interfaceGrid
```

[4] https://dune-mmesh.readthedocs.io

On domain Ω, we solve a mixed-dimensional Poisson equation

$$\begin{aligned} -\Delta u &= 0 && \text{in } \Omega, \\ -\Delta u_\Gamma + [\![\nabla u \cdot \mathbf{n}]\!] &= q && \text{in } \Gamma, \\ u &= 0 && \text{on } \partial\Omega, \end{aligned}$$

with the coupling

$$\nabla u \cdot \mathbf{n} = \frac{u_\Gamma - u}{\omega} \qquad \text{along } \Gamma$$

for some $\omega > 0$. Note that the jump operator $[\![\cdot]\!]$ above denotes the difference of the values of the trace of $\nabla u \cdot \mathbf{n}$ on both sides of the interfacce Γ and will be defined in more detail in Chapter 4. In this example, we use source term $q = 1$ and $\omega = 10^{-6}$.

A weak formulation of the problem above reads as follows. Find $u \in H_0^1(\Omega)$, $u_\Gamma \in H^1(\Gamma)$ s.t.

$$\begin{aligned} \int_\Omega \nabla u \cdot \nabla v \, dx - \int_\Gamma \frac{u_\Gamma - u}{\omega} \, dS &= 0, \\ \int_\Gamma \nabla u_\Gamma \cdot \nabla v_\Gamma \, dx + \int_\Gamma \frac{u_\Gamma - u}{\omega} \, dS &= \int_\Gamma q v_\Gamma \, dx, \end{aligned}$$

for all corresponding test functions $v \in H_0^1(\Omega)$, $v_\Gamma \in H^1(\Gamma)$.

We employ a (discontinuous) Galerkin discretization for the bulk and interface problem that can be implemented as follows. First, we define (discontinuous) Lagrange function spaces.

```
from ufl import *
from dune.fem.space import lagrange, dglagrange
space = dglagrange(gridView, order=1)
ispace = lagrange(igridView, order=1)
u = TrialFunction(space)
v = TestFunction(space)
```

```
iu = TrialFunction(ispace)
iv = TestFunction(ispace)
uh = space.interpolate(0, name="uh")
iuh = ispace.interpolate(0, name="iuh")
```

Using UFL, we state the problem in its weak form and add the consistency terms.

```
from dune.ufl import Constant
from dune.mmesh import interfaceIndicator
q = Constant(1, name="q")
omega = Constant(1e-6, name="omega")
beta = Constant(1e2, name="beta")
n = FacetNormal(space)
I = interfaceIndicator(igridView)
a = inner(grad(u), grad(v)) * dx
a += beta * inner(jump(u), jump(v)) * (1-I)*dS
a -= dot(dot(avg(grad(u)), n('+')), jump(v)) * (1-I)*dS
a += beta * inner(u - 0, v) * ds
a -= dot(dot(grad(u), n), v) * ds
ia = inner(grad(iu), grad(iv)) * dx
ib = q * iv * dx
```

The coupling between the two problems can be implemented using the trace and skeleton functionality of Dune-MMesh.

```
from dune.mmesh import skeleton, trace
omega = Constant(1e-6, name="omega")
a -= (skeleton(iuh)('+') - u('+')) / omega * v('+') * I*dS
a -= (skeleton(iuh)('-') - u('-')) / omega * v('-') * I*dS
ia += (iu - trace(uh)('+')) / omega * iv * dx
ia += (iu - trace(uh)('-')) / omega * iv * dx
```

The two separate Galerkin schemes can be coupled monolithically with our monolithic solution algorithm.

```
from dune.fem.scheme import galerkin
scheme = galerkin([a == 0])
```

```
ischeme = galerkin([ia == ib])
from dune.mmesh import monolithicSolve
monolithicSolve(schemes=(scheme, ischeme), targets=(uh, iuh))
```

Finally, we can plot the solution of this problem as visualized in Figure 2.9.

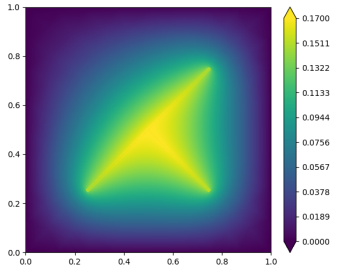

Figure 2.9: The solution of the mixed-dimensional Poisson problem.

Further examples are presented in the following without the corresponding source code, but it is available in full length on the documentation page[5].

2.5.2 Finite-Volume Moving-Mesh Algorithm

In this section, we will present an example of how to move the interface and adapt the mesh. For this purpose, we implement a finite-volume moving-mesh method tracking a discontinuity of the solution in the discretization mesh, cf. [25].

Let us consider the following transport problem.

$$u_t + \operatorname{div} F(u) = 0, \qquad \text{in } \Omega \times (0, T), \tag{2.1}$$

$$u(\cdot, 0) = u_0, \qquad \text{in } \Omega, \tag{2.2}$$

[5]https://dune-mmesh.readthedocs.io/en/latest/examples.html

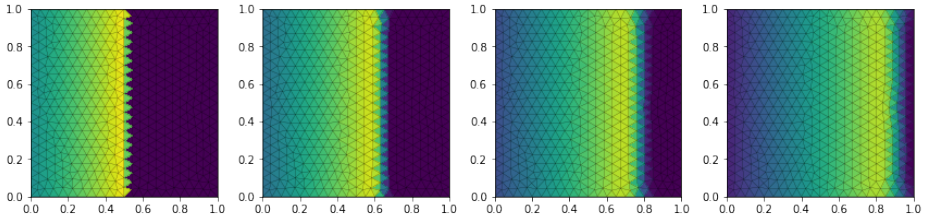

Figure 2.10: Standard finite volume scheme solving the transport equation.

where

$$F(u) = (1,0)^\top u, \tag{2.3}$$

$$u_0(x,y) = (0.5 + x)\chi_{x<0.5}. \tag{2.4}$$

Further, the interface is supposed to move with the transport speed in f, i.e., $\mathbf{m} = (1,0)^\top$.

We use a finite-volume moving-mesh method to keep the discontinuity sharp. It can be formulated in a weak form as

$$\int_\Omega (u^{n+1}|\det(\Psi)| - u^n)v\,dx + \Delta t \int_{\mathscr{F}} \big(g(u^n,\mathbf{n}) - h(u^n,\mathbf{n})\big)[\![v]\!]\,dS = 0 \tag{2.5}$$

where $\Psi := x + \Delta t\mathbf{n}$, and $\mathbf{s}$ is a linear interpolation of the interface's vertex movement $\mathbf{m}$ on the bulk triangulation. The numerical fluxes $g(u,\mathbf{n})$ and $h(u,\mathbf{n})$ are assumed to be consistent with the flux functions $F(u)\cdot\mathbf{n}$ and $u\mathbf{s}\cdot\mathbf{n}$, respectively. Here, we choose an upwind flux.

For reference, we run the finite volume scheme without moving the interface, cf. Figure 2.10. The standard finite volume method shows the expected numerical diffusion and leads to a runtime of 0.905 seconds with an L^2 error $\|u - u_{exact}\|_{L^2}$ of 0.107 at $T = 0.4$.

In contrast, the result of the finite-volume moving-mesh method can be found

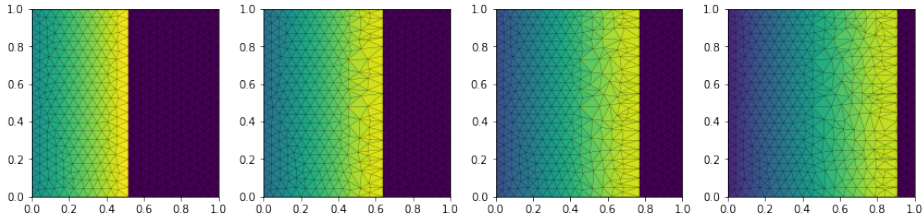

Figure 2.11: Finite-volume moving-mesh method to track a discontinuity.

in Figure 2.11. The edges at the discontinuity have been moved by the same speed as the transport and the mesh has been adapted accordingly. Here, we measure a runtime of 2.235 seconds with an L^2 error of 0.019. Remarkably, in this specific example, the runtime has increased by a factor of 2.47x, while the error has improved by a factor of 5.59x at the same time. Both errors have also been plotted over time, see Figure 2.12.

In our opinion, this example shows that it is worth adapting if one can conserve specific features of the solution.

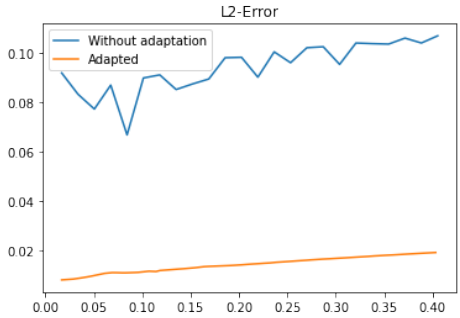

Figure 2.12: Errors of standard finite volume scheme vs. finite-volume moving-mesh method plotted over time.

2.5.3 Mixed-Dimensional Poro-Elasticity

The following example demonstrates the monolithic solving strategy of Dune-MMesh that is useful for strongly coupled mixed-dimensional systems. Let us consider linear Biot equations, cf. (1.5), with an interface Γ considered as thin heterogeneity. Neglecting the time derivative, the problem reads as follows. Find $\mathbf{u}$, p, p_Γ s.t

$$\begin{aligned} -\operatorname{div}(\mathbf{K}\nabla p) &= q, && \text{in } \Omega, \\ -\operatorname{div}(\sigma(\mathbf{u}) - \alpha p\mathbf{I}) &= 0, && \text{in } \Omega, \\ -\operatorname{div}(\mathbf{K}_\Gamma \nabla p_\Gamma) &= q_\Gamma, && \text{in } \Gamma, \end{aligned}$$

where $\sigma(\mathbf{u})$ and all other quantities are defined as in Section 1.3.3. Additionally, $\mathbf{K}_\Gamma$ denotes the permeability of the thin heterogeneity Γ and q_Γ is a corresponding source term. We define coupling conditions between Ω and Γ imposed as interior boundary conditions

$$\begin{aligned} p &= p_\Gamma, \\ (\sigma(\mathbf{u}) - \alpha p\mathbf{I})\mathbf{n} &= -p_\Gamma \mathbf{n}, \end{aligned} \qquad \text{on } \Gamma,$$

that describe pressure continuity and normal stress balance. Let us consider a T-shaped interface Γ embedded in $\Omega = (0,1)^2$, as sketched in Figure 2.1 (left). We choose $\lambda = 1.2$, $\mu = 0.8$, $\alpha = 1$, $\mathbf{K} = \operatorname{diag}((10^{-4}, 10^{-6})^\top)$, $K_\Gamma = \mathbf{I}$, $q = 0$, and $q_\Gamma = 10^{-6}$. Further, concerning boundary conditions, we impose zero displacement on top and bottom, and zero pressure at left and right boundaries of the domain Ω. We impose natural boundary conditions else, in particular, at the tips of the lower-dimensional domain Γ.

We implement a mixed-dimensional Interior Penalty Discontinuous Galerkin (IPDG) scheme that directly includes the discontinuity of the displacement along the interface Γ. Remarkably, the scheme also already incorporates the flux balance at junctions of the interface. Including penalty and consistency terms,

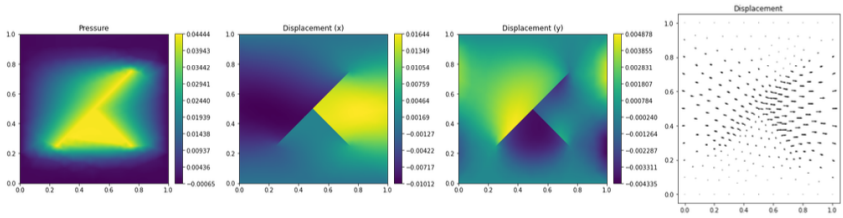

Figure 2.13: Mixed-dimensional model of poro-elasticity with a T-shaped heterogeneity.

we have the following weak form of the problem

$$
\begin{aligned}
A(\mathbf{u}, p; \mathbf{v}, \varphi) \coloneqq & \int_\Omega (\mathbf{K}\nabla p)\cdot\nabla\varphi \, dx - \int_\Omega q\varphi \, dx \\
& + \int_{\mathscr{F}\setminus\mathscr{F}_\Gamma} \frac{\beta}{h}[\![p]\!][\![\varphi]\!] - \{\!\{\mathbf{K}\nabla p\cdot\mathbf{n}\}\!\}[\![\varphi]\!] \, dS \\
& + \int_{\mathscr{F}_D^p} \frac{\beta}{h}(p - p_D)\varphi - \mathbf{K}\nabla p\cdot\mathbf{n}\varphi \, ds \\
& + \int_{\mathscr{F}_\Gamma} \frac{\beta}{h}(p^+ - p_\Gamma)\varphi^+ - \mathbf{K}\nabla p^+\cdot\mathbf{n}^+\varphi^+ \, dS \\
& + \int_{\mathscr{F}_\Gamma} \frac{\beta}{h}(p^- - p_\Gamma)\varphi^- - \mathbf{K}\nabla p^-\cdot\mathbf{n}^-\varphi^- \, dS \\
& + \int_\Omega (\sigma(\mathbf{u}) - \alpha p\mathbf{I}) : \epsilon(\mathbf{v}) \, dx \\
& + \int_{\mathscr{F}\setminus\mathscr{F}_\Gamma} \frac{\beta}{h}[\![\mathbf{u}]\!][\![\mathbf{v}]\!] - (\{\!\{\sigma(\mathbf{u}) - \alpha p\mathbf{I}\}\!\}\cdot\mathbf{n})\cdot[\![\mathbf{v}]\!] \, dS \\
& + \int_{\mathscr{F}_D^u} \frac{\beta}{h}(\mathbf{u} - \mathbf{u}_D)\cdot\mathbf{v} - ((\sigma(\mathbf{u}) - \alpha p\mathbf{I})\cdot\mathbf{n})\cdot\mathbf{v} \, ds \\
& - \int_{\mathscr{F}_\Gamma} -p_\Gamma(\mathbf{v}^+\cdot\mathbf{n}^+) - p_\Gamma(\mathbf{v}^-\cdot\mathbf{n}^-) \, dS
\end{aligned}
$$

and on the interface

$$A_\Gamma(p_\Gamma;\varphi_\Gamma) \coloneqq \int_\Gamma (\mathbf{K}_\Gamma \nabla p_\Gamma)\cdot\nabla\varphi_\Gamma - q_\Gamma\varphi_\Gamma + \beta(p_\Gamma - \{\!\{p\}\!\})\varphi_\Gamma \, dx + \int_{\mathscr{F}^\Gamma} \frac{\beta}{h_\Gamma}[\![p_\Gamma]\!][\![\varphi_\Gamma]\!] - \{\!\{\mathbf{K}_\Gamma\nabla p_\Gamma\cdot\mathbf{n}_\Gamma\}\!\}[\![\varphi_\Gamma]\!]\, dS.$$

This weak form has a similar representation in its implementation using UFL, and Dune-MMesh adds the functionality to couple the two domain-specific sub-problems. For the full implementation with all technical details we refer to the documentation page.

The solution of the example is visualized in Figure 2.13. It shows the displacement jump at the interface and how the pressure is distributed according to the anisotropic permeability. In our opinion, this example shows that this discretization approach is well-suited for this kind of problem. It has a general way to be written in weak form, its locally conservative and consistent for anisotropic tensors, and it already captures discontinuities at the interface as well as junctions.

2.5.4 Two-Phase Navier–Stokes with Rising Bubble

Let us consider incompressible Navier–Stokes equations with two immiscible phases and surface tension. In fact, with Dune-MMesh, it is possible to track the sharp interface between the two phases explicitly using the adaptation facilities.

A domain $\Omega \subset \mathbb{R}^n$ is assumed to be separated into two phases $\Omega_i(t), i = 1, 2$, by a sharp interface $\Gamma(t)$, $t \in (0, T)$. The problem investigated reads as follows, cf. [58].

Find (u, p) and $\Gamma(t)$ s.t.

$$\begin{aligned}
\rho u_t + \nabla \cdot (\rho u \otimes u) + \nabla \cdot \mathbb{T}(u,p) &= 0, && \text{in } \Omega_i(t), && i = 1,2,\\
\nabla \cdot u &= 0, && \text{in } \Omega_i(t), && i = 1,2,\\
[\![p]\!] &= \sigma \boldsymbol{\kappa} \cdot n, && \text{on } \Gamma(t), &&\\
[\![u]\!] &= 0, && \text{on } \Gamma(t), &&\\
\dot{x} &= u, && x \in \Gamma(t), &&\\
u(0) &= u_0, && \text{in } \Omega_i(0), && i = 1,2,\\
\Gamma(0) &= \Gamma_0, &&&&
\end{aligned}$$

for $t \in (0, T)$. The stress tensor $\mathbb{T}(u, p)$ is given by

$$\mathbb{T}(u,p) := p\mathbf{I} - \mu(\nabla u + (\nabla u)^\top)),$$

$\mu_i, i = 1, 2$, are the dynamic viscosities, $\rho_i, i = 1, 2$, the densities of the two phases, σ is the surface tension and $\boldsymbol{\kappa}$ denotes the signed mean curvature of the interface times its normal.

The mean curvature times normal $\boldsymbol{\kappa}$ can be computed by an auxiliary problem on the interface. Find $\boldsymbol{\kappa} \in \left[H^1(\Gamma(t))\right]^n$ s.t.

$$\int_{\Gamma(t)} \boldsymbol{\kappa} \cdot \boldsymbol{\phi} + \nabla_\Gamma \mathbf{x} \cdot \nabla_\Gamma \boldsymbol{\phi} \, d\mathbf{x} = 0, \qquad \text{in } \Gamma(t), \quad \forall \boldsymbol{\phi} \in \left[H^1(\Gamma(t))\right]^n,$$

compare, e.g., Equation (2.10) in [26], where ∇_Γ denotes the tangential gradient. It is easy to solve this problem on the interface numerically, as Dune-MMesh exports the interface as separate interface grid. Note that our overall numerical solution strategy follows a splitting scheme similar to the one presented in [34].

As example, we compute the dynamics of a rising bubble for $n = 2$. We start with a circular Ω_1 with radius $r = 0.25$ centered in $(0.5, 0.5)$ embedded in the domain $\Omega = (0, 1) \times (0, 2)$. The physical parameters are chosen as $\mu_1 = \mu_2 = 1$,

$\rho_1 = 1$, $\rho_2 = 2$, $\sigma = 0.03$ and $T = 12$, and we set no-slip boundary conditions everywhere on $\partial\Omega$. Four snapshots of the resulting time series are plotted in Figure 2.14. One can clearly observe how the bubble develops the typical shape of a rising bubble.

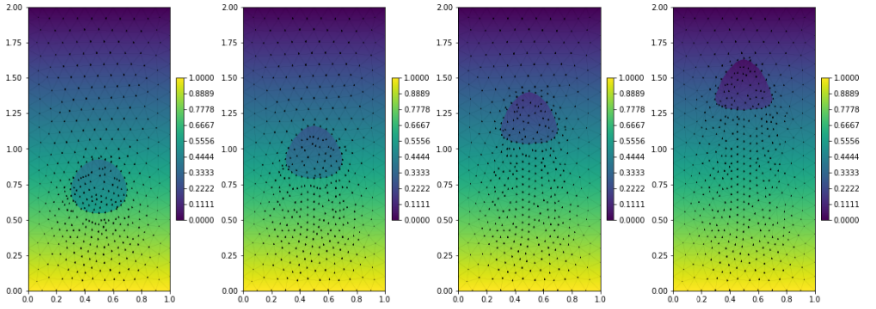

Figure 2.14: Rising bubble in the two-phase Navier–Stokes example for $t \in \{0, 4, 8, 12\}$.

2.6 Computations for Flow in Fractured Porous Media

In the subsequent chapters of this work, we will describe how we applied Dune-MMesh to some newly derived mixed-dimensional flow problems in fractured porous media. Besides this, we used the method described in Chapter 3 to perform numerical simulations for single-phase and two-phase flow in porous medium with static fracture geometries. We will describe the results of these computations shortly in this section.

As a first example, we present a results from a benchmark study for flow in three-dimensional fractured porous media [13]. Our circum-centered finite volume discretization has shown a remarkable agreement with the results of the other methods. In particular, it performed much better than the classical cell-centered

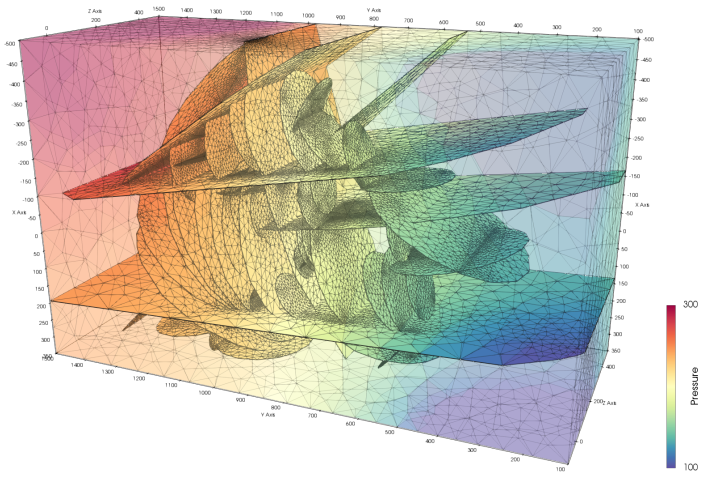

Figure 2.15: Verification benchmarks for single-phase flow in three-dimensional porous media. Visualized is the pressure distribution for Case 4, the field case. [13]

TPFA approximation while having exactly the same number of degrees of freedom. The result of the fourth test case of this benchmark study is visualized in Figure 2.15 and shows the pressure distribution within the field-case fractured porous medium.

During a summer school project within the SFB 1313 graduate school in 2019, we coupled our solver to an inversion algorithm that determined the fracture positions from a few pressure measurements. One of the pressure distributions in the two-dimensional porous medium that has been used in this project is visualized in Figure 2.16 (left). A comparison of our method to another model using a phase-field representation of the fractures have shown good agreement between the two.

We used the same fracture network geometry as in the previous example to

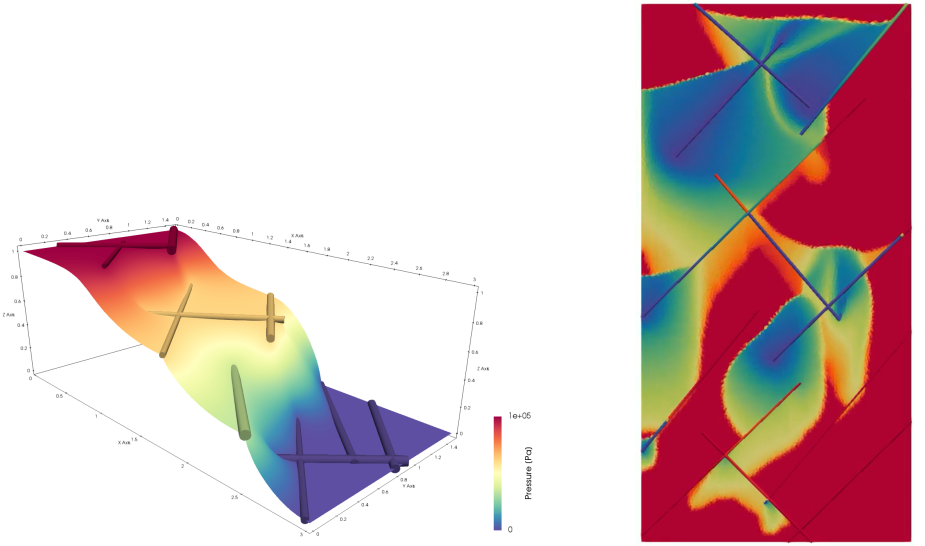

Figure 2.16: Left: Pressure distribution in a two-dimensional fractured porous medium that has been used during a summer school project. Right: Gravity-driven two-phase flow in fracture network with several sharp saturation fronts.

compute gravity-driven two-phase flow scenarios [23]. The result displayed in Figure 2.16 (right) clearly shows the sharp saturation fronts between the two phases. This example suggests that two-phase flow patterns in fractured porous media can become very complex.

Two-phase Flow in Dynamically Fracturing Porous Media

3

The content of the following chapter led to the publication ”A finite-volume moving-mesh method for two-phase flow in dynamically fracturing porous media” in ”Journal of Computational Physics” [24]. All source code and the data of the simulation results have been published via DaRUS [20]. I worked out the theoretical details, implemented the numerical scheme and performed the numerical calculations.

In this chapter, we derive a mathematical model governing capillarity-free two-phase flow in fractured porous media that extends previous models as it accounts for fractures with space- and time-dependent aperture. The numerical scheme presented in this chapter has been implemented using Dune-MMesh, cf. Chapter 2, and makes extensive use of its interface grid implementation and the adaptation capabilities modeling the propagating fractures as a moving interface.

3.1 Introduction

Let us consider capillarity-free two-phase flow regimes in fractured porous media at the Darcy scale. Neglecting capillary forces, we obtain mixed hyperbolic-elliptic models for saturation and total pressure. As a consequence there can

be discontinuous saturation fronts as weak solutions that travel through the porous medium interacting with the fractures. Notably, we assume that the two-phase flow model can be applied for the bulk domain as well as for the fracture domain. This applies for fractures filled with debris but might also be a valid ansatz if one accounts in an effective way for the surface roughness induced by the fracture walls. In passing we note that this ansatz implies that the porous media parameters like porosity or intrinsic permeability might vary discontinuously when crossing the interface between bulk and fracture domain. We focus on dynamically changing fracture geometries. The approach starts from an initially given full-dimensional fracture domain that is characterized by an aperture function along its longitudinal extension. The fracture might evolve in time and also the aperture function might change dynamically. Notably, we assume these motions to be given for all times and not to be part of the problem unknowns.

In Section 3.2, we define the geometrical setting of our model. As we are interested in convection-dominated regimes we pass to the fractional-flow formulation of the parabolic two-phase system. Then, we follow the discrete fracture matrix ideas of [51] and apply transversal averaging for the fracture domains. This derivation leads us to a new mixed-dimensional model that governs two-phase flow in fracturing porous media (see equations (3.25)-(3.27) in Section 3.3). If we consider a static fracture geometry, this reduced discrete fracture model coincides with the two-phase flow models as in, e.g., [32, 43]. To close the reduced discrete fracture model we need to make some assumptions on the coupling conditions regarding their physical meaning, see Section 3.2.
The main contribution of this chapter is a conforming numerical method for the solution of the reduced discrete fracture model (3.25)-(3.27). It is presented in Section 3.4. As discussed before, the major challenge of the conforming ansatz is the mesh design which becomes even more complicated for time-dependent fracture changes. We believe that the additional effort to construct conforming meshes, including re-meshing, pays off in the easy coupling to the lower-dimensional grid. Extending an approach from [25], we propose a moving-mesh algorithm that preserves a conforming mesh at any point in time. Moreover, the (discrete)

codimension-1 fracture manifold is represented for all times as a connected union of facets of the mesh. Based on the moving mesh one can then construct a finite volume method for the saturation equation. By constructing an appropriate geometric flux that accounts for the exact mesh movement, the method remains mass conservative even with moving meshes. The elliptic equation for the total pressure is solved by a tailored two-point flux discretization. It is consistent for isotropic permeability tensors and does not require the construction of any cell stencils that change and might be expensive during re-meshing. The complete finite-volume moving-mesh (FVMM) algorithm is summarized in Section 3.4.4.

We report on a series of numerical simulations using the FVMM algorithm. Preliminary results for static fracture networks have already been published in [23]. To validate the reduced discrete fracture model (3.25)-(3.27), we compare numerical results for the original two-phase model (with full-dimensional fracture and bulk domains) with results of the discrete fracture approach using the FVMM algorithm. For elliptically shaped fractures that grow and are compressed in time both numerical results match almost perfectly. Then, we proceed to two- and three-dimensional examples that illustrate the interaction of infiltrating saturation fronts with a prescribed set of fractures.

3.2 Derivation of the Discrete Fracture Model

In the context of fractured porous media, it is a wide-spread approach to model sufficiently thin fractures as lower-dimensional manifolds. By doing so, we implicitly assume that the original fracture's aperture is clearly separated from the pore scale. Then, it is justified that the fracture persists on the Darcy scale instead of being homogenized. For single-phase flow, such discrete fracture models have been initially proposed in [43, 51] using transversal averaging. We suggest a mathematical model to describe two-phase flow in dynamically fracturing porous media on the basis of a discrete-fracture network approach

and using the fractional-flow formulation. Up to our knowledge, a two-phase flow model with the dynamic change of the fracture geometry has not been investigated before in the context of discrete fracture networks. The work on two-phase flow discussed in Section 3.1 refers to static fracture networks.

For $t \in [0,T]$, let us consider a connected open set $\Omega_f(t) \subset \Omega$, representing the original fracture. We suppose that the domain Ω is partitioned according to $\Omega = \left(\bar{\Omega}_b(t) \cup \bar{\Omega}_f(t)\right)^\circ$ (see Figure 3.1 for a sketch of the geometry), where $\Omega_b(t)$ denotes the bulk porous medium with $\Omega_b(t) \cap \Omega_f(t) = \emptyset$ and $^\circ$ denotes the interior of the set. We define space-time sets by

$$\Omega_b^t := \Big\{\Omega_b(t) \times \{t\} \mid t \in [0,T]\Big\},$$

$$\Omega_f^t := \Big\{\Omega_f(t) \times \{t\} \mid t \in [0,T]\Big\}.$$

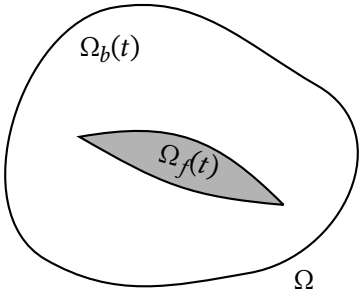

Figure 3.1: Sketch of the domain Ω divided into a bulk porous medium $\Omega_b(t)$ and the fracture region $\Omega_f(t)$.

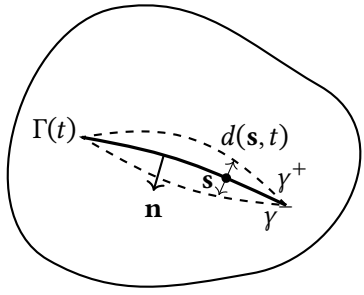

Figure 3.2: The fracture domain $\Omega_f(t)$ is replaced by the lower-dimensional interface $\Gamma(t)$ and aperture $d = d(\mathbf{s},t)$.

As in Section 1.3.2, we assume to have incompressible and immiscible two-phase flow in the porous medium for both the bulk domain $\Omega_b(t)$ and the fracture domain $\Omega_f(t)$. However, the porosities ϕ, ϕ^f, the intrinsic permeabilities $\mathbf{K}, \mathbf{K}^f$ and

the relative permeabilities k_α, k_α^f might differ. Within fractures a porous media (two-phase) flow occurs, for instance, if they are filled with debris. Effective porous media flow can also be induced by wall roughness. We assume that this behavior can be characterized by the physical properties of a porous medium in the fracture.

Adapting the fractional-flow formulation from (1.4), the fluid unknowns $S^i : \Omega_i^t \to [0,1]$, $p^i : \Omega_i^t \to \mathbb{R}$ and $\mathbf{v}^i : \Omega_i^t \to \mathbb{R}^n$ are governed by

$$\begin{aligned} (\phi^i S^i)_t + \operatorname{div} \mathbf{F}^i(S^i, \mathbf{v}^i) &= q_w, \\ \mathbf{v}_i + \lambda^i(S^i)\mathbf{K}^i(\nabla p^i - G^i(S^i)\mathbf{g}) &= 0, \qquad \text{in } \Omega_i^t, \quad i \in \{b, f\}, \\ \operatorname{div}(\mathbf{v}^i) &= q_w + q_{nw} \end{aligned} \tag{3.1}$$

with the coupling conditions

$$\begin{aligned} \mathbf{F}^b(S^b, \mathbf{v}^b) \cdot \mathbf{n} &= \mathbf{F}^f(S^f, \mathbf{v}^f) \cdot \mathbf{n}, \\ p^b &= p^f, \\ \mathbf{v}^b \cdot \mathbf{n} &= \mathbf{v}^f \cdot \mathbf{n} \end{aligned} \tag{3.2}$$

on $\partial\Omega_b(t) \cap \partial\Omega_f(t)$ for all $t \in (0,T)$ and $i \in \{b, f\}$. Here, the functions G, λ and F are defined as in Section 1.3.2.

The physical quantities, such as ϕ and $\mathbf{K}$, are expected to differ in the two subdomains and, therefore, are indicated by the superscript $i \in \{b, f\}$. Appropriate initial data and boundary conditions have to be added.

The coupling conditions (3.2) express mass conservation and pressure equilibrium and are a natural choice such that problem (3.1) is equivalent to the problem (1.4), defined on the complete domain $\Omega = \Omega_b \cup \Omega_f$.

Now, let us replace the fracture $\Omega_f(t)$ by a centered $(n-1)$-dimensional hypersurface $\Gamma(t)$ and a given aperture function $d \in \mathscr{C}^1(\Gamma^t)$ with $d > 0$, where

$\Gamma^t := \{\Gamma(t) \times \{t\} \mid t \in (0,T)\}$, cf. Figure 3.2. For this, we assume a simple geometrical setup with no junctions, where the fracture can be represented as a hypersurface and a smooth function defined on $\Gamma(t)$ that models the aperture.

We shall orient the two sides of the surface. To do so, we choose a normal $\mathbf{n} = \mathbf{n}(\mathbf{s},t) \in \mathcal{S}^{n-1}$ in $\mathbf{s} \in \Gamma(t)$ where $\mathcal{S}^{n-1}$ denotes the set of vectors in $\mathbb{R}^n$ with unit length. The sides will be denoted by positive (+) and negative (-) signs where $\mathbf{n}$ is assumed to point to the negative side. Later, we will also use the notation $\mathbf{n} = \mathbf{n}^+ = -\mathbf{n}^-$.

Let us consider for $i \in \{b, f\}$ smooth solutions S^i, p^i and $\mathbf{v}^i$ of system (3.1) that satisfy the coupling conditions (3.2). Then, the reduced model is obtained by averaging along the line segments

$$L(\mathbf{s},t) := \left\{ \mathbf{s} + \frac{r}{2}\mathbf{n} \;\middle|\; r \in \big(-d(\mathbf{s},t), d(\mathbf{s},t)\big) \right\} \subset \Omega^f(t), \qquad \mathbf{s} \in \Gamma(t), t \in (0,T). \quad (3.3)$$

We introduce the projection matrices $\mathbf{N} := \mathbf{n} \otimes \mathbf{n} \in \mathbb{R}^{n\times n}$ and $\mathbf{T} := \mathbf{I} - \mathbf{N} \in \mathbb{R}^{n\times n}$. For differentiable functions $\varphi : \Gamma \to \mathbb{R}$ and $\psi : \Gamma \to \mathbb{R}^n$ we define tangential and normal derivations by

$$\nabla_\tau \varphi := \mathbf{T}\nabla\bar{\varphi}, \qquad \mathrm{div}_\tau \psi := \mathrm{div}(\mathbf{T}\bar{\psi}), \qquad \mathrm{div}_{\mathbf{n}} \psi := \mathrm{div}(\mathbf{N}\bar{\psi}),$$

where $\bar{\varphi}, \bar{\psi}$ are extensions of φ, ψ to an open set in $\mathbb{R}^n$ including Γ. To each $\mathbf{s} \in \Gamma(t)$ we associate the fracture boundary points

$$\mathbf{s}_\pm(\mathbf{s},t) := \mathbf{s} \mp \frac{1}{2} d(\mathbf{s},t)\mathbf{n}. \quad (3.4)$$

We refer to Figure 3.2 for illustration. Denote by

$$\gamma_\pm(t) := \left\{ \mathbf{s}_\pm(\mathbf{s},t) \;\middle|\; \mathbf{s} \in \Gamma \right\}$$

the boundary surfaces on each side of the fracture (see Figure 3.2). Using this notation, we define for some function $\varphi : \Omega_b \to \mathbb{R}$ the bulk traces

$$\varphi^{\pm} = \varphi^{\pm}(\mathbf{s}) := \lim_{\substack{\varepsilon \to 0 \\ \varepsilon > 0}} \varphi(\mathbf{s}_{\pm} \mp \varepsilon \mathbf{n}),$$

and the jump and mean values by

$$[\![\varphi]\!] := \varphi^{+} - \varphi^{-} \qquad \text{and} \qquad \{\varphi\} := \frac{\varphi^{+} + \varphi^{-}}{2}.$$

We proceed and define reduced quantities on $\Gamma(t)$ by averaging along the line segments $L(\mathbf{s}, t)$ from (3.3), namely

$$\mathbf{v}_{\Gamma}(\mathbf{s}, t) := \frac{1}{d(\mathbf{s}, t)} \int_{L(\mathbf{s},t)} \mathbf{T}\mathbf{v}^{f}(\cdot, t)\, d\mathbf{x} = \frac{1}{d(\mathbf{s}, t)} \int_{-d(\mathbf{s},t)}^{d(\mathbf{s},t)} \mathbf{T}\mathbf{v}^{f}\Big(\mathbf{s} + \frac{r}{2}\mathbf{n}, t\Big)\, dr, \tag{3.5}$$

$$S_{\Gamma}(\mathbf{s}, t) := \frac{1}{d(\mathbf{s}, t)} \int_{L(\mathbf{s},t)} S^{f}(\cdot, t)\, d\mathbf{x} = \frac{1}{d(\mathbf{s}, t)} \int_{-d(\mathbf{s},t)}^{d(\mathbf{s},t)} S^{f}\Big(\mathbf{s} + \frac{r}{2}\mathbf{n}, t\Big)\, dr, \tag{3.6}$$

$$p_{\Gamma}(\mathbf{s}, t) := \frac{1}{d(\mathbf{s}, t)} \int_{L(\mathbf{s},t)} p^{f}(\cdot, t)\, d\mathbf{x} = \frac{1}{d(\mathbf{s}, t)} \int_{-d(\mathbf{s},t)}^{d(\mathbf{s},t)} p^{f}\Big(\mathbf{s} + \frac{r}{2}\mathbf{n}, t\Big)\, dr. \tag{3.7}$$

From now on, we assume that ϕ^{f} and $\mathbf{K}^{f}$ are constant along each $L(\mathbf{s}, t)$. For smooth functions k_{α}^{f}, f^{f} and G^{f}, that may depend non-linearly on S^{f}, we approximate all evaluation in $L(\mathbf{s}, t)$ by the evaluation at the mean quantity, i.e.,

$$k_{\alpha}^{f}(S^{f}(\mathbf{x}, t)) = k_{\alpha}^{f}(S_{\Gamma}(\mathbf{s}, t)) + O(\bar{d}), \tag{3.8}$$

$$f^{f}(S^{f}(\mathbf{x}, t)) = f^{f}(S_{\Gamma}(\mathbf{s}, t)) + O(\bar{d}), \tag{3.9}$$

$$G^{f}(S^{f}(\mathbf{x}, t)) = G^{f}(S_{\Gamma}(\mathbf{s}, t)) + O(\bar{d}), \tag{3.10}$$

for all $\mathbf{x} \in L(\mathbf{s}, t)$ where $\bar{d} := \max\{d(\mathbf{s}, t) \mid t \in [0, T], \mathbf{s} \in \Gamma(t)\}$. For the simple affine choice for k_{α}^{f}, i.e., $k_{w}^{f}(S^{f}) = S^{f}$ and $k_{nw}^{f}(S^{f}) = 1 - S^{f}$, the $O(\bar{d})$-term in conditions

(3.8)-(3.10) vanishes. In general, relations (3.8)-(3.10) hold if S_f is regular enough. The regularity of S_f depends on the used models, we refer for rigorous results to [50] and [54, 55, 57], albeit for different models.
The further derivation of our model is based on the following results.

Lemma 3.1: *For $\varphi \in \mathscr{C}^1(\Omega_f^t)$ and $\psi \in \mathscr{C}^1(\Omega_f^t)^n$ we have for all $(\mathbf{s},t) \in \Gamma^t$ the identities*

(I.)

$$\begin{aligned}\int_{L(\mathbf{s},t)} \frac{d}{dt}\varphi(\mathbf{x},t)\,d\mathbf{x} = \frac{d}{dt}\big(d(\mathbf{s},t)\varphi_\Gamma(\mathbf{s},t)\big)\\ - \frac{\partial_t d(\mathbf{s},t)}{2}\Big(\varphi(\mathbf{s},t)|_{\mathbf{s}=\mathbf{s}_-} + \varphi(\mathbf{s},t)|_{\mathbf{s}=\mathbf{s}_+}\Big)\end{aligned} \tag{3.11}$$

(II.)

$$\begin{aligned}\int_{L(\mathbf{s},t)} \operatorname{div}\psi(\mathbf{x},t)\,d\mathbf{x} = \operatorname{div}_\tau\big(d(\mathbf{s},t)\psi_\Gamma(\mathbf{s},t)\big)\\ - \frac{\nabla_\tau d(\mathbf{s},t)}{2}\cdot\Big(\mathbf{T}\psi(\mathbf{s},t)|_{\mathbf{s}=\mathbf{s}_-} + \mathbf{T}\psi(\mathbf{s},t)|_{\mathbf{s}=\mathbf{s}_+}\Big)\\ - \Big(\psi(\mathbf{s},t)|_{\mathbf{s}=\mathbf{s}_+} - \psi(\mathbf{s},t)|_{\mathbf{s}=\mathbf{s}_-}\Big)\cdot\mathbf{n}\end{aligned} \tag{3.12}$$

(III.)

$$\begin{aligned}\int_{L(\mathbf{s},t)} \nabla\varphi(\mathbf{x},t)\,d\mathbf{x} = \nabla_\tau\Big(d(\mathbf{s},t)\varphi_\Gamma(\mathbf{s},t)\Big)\\ - \frac{\nabla_\tau d(\mathbf{s},t)}{2}\Big(\varphi(\mathbf{s},t)|_{\mathbf{s}=\mathbf{s}_-} + \varphi(\mathbf{s},t)|_{\mathbf{s}=\mathbf{s}_+}\Big)\end{aligned} \tag{3.13}$$

where $\varphi_\Gamma(\mathbf{s},t) := \frac{1}{d(\mathbf{s},t)}\int_{L(\mathbf{s},t)}\varphi(\mathbf{x},t)\,d\mathbf{x}$ and $\psi_\Gamma(\mathbf{s},t) := \frac{1}{d(\mathbf{s},t)}\int_{L(\mathbf{s},t)}\psi(\mathbf{x},t)\,d\mathbf{x}$.

Proof: The computations for (I.)-(III.) are similar. We provide the proof for (III.) and compute

$$\begin{aligned} d(\mathbf{s},t)\nabla_\tau\varphi_\Gamma(\mathbf{s},t) &= d(\mathbf{s},t)\nabla_\tau\Big(\frac{1}{d(\mathbf{s},t)}\Big)\int_{L(\mathbf{s},t)}\varphi(\mathbf{x},t)\,d\mathbf{x} + \nabla_\tau\Big(\int_{L(\mathbf{s},t)}\varphi(\mathbf{x},t)\,d\mathbf{x}\Big), \\ &= -\frac{\nabla_\tau d(\mathbf{s},t)}{d(\mathbf{s},t)}\int_{L(\mathbf{s},t)}\varphi(\mathbf{x},t)\,d\mathbf{x} + \int_{L(\mathbf{s},t)}\nabla\varphi(\mathbf{x},t)\,d\mathbf{x} \\ &\quad + \frac{\nabla_\tau d(\mathbf{s},t)}{2}\varphi(\mathbf{s},t)|_{\mathbf{s}=\mathbf{s}_-} + \frac{\nabla_\tau d(\mathbf{s},t)}{2}\varphi(\mathbf{s},t)|_{\mathbf{s}=\mathbf{s}_+}, \\ &= -\nabla_\tau d(\mathbf{s},t)\varphi_\Gamma + \int_{L(\mathbf{s},t)}\nabla\varphi(\mathbf{x},t)\,d\mathbf{x} \\ &\quad + \frac{\nabla_\tau d(\mathbf{s},t)}{2}\Big(\varphi(\mathbf{s},t)|_{\mathbf{s}=\mathbf{s}_-} + \varphi(\mathbf{s},t)|_{\mathbf{s}=\mathbf{s}_+}\Big). \end{aligned}$$

Here, we used definition (3.4) and the definition of φ_Γ. Rearranging the terms and using the chain rule results in (3.13). The derivation of the two other identities follows analogously. □

For $\varphi = \phi^f S^f$ and $\psi = \mathbf{v}^f$ equations (3.11) and (3.12) read

$$\begin{aligned} \int_{L(\mathbf{s},t)}\frac{d}{dt}\Big(\phi^f S^f(\mathbf{x},t)\Big)\,d\mathbf{x} &= \frac{d}{dt}\Big(d(\mathbf{s},t)\phi^f S_\Gamma(\mathbf{s},t)\Big) \\ &\quad - \frac{\partial_t d(\mathbf{s},t)}{2}\phi^f\Big(S^f(\mathbf{s},t)|_{\mathbf{s}=\mathbf{s}_-} + S^f(\mathbf{s},t)|_{\mathbf{s}=\mathbf{s}_+}\Big), \end{aligned} \tag{3.14}$$

$$\begin{aligned} \int_{L(\mathbf{s},t)}\operatorname{div}\mathbf{v}^f(\mathbf{x},t)\,d\mathbf{x} &= \operatorname{div}_\tau\Big(d(\mathbf{s},t)\mathbf{v}_\Gamma(\mathbf{s},t)\Big) \\ &\quad - \frac{\nabla_\tau d(\mathbf{s},t)}{2}\cdot\Big(\mathbf{T}\mathbf{v}^f(\mathbf{s},t)|_{\mathbf{s}=\mathbf{s}_-} + \mathbf{T}\mathbf{v}^f(\mathbf{s},t)|_{\mathbf{s}=\mathbf{s}_+}\Big) \\ &\quad - [\![\mathbf{v}\cdot\mathbf{n}]\!]. \end{aligned} \tag{3.15}$$

Here, we used coupling condition (3.2c) to write the jump $[\![\mathbf{v}\cdot\mathbf{n}]\!]$. For $\varphi = p^f$ and

$\psi = \mathbf{F}^f(S^f, \mathbf{v}^f)$, using the approximations (3.8)-(3.10) and coupling conditions (3.2), we can write

$$\int_{L(\mathbf{s},t)} \nabla p^f(\mathbf{x},t)\, d\mathbf{x} = \nabla_\tau\big(d(\mathbf{s},t)p_\Gamma(\mathbf{s},t)\big) - \nabla_\tau d(\mathbf{s},t)\{\!\{p\}\!\} + O(\bar{d}), \tag{3.16}$$

$$\begin{aligned}\int_{L(\mathbf{s},t)} \operatorname{div} \mathbf{F}^f(S^f, \mathbf{v}^f)\, d\mathbf{x} = {} & \operatorname{div}_\tau\Big(d\mathbf{F}^f(S_\Gamma, \mathbf{v}_\Gamma)\Big) \\ & - \frac{\nabla_\tau d}{2} \cdot \Big(\mathbf{TF}^f(S^f, \mathbf{v}^f)|_{\mathbf{s}_-} + \mathbf{TF}^f(S^f, \mathbf{v}^f)|_{\mathbf{s}_+}\Big) \\ & - [\![\mathbf{F}^f(S, \mathbf{v}) \cdot \mathbf{n}]\!] + O(\bar{d}).\end{aligned} \tag{3.17}$$

Now, integrating each equation in (3.1) for $i = f$ along the line segments $L(\mathbf{s},t)$, we obtain a reduced model for the fracture in terms of the unknowns S_Γ, p_Γ and $\mathbf{v}_\Gamma$. Integrating the saturation conservation equation (3.1) for $i = f$ and using (3.14)-(3.17) we obtain

$$\begin{aligned}&\int_{L(\mathbf{s},t)} (\phi^f S^f)_t + \operatorname{div} \mathbf{F}^f(S^f, \mathbf{v}^f)\, d\mathbf{x} \\ &= \Big(d\phi^f S_\Gamma\Big)_t - \frac{\partial_t d(\mathbf{s},t)}{2}\phi^f\Big(S^f(\mathbf{s},t)|_{\mathbf{s}=\mathbf{s}_-} + S^f(\mathbf{s},t)|_{\mathbf{s}=\mathbf{s}_+}\Big) \\ &\quad + \operatorname{div}_\tau\Big(d\mathbf{F}^f(S_\Gamma, \mathbf{v}_\Gamma)\Big) - \frac{\nabla_\tau d}{2} \cdot \Big(\mathbf{TF}^f(S^f, \mathbf{v}^f)|_{\mathbf{s}_-} + \mathbf{TF}^f(S^f, \mathbf{v}^f)|_{\mathbf{s}_+}\Big) \\ &\quad - [\![\mathbf{F}^f(S, \mathbf{v}) \cdot \mathbf{n}]\!] + O(\bar{d}) \\ &= dq_w^\Gamma + O(\bar{d}).\end{aligned} \tag{3.18}$$

For the last line we used

$$q_w^\Gamma := \frac{1}{d(\mathbf{s},t)} \int_{L(\mathbf{s},t)} q_w\, d\mathbf{x}.$$

We decompose $\mathbf{K}^f$ into $\mathbf{K}^f = K_n^f\mathbf{N} + \mathbf{K}_\tau^f\mathbf{T}$ and define $\mathbf{g}_\tau = \mathbf{Tg}$. Further, we multiply

the equation (3.1b) for $i = f$ by $\mathbf{T}$ and $\mathbf{N}$. By averaging over the line segments we deduce using (3.16) the relation

$$\begin{aligned} 0 &= \int_{L(\mathbf{s},t)} \mathbf{T}\mathbf{v}^f + \lambda^f(S^f)\mathbf{T}\mathbf{K}^f\big(\nabla p^f - G^f(S^f)\mathbf{g}\big)\, d\mathbf{x} \\ &= d(\mathbf{s},t)\mathbf{v}_\Gamma \\ &\quad + \lambda^f(S_\Gamma)\mathbf{K}_\tau^f\Big(\nabla_\tau(d(\mathbf{s},t)p_\Gamma) - \nabla_\tau d(\mathbf{s},t)\{\!\{p\}\!\} - d(\mathbf{s},t)G^f(S_\Gamma)\mathbf{g}_\tau\Big) + O(\bar{d}) \end{aligned} \tag{3.19}$$

and

$$\begin{aligned} 0 &= \frac{1}{d(\mathbf{s},t)}\int_{L(\mathbf{s},t)} \mathbf{N}\mathbf{v}^f + \lambda^f(S^f)\mathbf{N}\mathbf{K}^f(\nabla p^f - G^f(S^f)\mathbf{g})\, d\mathbf{x} \\ &= \{\!\{\mathbf{v}\cdot\mathbf{n}\}\!\} + \lambda^f(S_\Gamma)K_n^f\left(-\frac{[\![p]\!]}{d(\mathbf{s},t)} - G^f(S_\Gamma)(\mathbf{g}\cdot\mathbf{n})\right) + O(\bar{d}). \end{aligned} \tag{3.20}$$

To formulate a closed model it remains to impose suitable coupling conditions at the interfaces between the subdomains. We approximate p^f by a quadratic polynomial $\tilde{p}^f(\xi) = a\xi^2 + b\xi + c,\ \xi \in \left[-\frac{d}{2}, \frac{d}{2}\right]$, along the line segment $L(\mathbf{s},t)$. Here, the coefficients a, b, c depend on $(\mathbf{s},t)$. This polynomial is supposed to satisfy the four continuity conditions (3.2b), (3.2c) at the boundaries (compare Figure 3.3) where one can be eliminated using (3.20). Averaging as in (3.7), we obtain the relation

$$p_\Gamma = \frac{1}{d(\mathbf{s},t)}\int_{L(\mathbf{s},t)} p^f(.,t)\, d\mathbf{x} = \int_{-\frac{d}{2}}^{\frac{d}{2}} \tilde{p}^f(\xi)\, d\xi + O(\bar{d}) \tag{3.21}$$

$$= \{\!\{p\}\!\} - \frac{d}{12\lambda^f(S_\Gamma)\mathbf{K}_n^f}[\![\mathbf{v}\cdot\mathbf{n}]\!] + O(\bar{d}). \tag{3.22}$$

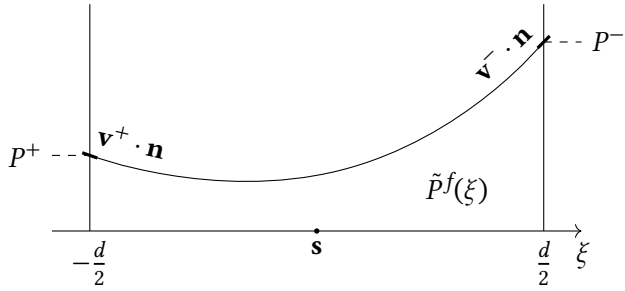

Figure 3.3: Within the fractures the pressure along the line segments is approximated by a second-order polynomial that satisfies conditions (3.2) *at the boundary.*

Combining equation (3.20) and (3.21) leads for $\alpha \in \{+,-\}$ to

$$\mathbf{v}^\alpha \cdot \mathbf{n}^\alpha = -\lambda^f(S_\Gamma) K_n^f \left(\frac{p_\Gamma - p^\alpha}{d/2} + \frac{p_\Gamma - \{\!\{p\}\!\}}{d/4} - G^f(S_\Gamma)(\mathbf{g} \cdot \mathbf{n}^\alpha) \right) + O(\bar{d}). \tag{3.23}$$

This identity provides a coupling condition between the bulk and the fracture problem, cf. (3.27) below. From the divergence constraint in (3.1) we obtain equation (3.15) directly with a source term $d(\mathbf{s},t) q_{nw}^\Gamma$ where $q_{nw}^\Gamma := \frac{1}{d(\mathbf{s},t)} \int_{L(\mathbf{s},t)} q_{nw}\, d\mathbf{x}$ on the right-hand side. The coupling conditions for the mass balance (3.2a) can be rewritten as

$$\begin{aligned} (\mathbf{F}(S^\alpha(\mathbf{s}_\alpha,t), \mathbf{v}^\alpha(\mathbf{s}_\alpha,t)) \cdot \mathbf{n}^\alpha)|_{\gamma_\alpha} &= \left(\mathbf{F}^f(S^f(\mathbf{s}_\alpha,t), \mathbf{v}^f(\mathbf{s}_\alpha,t)) \cdot \mathbf{n}^\alpha \right)|_{\gamma_\alpha} \\ &= \left(\mathbf{F}^f(S_\Gamma(\mathbf{s},t), \mathbf{v}^\alpha(\mathbf{s}_\alpha,t)) \cdot \mathbf{n}^\alpha \right)|_{\gamma_\alpha} + O(\bar{d}) \end{aligned} \tag{3.24}$$

for $\alpha \in \{+,-\}$.

Before we summarize the reduced discrete fracture model, we come up with some physical considerations. Within the reduced model, a different concept of physical volume occurs. This is because the storage volume $|\Omega|_{\text{storage}}$ that can

be occupied by fluid is given by the volume of the bulk domain plus the aperture integrated over the interface length. To be more precise, we define the storage volume by

$$|\Omega|_{\text{storage}} := \int_{\Omega} 1 \, d\mathbf{x} + \int_{\Gamma(t)} d(\cdot, t) \, d\mathbf{x}.$$

This concept of storage volume in the reduced model leads to unconventional behavior regarding mass conservation. For instance, when the fracture geometry changes, we increase (or decrease) the physical volume within the fracture while the volume of the surrounding bulk domain stays constant. This is in contradiction to the full-dimensional setup where the volume of the bulk domain will decrease (or increase) accordingly. We try to ensure mass conservation by assuming no fluid exchange between bulk and fracture domain caused by the change of aperture. Doing so, we can ensure mass conservation in both bulk and fracture domain separately, even if the geometry of the fracture changes.

Within our model above, one can identify the terms $\partial_t d(\mathbf{s}, t)(\phi^f S^f(\mathbf{s}, t)|_{\mathbf{s}=\mathbf{s}_\pm})$, $\nabla_\tau d\mathbf{TF}^f(S^f, {}^f)|_{\mathbf{s}_\pm}$ and $\nabla_\tau d(\mathbf{s}, t)\{\!\{p\}\!\}$ to govern the mass flux between fracture and bulk domain due to non-constant aperture. Therefore, for the sake of our mass conservation considerations, we will omit these terms. Further investigation might lead to these additional terms in the reduced model, but supplementary deliberation about the concept of mass conservation will be necessary.

3.3 The Reduced Discrete Fracture Model

Neglecting the $O(\bar{d})$-terms and incorporating the above mentioned considerations, we summarize the reduced model equations (3.18), (3.19), (3.23) and (3.24). For each $t \in (0, T)$ let as before $\Gamma(t) \subset \Omega$ be a given family of hypersurfaces and $d(\mathbf{s}, t)$ the corresponding aperture in $\mathbf{s} \in \Gamma(t)$ and $D(t) := \Omega \setminus \bar{\Gamma}(t)$.

The wetting fluid saturation $S : D_t \to [0,1]$, the global pressure $p : D_t \to \mathbb{R}$ and the total velocity $\mathbf{v} : D_t \to \mathbb{R}^n$ in the bulk medium satisfy

$$\begin{aligned} (\phi S)_t + \operatorname{div} \mathbf{F}(S,\mathbf{v}) &= q_w, \\ \mathbf{v} + \lambda(S)\mathbf{K}(\nabla p - G(S)\mathbf{g}) &= \mathbf{0}, \qquad \text{in } D_t, \\ \operatorname{div}(\mathbf{v}) &= q_w + q_{nw} \end{aligned} \tag{3.25}$$

where $\mathbf{F}(S,\mathbf{v})$ and $G(S)$ are defined as for (1.4). On Γ_t we search for the reduced quantities $S_\Gamma : \Gamma_t \to [0,1]$, $p_\Gamma : \Gamma_t \to \mathbb{R}$ and $\mathbf{v}_\Gamma : \Gamma_t \to \mathbb{R}^n$ satisfying

$$\begin{aligned} (d\phi^f S_\Gamma)_t + \operatorname{div}_\tau\Big(d\mathbf{F}^f(S_\Gamma,\mathbf{v}_\Gamma)\Big) &= [\![\mathbf{F}(S,\mathbf{v})\cdot\mathbf{n}]\!] + dq_w^\Gamma, \\ d\mathbf{v}_\Gamma + \lambda^f(S_\Gamma)\mathbf{K}_\tau^f\Big(\nabla_\tau(dp_\Gamma) - dG^f(S_\Gamma)\mathbf{g}_\tau\Big) &= \mathbf{0}, \qquad \text{in } \Gamma_t. \\ \operatorname{div}_\tau(d\mathbf{v}_\Gamma) &= [\![\mathbf{v}\cdot\mathbf{n}]\!] + d(q_w^\Gamma + q_{nw}^\Gamma) \end{aligned} \tag{3.26}$$

The systems (3.25), (3.26) are closed at the hypersurface $\Gamma(t)$ by the interface conditions

$$\begin{aligned} &\mathbf{F}(S^\alpha,\mathbf{v}^\alpha)\cdot\mathbf{n}^\alpha = \mathbf{F}^f(S_\Gamma,\mathbf{v}^\alpha)\cdot\mathbf{n}^\alpha, \\ &\mathbf{v}^\alpha\cdot\mathbf{n}^\alpha = -\lambda^f(S_\Gamma)K_n^f\left(\frac{p_\Gamma - p^\alpha}{d/2} + \frac{p_\Gamma - \{\!\{p\}\!\}}{d/4} - G^f(S_\Gamma)(\mathbf{g}\cdot\mathbf{n}^\alpha)\right) \end{aligned} \tag{3.27}$$

on $\Gamma(t)\times\{t\}, t\in(0,T), \alpha\in\{+,-\}$.

Remark 3.2: *(i) In case of $S \equiv S_\Gamma \equiv 0$ and $\mathbf{g} = \mathbf{0}$ the model (3.25)-(3.27) reduces to the single-phase case as described in [51]. Here, our pressure coupling condition corresponds to the shape parameter value $\xi = \frac{2}{3}$.*

(ii) For $d = const.$ we note that even if we construct the models as in [32] and [43], we obtain different coupling conditions. For instance, in contrast to [32] we replaced $G^f(S)|_{\gamma_\pm}$ by $G^f(S_\Gamma)$ instead of $G^f(S^\pm)$. This choice appears consistent to us as it is used for all other terms depending on S.

(iii) Reduced models for unsaturated flow [47] exhibit a very similar structure as model (3.25)-(3.27). However, because of the advection-dominated regime neglecting capillary pressure, the reduced model can not be directly linked to the unsaturated case.

(iv) The assumption that p_f is transversally constant leads to the coupling conditions $p = p_f$ and $\mathbf{v}\cdot\mathbf{n} = 0$. These conditions are analyzed in [57]. However, our conditions that are built on a higher-order approximation include also the case of lower permeable fractures (barriers) where usually $[\![p]\!] \neq 0$.

The equations (3.25), (3.26) describe a mixed-dimensional problem of hyperbolic-elliptic type in time-dependent domains. Special numerical methods and tools are required to solve such kind of problem.

In the next section, we will describe our solution approach. We follow a finite volume approach because of the hyperbolic character of the saturation equation. As a novel contribution this approach is coupled with a moving-mesh concept that keeps track of the moving lower-dimensional domains.

3.4 The Finite-Volume Moving-Mesh Algorithm

A large variety of numerical methods have been proposed for mixed-dimensional models (see, e.g., [10, 13, 16, 32]). They can be classified in two categories: conforming and non-conforming methods. The non-conforming methods make use of independent discretizations of full-dimensional and lower-dimensional sets, whereas conforming methods assume some kind of conformity of the lower-dimensional set to the bulk mesh. For instance, mesh elements of the lower-dimensional mesh coincide with facets of the bulk mesh. Non-conforming methods seem to suggest themselves as a good choice for moving interfaces being much more easy to handle. However, the mutual geometrical relations are not trivial to compute, and have to be recomputed, in principle, at each time step. If instead one is able to manage a moving mesh, the geometrical relations

become trivial. Therefore, we propose a moving-mesh method that permits the efficient tracking of lower-dimensional mesh facets. We utilize the conformity in a finite volume method by only adopting fluxes at the lower-dimensional interface.

In the following, a finite volume discretization will be used for both the bulk and the fracture problem. The coupling between the two problems is incorporated by suitable fluxes at the edges of the codimension-1 interface which ensures, in particular, conservation of mass. To keep track of the moving interface the ansatz results in a new finite-volume moving-mesh method (FVMM).

We will use a two-point flux approximation for the discretization of the pressure gradient in (3.25), (3.26). We use this simple approach because large effort is necessary to update cell stencils during re-meshing. It is known that a standard two-point flux approximation is not consistent on general triangular grids and for anisotropic permeability tensors [30]. Therefore, we will propose an adaptation of the two-point flux approximation that is consistent at least for isotropic permeabilities in Section 3.4.3. This is achieved by locating the pressure values at the cirumcenters.

Before we start with the description of the scheme, let us introduce some notation.

3.4.1 The Geometry of the Moving Mesh

In the sequel, we assume that the open subset Ω of $\mathbb{R}^n, n \in \{2, 3\}$, is a polygon. Likewise, the interface $\Gamma = \Gamma(t)$ is assumed to be a polygonal hypersurface for all $t \in [0, T]$. In this section, we introduce the moving-mesh concept that ensures that $\Gamma(t)$ is always represented as a union of facets of the triangulation for Ω.

For each $F \in \mathscr{F}(K)$, cf. Section 2.2.1, we denote by $\mathbf{n}_K$ the outer normal to this facet seen from K weighted by the facet area. The outer normal defines an inner, positive side of the facet and an outer, negative side. The adjacent cells are therefore denoted by $K^+ = K$ and K^-.

Turning to the evolution of the mesh, let $0 = t_0 < t_1 < \cdots < t_N = T, N \in \mathbb{N}$, be a series of time steps. In the following, we start with a triangulation which is conforming to the interface for each time step $t_i, i = 0, ..., N$. In between, we assume that the vertices of $\mathcal{T}$ move linearly in time. That is, all $K = K(t) \in \mathcal{T}(t), t \in (t_i, t_{i+1})$, are given by $K(t) := \text{conv}(\mathbf{p}_0(t), \dots, \mathbf{p}_n(t))$, where $\mathbf{p}_i(t) \in \mathbb{R}^n$ moves with speed $\mathbf{s}_i \in \mathbb{R}^n$ according to

$$\mathbf{p}_i(t) = \mathbf{p}_i(0) + t\mathbf{s}_i, \qquad i = 0, \dots, n.$$

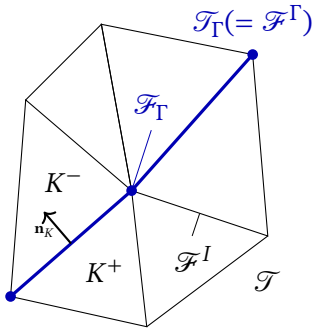

Figure 3.4: Visualization of the geometrical notations used in Section 3.4.1 for $n = 2$.

3.4.2 Moving-Mesh Method for the Saturation Equations

In this section, we describe the moving-mesh method that is used for handling the propagation of fractures. Note that moving-mesh methods are typically used to minimize artificial diffusion, for instance, when tracking discontinuities in the solution of hyperbolic problems [39]. In contrast, we use it to track a lower-dimensional interface.

The moving-mesh method requires an additional geometrical flux within the finite volume formulation. This geometrical flux accounts for the mass flux

across moving facets. Here, we want to incorporate the ideas that have been applied in numerical methods for droplet dynamics [25]. Because it is only an additional flux in the finite volume update step, it works without any re-meshing and projection as long as the triangulation is not adapted, and reduces to the classic finite volume scheme if no movement occurs. With this method one is able to move the lower-dimensional fracture facets without moving mass in the solution in the surrounding mesh.

Let us consider a single interval (t_i, t_{i+1}). We assume that $\mathscr{T}(t)$ does not degenerate for $t \in (t_i, t_{i+1})$, i.e., there is a $c > 0$ such that for all $t \in (t_i, t_{i+1})$ we have $|K| > c$ for all $K \in \mathscr{T}(t)$. If this condition is not satisfied, the triangulation has to be adapted first, which is be described in detail in Section 2.3.

Now, consider the space-time cell

$$K_{st} = \Big\{(\mathbf{x}, t) \;\Big|\; \mathbf{x} \in K(t),\ t_i \le t \le t_{i+1}\Big\}.$$

Integrating (3.25a) over K_{st} and using Reynolds' transport theorem we compute

$$\begin{aligned}
&\int_{K_{st}} (\phi S)_t + \operatorname{div} \mathbf{F}(S, \mathbf{v})\, d(\mathbf{x}, t) \\
&\qquad = \int_{K(t_{i+1})} \phi S(\cdot, t_{i+1})\, d\mathbf{x} - \int_{K(t_i)} \phi S(\cdot, t_i)\, d\mathbf{x} \\
&\qquad\quad + \int_{t_i}^{t_{i+1}} \int_{\partial K(t)} \big(\mathbf{F}(S, \mathbf{v}) - (\phi S)\mathbf{s}\big) \cdot \mathbf{n}_{K(t)}\, dS\, dt \\
&\qquad = \int_{t_i}^{t_{i+1}} \int_{K(t)} q_w\, d\mathbf{x}\, dt.
\end{aligned} \tag{3.28}$$

Here, $\mathbf{s} : K(t) \to \mathbb{R}^n$ is the speed of a point

$$\mathbf{x}(t) = \mathbf{p}_0(t) + \sum_{i=1}^{n} \lambda_i \big(\mathbf{p}_i(t) - \mathbf{p}_0(t)\big),$$

with $\lambda_i \in [0,1],\ i = 1,\dots,n$, i.e.,

$$\mathbf{s}(\mathbf{x}) = \mathbf{s}_0 + \sum_{i=1}^{n} \lambda_i(\mathbf{s}_i - \mathbf{s}_0).$$

With a slight abuse of notation, in the above formula, $\mathbf{n}_{K(t)} : \partial K(t) \to \mathcal{S}^{n-1}$ denotes the unit outer normal at the boundary of $K(t)$. Let us define the finite volume ansatz-space of cell-wise constant functions

$$\mathcal{S}_h(\mathscr{T}) := \{v \in L^2(\mathbb{R}^n) \mid v_K := v|_K \in \mathbb{P}_0(K)\ \forall K \in \mathscr{T}\}.$$

We choose two discrete representatives of the saturation $S^i, S^{i+1} \in \mathcal{S}_h(\mathscr{T})$ and define S^0 by $S^0_K := \frac{1}{|K|}\int_K S(\cdot,0)\,d\mathbf{x}$. Now, using an implicit Euler time-stepping for (3.28) and dividing by $|K(t_{i+1})|$ we evolve $S^i \to S^{i+1}$ by

$$\begin{aligned}\phi S_K^{i+1} - \phi S_K^i \frac{|K(t_i)|}{|K(t_{i+1})|} + (t_{i+1}-t_i) \sum_{F\in\mathscr{F}\left(K(t_{i+1})\right)} \Big[g_F(S^{i+1}_{K^+}, S^{i+1}_{K^-}, \mathbf{v}) + h_F(S^{i+1}_{K^+}, S^{i+1}_{K^-})\Big] \\ = \frac{t_{i+1}-t_i}{|K(t_{i+1})|}\int_{K(t_{i+1})} q_w\,d\mathbf{x}.\end{aligned}$$

Here, $g_F(\cdot,\cdot,\mathbf{v})$ is a numerical flux that is consistent with the flux function $\mathbf{F}(S,\mathbf{v})\cdot\mathbf{n}_K$, whereas the numerical flux $h_F(\cdot,\cdot)$ has to be consistent with the geometric flux function $-(\phi S)\mathbf{s}\cdot\mathbf{n}_K$. Suitable choices are, for instance, a Lax-Friedrichs or Godunov-type flux for g_F and an upwind flux for h_F. Because the flux function $\mathbf{F}(S,\mathbf{v})$ in our model is non-monotone in the first argument, we will use the Godunov flux that results from an exact solution of the Riemann problem, cf. Equation 3.29 below. The fluxes at the boundary have to be adapted according to the boundary conditions.

With the additional geometrical flux and volume term the conservative quantity is not transported in space although vertices of the triangulation move. We show in Section 3.5.2 numerical examples demonstrating the performance of

the scheme for constant initial data. The scheme can only be applied as long as no cell degenerates. In order to prevent degeneration and improve mesh quality we use the re-meshing techniques provided by Dune-MMesh, see Section 2.3 for details. We can use this moving-mesh method for both the bulk and the lower-dimensional domain. To couple the schemes, the fluxes at the inner fracture facets $\mathscr{F}^\Gamma$ have to incorporate condition (3.27).

We shall describe our choice for the numerical flux $g(\cdot,\cdot,\mathbf{v})$ in more detail. The flux has to be generalized for a discontinuous flux function as the physical properties (in particular $\mathbf{K}$) might vary in space. We start with the formulation of the Godunov flux [46] which can be written as

$$g(S^+,S^-,\mathbf{v}) = \begin{cases} \min\limits_{S^+<S<S^-} \mathbf{F}(S,\mathbf{v})\cdot\mathbf{n}_K, & \text{if } S^+ \le S^-, \\ \max\limits_{S^-<S<S^+} \mathbf{F}(S,\mathbf{v})\cdot\mathbf{n}_K, & \text{if } S^- < S^+. \end{cases} \tag{3.29}$$

Generalizing this flux for a discontinuous flux function we use the identity

$$g^*(S^+,S^-,\mathbf{v}) := g^+(S^+,S^*,\mathbf{v}) = g^-(S^*,S^-,\mathbf{v}) \text{ for some } S^* \in [0,1].$$

This generalization has to be applied on all facets where the physical parameters of the adjacent cells are distinct, in particular between bulk and fracture domain.

For a quadratic material law $k_w(S) = S^2$ and $k_{nw}(S) = (1-S)^2$ we implemented explicit formulas which can be evaluated efficiently. In particular, we use the fact that $\mathbf{F}(S,\mathbf{v})$ has a single extremum (cf. Figure 3.6). This fact can also be exploited to deduce an explicit formula for the generalized flux.

3.4.3 Circum-Centered Two-Point Flux Approximation on Moving Meshes

We continue with the discretization of the elliptic part (3.25b)-(3.25c) governing bulk pressure and velocity. The derivation shows the method for the bulk problem

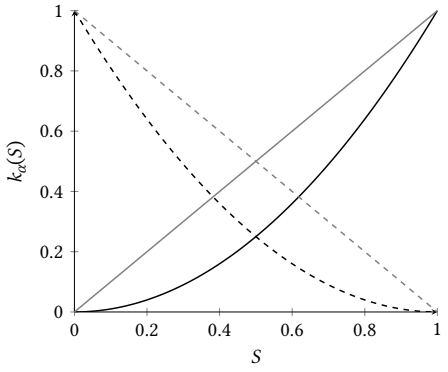

Figure 3.5: Relative permeability functions for two (linear/quadratic) choices for k_α. The continuous curve shows k_w, the dashed one shows k_{nw}.

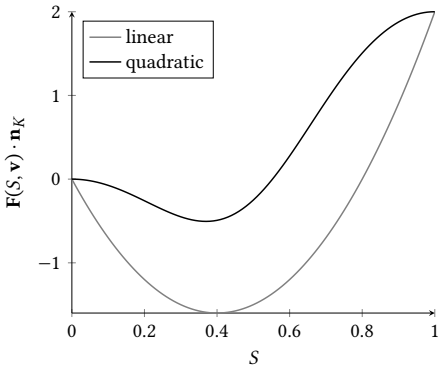

Figure 3.6: The non-monotone shape of the flux function $\mathbf{F}(\cdot,\mathbf{v}) \cdot \mathbf{n}_K$. Here, k_α is linear / quadratic, $\mathbf{v} \cdot \mathbf{n}_K = 2$ and $\mathbf{n}_K\mathbf{K}(\rho_n - \rho_w)\mathbf{g} = 10$.

in $D(t)$, but it is similar for the problem on the interface $\Gamma(t)$.

The finite volume approach for the divergence constraint (1.4c) reads

$$\sum_{F\in\mathcal{F}(K(t))} v_F \, d\mathbf{x} = \int_{K(t)} (q_w + q_{nw}) \, d\mathbf{x},$$

where v_F is a suitable approximation of $\mathbf{v}\cdot\mathbf{n}$ on F and $K(t) \in \mathcal{T}(t)$. A simple choice for v_F is the two-point flux approximation (TPFA) derived from equation (1.4b), see [30]. Including the gravity term it reads

$$v_F := -\mathbb{T}_F\big(p_{K^-} - p_{K^+} - \mathbb{G}_F\big),$$

where the transmissibility $\mathbb{T}_F$ is defined by

$$\mathbb{T}_F := \frac{\mathbb{T}_{K^+}\mathbb{T}_{K^-}}{\mathbb{T}_{K^+} + \mathbb{T}_{K^-}} \qquad \text{with} \qquad \mathbb{T}_i := \lambda(S_i)\frac{\mathbf{d}_i \mathbf{K}_i \mathbf{d}_i}{\|\mathbf{d}_i\|_2^3}, \quad i \in \{K^+, K^-\}.$$

Here, $\mathbf{d}_i := \mathbf{m}_F - \mathbf{m}_i$, $i \in \{K^+, K^-\}$, is the distance vector between the center $\mathbf{m}_F$ of facet F and the cell centers $\mathbf{m}_i$. $\mathbf{K}_i$ for $i \in \{K^+, K^-\}$ denotes the restriction of $\mathbf{K}$ to K^+ and K^-. For consistency of the scheme it is necessary that $\mathbf{m}_{K^+}, \mathbf{m}_{K^-}, \mathbf{m}_F$ are the cirumcenters of K^+, K^-, F. The gravitational influence $\mathbb{G}_F$ is defined by

$$\mathbb{G}_F := \mathbb{G}_{K^+} - \mathbb{G}_{K^-}, \qquad \mathbb{G}_i := G(S_i)\,(\mathbf{d}_i \cdot \mathbf{g}), \quad i \in \{K^+, K^-\}.$$

The choices for the transmissibilities have been made such that

$$-\mathbb{T}_{K^+}\big(p^* - p_{K^+} - \mathbb{G}_{K^+}\big) = \mathbb{T}_{K^-}\big(p^* - p_{K^-} - \mathbb{G}_{K^-}\big)$$

holds for some intermediate pressure value p^*. This is the classical way to derive the harmonic average occurring in the two-point flux approximation, and the intermediate pressure actually can be eliminated.

As we assumed that the triangulation is conforming to the interface, some facets coincide with lower-dimensional fracture elements $K_\Gamma \in \mathscr{T}_\Gamma$. At such facets, we include the coupling conditions (3.27) of the reduced model. Therefore, we introduce intermediate pressure values $p|_{\gamma_+}$ and $p|_{\gamma_-}$ at the boundaries of the bulk medium next to the fracture. Conditions for the intermediate pressure values can be stated by

$$\begin{aligned} v_F|_{\gamma_+} &= -\mathbb{T}_{K^+}\big(p|_{\gamma_+} - p_{K^+} - \mathbb{G}_{K^+}\big), \\ v_F|_{\gamma_-} &= -\mathbb{T}_{K^-}\big(p|_{\gamma_-} - p_{K^-} - \mathbb{G}_{K^-}\big). \end{aligned}$$

Then, the coupling conditions in (3.27) can be used to eliminate the intermediate values. Defining

$$\mathbb{T}_\Gamma := \frac{2}{d}\lambda^f(S_{T_\Gamma})K_n^f, \qquad \mathbb{G}_\Gamma := -\frac{d}{2}G^f(S_{K_\Gamma})\,(\mathbf{n}_K \cdot \mathbf{g})$$

we obtain (using an computer algebra system)

$$v_F|_{\gamma_+} = R \begin{pmatrix} 3\mathbb{T}_\Gamma + 2\mathbb{T}_{K^-} \\ -3\mathbb{T}_\Gamma - 3\mathbb{T}_{K^-} \\ \mathbb{T}_{K^-} \end{pmatrix} \cdot \begin{pmatrix} p_{K^+} + \mathbb{G}_{K^+} \\ p_\Gamma + \mathbb{G}_\Gamma \\ p_{K^-} + \mathbb{G}_{K^-} + 2\mathbb{G}_\Gamma \end{pmatrix}$$

where

$$R := \frac{\mathbb{T}_{K^+}\mathbb{T}_\Gamma}{\mathbb{T}_{K^+}\mathbb{T}_{K^-} + 3{\mathbb{T}_\Gamma}^2 + 2\mathbb{T}_\Gamma(\mathbb{T}_{K^+} + \mathbb{T}_{K^-})}.$$

Remark 3.3: *The presented discretization is consistent for isotropic intrinsic permeabilities if we use circumcenters for* $\mathbf{m}_{K^+}, \mathbf{m}_{K^-}, \mathbf{m}_F$*, and, therefore, locate the pressure values at the circumcenters of the tetrahedral cells [30]. This is still valid for the coupling to the fracture network as the circumcenters of the lower-dimensional mesh elements are located at the orthogonal connection line of the circumcenters of the two adjacent bulk cells.*

In a recent benchmark study, we showed that this TPFA scheme with circumcenters produces comparative results while having a comparably small number of degrees of freedom [13].

3.4.4 The Complete FVMM Algorithm

With the Sections 3.4.1, 3.4.2 and 3.4.3 we can now present the complete FVMM algorithm. It governs the discrete two-phase dynamics in the time-dependent bulk domains as well as in the lower-dimensional fractures. It can be stated as follows.

Consider a triangulation $\mathcal{T}(t)$ of domain Ω which is conforming to the interface triangulation $\mathcal{T}_\Gamma(t)$ of the time-dependent interface $\Gamma(t)$. We start the algorithm

by averaging the initially given bulk saturation S_0 and the fracture saturation $S_{\Gamma,0}$. For all $K \in \mathscr{T}(0)$ and $K_\Gamma \in \mathscr{T}_\Gamma(0)$ set

$$S_K^0 := \frac{1}{|K|}\int_K S_0(\mathbf{x})\,d\mathbf{x},$$
$$(S_\Gamma)_{K_\Gamma}^0 := \frac{1}{|K_\Gamma|}\int_{K_\Gamma} S_{\Gamma,0}(\mathbf{x})\,d\mathbf{x}.$$

The cell-wise constant saturation values define discrete functions

$$S^i = (S_K^i)_{K\in\mathscr{T}(t_i)} \qquad \in \mathscr{S}_h\big(\mathscr{T}(t_i)\big),$$
$$(S_\Gamma)^i = \big((S_\Gamma)_{K_\Gamma}^i\big)_{K_\Gamma\in\mathscr{T}_\Gamma(t_i)} \qquad \in \mathscr{S}_h\big(\mathscr{T}_\Gamma(t_i)\big)$$

that will approximate the exact solution of system (3.25)-(3.27).

For each time step t_i with given $S^i \in \mathscr{S}_h(\mathscr{T})$ and $(S_\Gamma)^i \in \mathscr{S}_h(\mathscr{T}_\Gamma)$, we solve the discrete system (3.30)-(3.33) below with a backward Euler time stepping monolithically. Alternative solution strategies could be utilized here, e.g., IMPES splitting, but our monolithic approach implemented with DuMu$^{\mathrm{x}}$ [44] turned out to be reliable. Hereby, the size of the time step decreases automatically in case of convergence issues during the Newton iteration, and is usually in the order of magnitude suggested by the CFL condition.

We solve the systems below for $(S^{i+1}, p^{i+1}) \in \mathscr{S}_h(\mathscr{T}) \times \mathscr{S}_h(\mathscr{T})$ and $\big((S_\Gamma)^{i+1}, (p_\Gamma)^{i+1}\big) \in \mathscr{S}_h(\mathscr{T}_\Gamma) \times \mathscr{S}_h(\mathscr{T}_\Gamma)$ defined by

$$\frac{\phi S_K^{i+1} - \phi S_K^i \frac{|K(t_i)|}{|K(t_{i+1})|}}{t_{i+1}-t_i} + \sum_{F\in\mathscr{F}^I}\big(g_F(S_{K^+}^{i+1}, S_{K^-}^{i+1}, v_F^{i+1}\mathbf{n}_K) + h_F(S_{K^+}^{i+1}, S_{K^-}^{i+1})\big) + \sum_{F\in\mathscr{F}^\Gamma} g_F(S_{K^+}^{i+1}, S_{K_\Gamma}^{i+1}, v_F|_{\gamma_+}^{i+1}\mathbf{n}) = q_w^{i+1} \tag{3.30}$$

$$\sum_{F\in\mathscr{F}^I} v_F^{i+1}\mathbf{n}_K + \sum_{F\in\mathscr{F}^\Gamma} v_F|_{\gamma_+}^{i+1}\mathbf{n} = q_w^{i+1} + q_{nw}^{i+1} \tag{3.31}$$

for all $K(t_i) \in \mathscr{T}(t_{i+1})$, and

$$\begin{aligned}
&\frac{d^{i+1}\phi^\Gamma S^{i+1}_{K_\Gamma} - d^i\phi^\Gamma S^i_{K_\Gamma}\frac{|K_\Gamma(t_i)|}{|K_\Gamma(t_{i+1})|}}{t_{i+1}-t_i} \\
&\qquad + \sum_{F\in\mathscr{F}^I_\Gamma}\left(d^{i+1}g_F(S^{i+1}_{K^+_\Gamma}, S^{i+1}_{K^-_\Gamma}, \mathbf{v}_{F_\Gamma}\mathbf{n}_{K_\Gamma}) + h_F(S^{i+1}_{K^+_\Gamma}, S^{i+1}_{K^-_\Gamma})\right) \qquad (3.32)\\
&= g_{\gamma^+}(S^{i+1}_{K_\Gamma}, S^{i+1}_{K^+_\Gamma}, v_F|^{i+1}_{\gamma_+}\mathbf{n}) + g_{\gamma^-}(S^{i+1}_{K_\Gamma}, S^{i+1}_{K^-_\Gamma}, v_F|^{i+1}_{\gamma_-}\mathbf{n}) + d^{i+1}(q^\Gamma)^{i+1}_w,
\end{aligned}$$

$$\sum_{F\in\mathscr{F}^I_\Gamma} d^{i+1}\mathbf{v}_{F_\Gamma} = v_F|^{i+1}_{\gamma_+}\mathbf{n} + v_F|^{i+1}_{\gamma_-}\mathbf{n}_K + d^{i+1}\left((q^\Gamma)^{i+1}_w + (q^\Gamma)^{i+1}_{nw}\right) \qquad (3.33)$$

for all $K_\Gamma(t_i) \in \mathscr{T}_\Gamma(t_{i+1})$. For abbreviation, we used $d^i = d(\cdot, t^i)$, $q^{i+1}_\alpha = \int_{K(t_{i+1})} q_\alpha(\mathbf{x}, t_{i+1})\,d\mathbf{x}$ and $(q^\Gamma)^{i+1}_\alpha = \int_{K_\Gamma(t_{i+1})} q^\Gamma_\alpha(\mathbf{x}, t_{i+1})\,d\mathbf{x}$ where $\alpha \in \{w, nw\}$.

For the purpose of readability we neglected the boundary terms in the formulation above. At Dirichlet boundaries, the outer values $S^{i+1}_{K^-}$ and $p^{i+1}_{K^-}$ (respectively $S^{i+1}_{K^-_\Gamma}$ and $p^{i+1}_{K^-_\Gamma}$) have to be replaced by the Dirichlet boundary value. At Neumann boundaries, the corresponding normal fluxes g and v_F can be replaced directly by the Neumann boundary flux.

3.4.5 Implementation

We implemented the FVMM algorithm (3.30)-(3.33) within the software framework Dune [11] on the basis of the discretization module DuMu^x [44] and the grid implementation Dune-MMesh [21]. The grid implementation Dune-MMesh is essential for both the mixed-dimensional discretization and the moving-mesh method. The details about Dune-MMesh have been described in Chapter 2.

3.5 Numerical Experiments

We demonstrate the performance of the FVMM algorithm in some showcases. For the sake of model validation, we investigate the error between a solution of the reduced model (3.25)-(3.27) and a solution of the full-dimensional model (3.1). In fact, the moving-mesh method can be used to obtain both solutions. In the full-dimensional case, the re-meshing capability of Dune-MMesh is used to track the boundary between bulk and fracture domain.

We consider three numerical experiments for $n = 2$. In the first case we investigate how the FVMM algorithm performs for two-phase dynamics driven by fracture prolongation only. Second, we analyze the same setting but with flow injection into the fracture. Third, we perform a similar analysis with a squeezing fracture. The solution of the reduced model is always compared to the reference solution obtained by resolving the full-dimensional fracture. Finally, we consider a static fracture network for $n = 3$ and a two-dimensional setting with two interfering fractures.

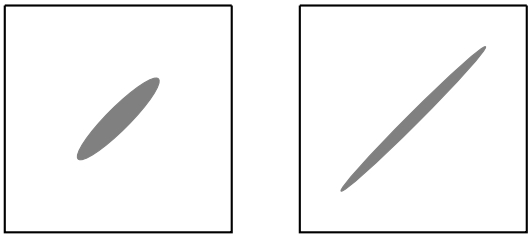

Figure 3.7: Geometrical setting where the fracture prolongates and squeezes over time.

All source code that was used to produce the results and the raw data of the simulation results is accessible via DaRUS [20].

3.5.1 Geometrical Setting and Model Parameters

We choose a similar geometrical setting for the first three two-dimensional cases. Let $\Omega = (0,1)^2$ and $T = 1$. The time-dependent fracture $\Gamma(t)$ is given by an ellipse that prolongates and squeezes over time, i.e.,

$$\Gamma(t) = \{x_1 = x_2 \mid r(x_1, x_2) \leq R(t)\}, \quad (x_1, x_2)^\top \in \Omega. \tag{3.34}$$

In (3.34) we have $r(x_1, x_2) \coloneqq \sqrt{(x_1 - 0.5)^2 + (x_2 - 0.5)^2}$ and $R(t) = 0.25 + t v_{\text{prolong}}$. The aperture is given by

$$d(x_1, x_2, t) = (d_0 - t v_{\text{squeeze}}) \sqrt{1 - \big(r(x_1, x_2) - R(t)\big)^2}, \quad (x_1, x_2)^\top \in \Omega.$$

The constants $d_0, v_{\text{prolong}}, v_{\text{squeeze}} \in \mathbb{R}$ are chosen depending on the case. The geometrical setting is visualized in Figure 3.7. The full-dimensional fracture domain Ω_f is given by $\Omega_f(t) = \{\mathbf{x} \in \Omega \mid \|\mathbf{x} - \mathbf{s}\| \leq d(\mathbf{x}, t), \mathbf{s} \in \Gamma(t)\}$. Inspired by plane Poisseuille flow, we use $\mathbf{K}_f = \frac{d^2}{12}\mathbf{I}$ for the tangential permeability within the fracture. This is also used in the full-dimensional setting.

The main parameters are chosen for all three cases as in Table 3.8, if not stated differently. The choice of the parameters covers realistic settings without being derived from a specific experiment.

3.5.2 Case 1: Two-Phase Flow Dynamics Driven by Fracture Prolongation

As first benchmark problem we want to verify the moving-mesh concept. We consider a setup where the initial saturation is chosen to be constant $S(\cdot, 0) = S_\Gamma(\cdot, 0) = 1$. Then, the evolution of S is supposed to be driven by the deformation of the fracture. We apply no external forces ($\mathbf{g} = 0$) and set the pressure to be zero at the boundaries. Therefore, we have $p \equiv 0$ and $p_\Gamma \equiv 0$. The fracture

Figure 3.8: Model parameters for all test cases.

Parameter	Value
ρ_w	$1000\,\mathrm{kg\,m^{-3}}$
ρ_{nw}	$500\,\mathrm{kg\,m^{-3}}$
$\mathbf{g}$	$(0, -9.81\,\mathrm{m\,s^{-2}})$
η_w	$1\,\mathrm{Pa\,s}$
η_{nw}	$10\,\mathrm{Pa\,s}$
$\mathbf{K}$	$1 \cdot 10^{-8}\,\mathrm{m}^2\,\mathbf{I}$
$\mathbf{K}_f$	$\frac{d^2}{12}\,\mathbf{I}$
ϕ, ϕ_f	1
$k_w(S)$	S^2
$k_{nw}(S)$	$(1-S)^2$

movement is prescribed by $d_0 = 0.1$, $v_{\text{prolong}} = 0.25$ and $v_{\text{squeeze}} = 0$. Hence, all flow dynamics are only due to the change in the fractures' geometry.

The result of the saturation distribution of this example is displayed in Figure 3.10. In the reduced case, the fracture is visualized as transparent overlay with the corresponding aperture. A plot-over-line from the lower-left to the upper-right corner (coinciding with the fracture center-line) is shown in Figure 3.9. Within the fracture, the saturation of the full-dimensional reference solution is averaged along the orthogonal line segments.

We can observe that the saturation within the fracture decreases from the middle of the ellipse advancing to the tips. In the full-dimensional reference, the space taken up by the fracture shows a zero saturation, whereas the saturation is slightly increasing around the initial position of the (wetting-phase filled) fracture. This behavior is reasonable in both cases as empty space is generated within the fracture domain and is initialized with zero saturation. The results of this example show the validity of the FVMM algorithm and its implementation.

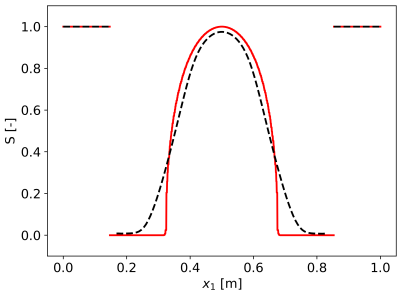

Figure 3.9: Plot-over-line of saturation for Case 1 at $t = 1$ s. Reduced model (solid) vs. full-dimensional model (dashed).

3.5.3 Case 2: Two-Phase Flow Dynamics Driven by Fracture Prolongation and Fluid Infiltration

Now, let us consider a propagating fracture with gravity-driven two-phase flow and compare the numerical solution again with a fully-resolved fracture. The source term $q_w^f = q_{nw}^f = 10\,\mathrm{s}^{-1}$ realizes an infiltration in Γ, or Ω_f, respectively.

The initial saturation is chosen as $S(\mathbf{x}, 0) = 0$ and $S_\Gamma(\mathbf{s}, 0) = 0$. The fracture movement is defined by $d_0 = 0.01$, $v_{\text{prolong}} = 0.25$ and $v_{\text{squeeze}} = 0$. No-flow boundary conditions are imposed everywhere except at the top where we fix the pressure to zero. Again, a plot-over-line through the fracture center-line is displayed in Figure 3.12 and the saturation in Figure 3.14. For this case, we plotted the computational mesh with its adaptation around the upper tip in Figure 3.11.

We see good agreement of the results between the reduced and the full-dimensional model. Small deviations at the fracture tips can be explained by the resolution of the full-dimensional grid and the corresponding error in averaging along the orthogonal line segments. Note that in this example the influence of the tip

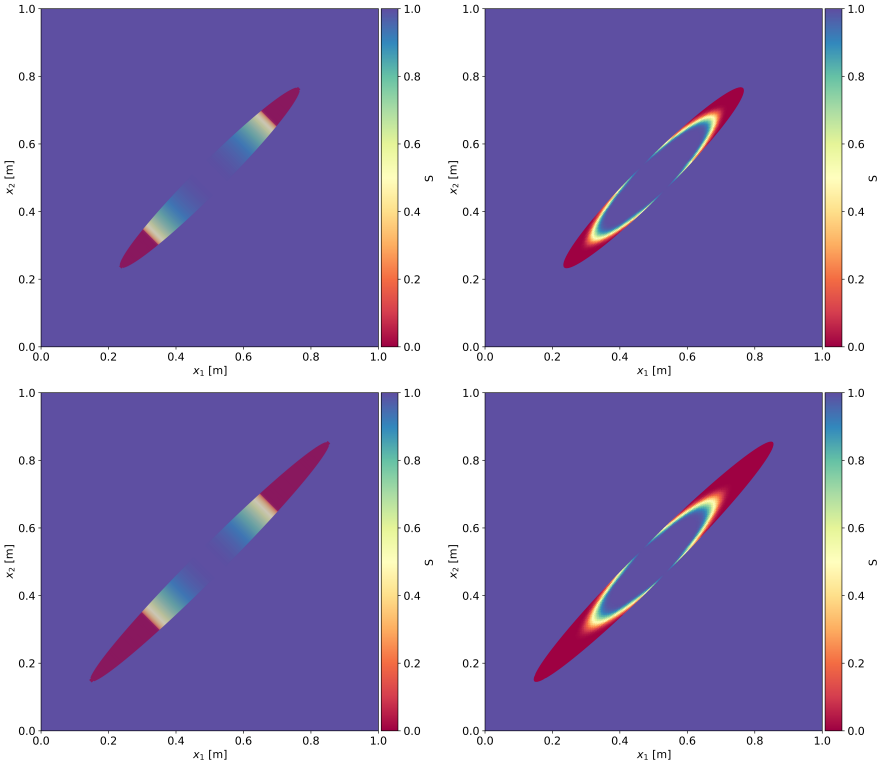

Figure 3.10: Saturation distribution for Case 1 at $t = 0.5$ s (top) and $t = 1$ s (bottom). Left: Reduced model where fracture is visualized as transparent overlay with corresponding aperture. Right: Full-dimensional reference solution.

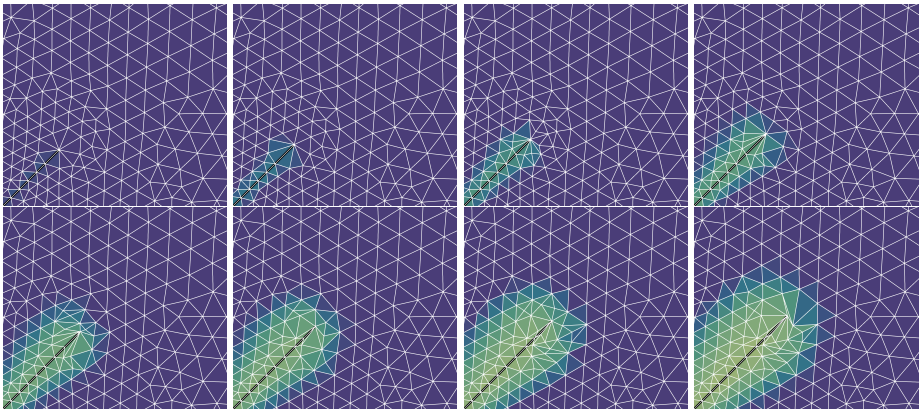

Figure 3.11: As the upper fracture tip of the lower-dimensional fractures moves to the upper right corner of the domain, the computational mesh is adapted to this movement.

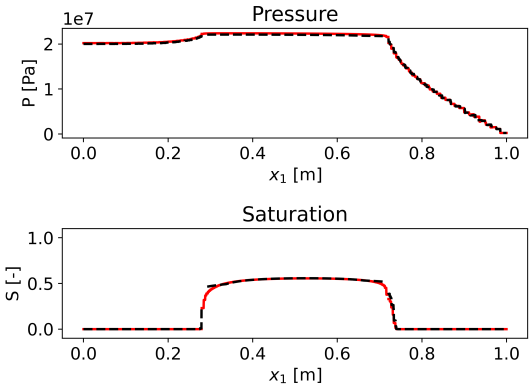

Figure 3.12: Plot-over-line for Case 2 at $t = 1$ s. Reduced model (solid) vs. full-dimensional model (dashed).

movement on the saturation distribution can be well observed around the lower left tip.

3.5.4 Case 3: Two-Phase Flow Dynamics Driven by Fracture Squeezing and Fluid Infiltration

Let us consider a squeezing fracture with the physical parameters as in Case 2, but where the fracture movement is defined by $d_0 = 0.01$, $v_{\text{prolong}} = 0$ and $v_{\text{squeeze}} = 0.005$. Differently from Case 2, the fracture is not prolongated, but on the contrary squeezed.

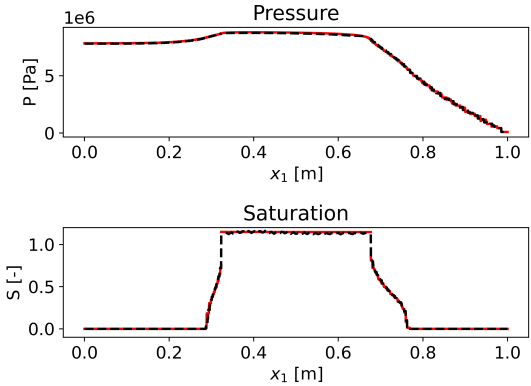

Figure 3.13: Plot-over-line for Case 3 at $t = 1.0$. Reduced model (solid) vs. full-dimensional model (dashed).

As in the cases before, we visualize the saturation in Figure 3.15 and a plot-over-line through the fracture center-line in Figure 3.13 which shows a high accordance between our two models.

The saturation profile in the bulk domain around the fracture tips matches perfectly. For the saturation within the fracture we observe values larger than

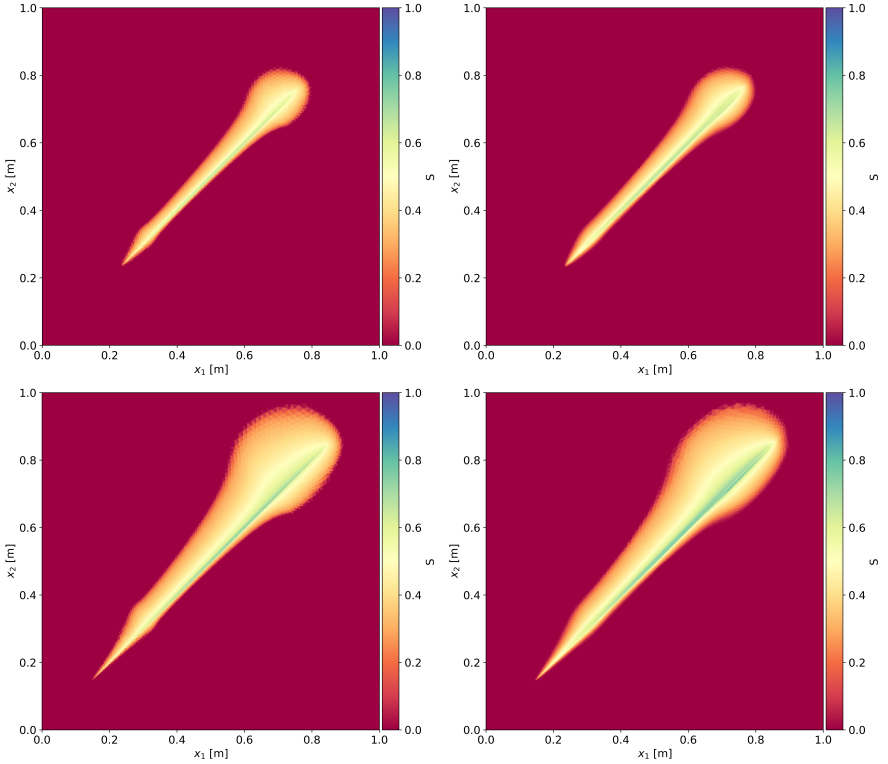

Figure 3.14: Saturation for Case 2 at $t = 0.5$ s and $t = 1$ s. Left: Reduced model. Right: Full-dimensional reference.

one. This is outside the physical admissible region. We presume that this extreme example leads to overshooting behavior due to the boundary condition of the moving mesh method which does not take into account transmission between fracture and bulk domain.

Cases 1 to 3 served to validate the approach as compared to the full-dimensional model. The next two examples show the capability of the FVMM algorithm to

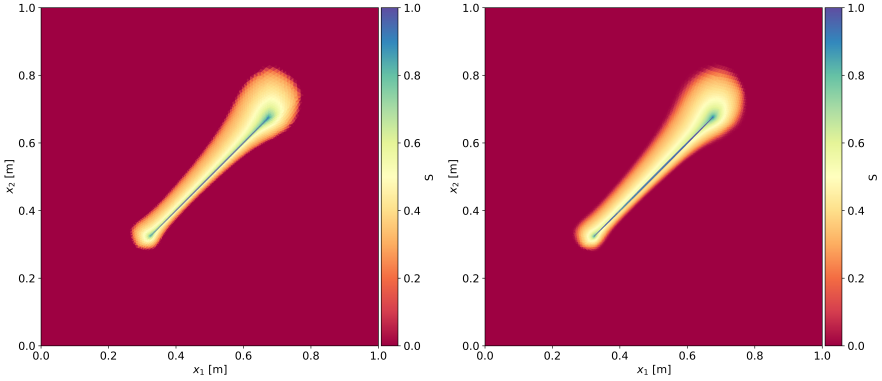

Figure 3.15: Saturation for Case 3 for $t = 1.0$. Left: Reduced model. Right: Full-dimensional reference.

capture two-phase flow and fracture interaction.

3.5.5 Case 4: Static Fractures in Three Dimensions

We show a rather exploratory example of two-dimensional reduced fractures in a three-dimensional bulk porous medium. The idea is to show that the proposed reduced model and scheme can also be used in a three-dimensional setting. Three penny-shaped fractures are located in a column as visualized in Figure 3.16 on the left. In this example, the fractures are assumed to be static with constant apertures $d = 0.01$. The fracture permeability is chosen as $\mathbf{K}^f = 1 \cdot 10^{-4}\,\mathrm{m}^2\mathbf{I}$. All other physical parameters are chosen again as in Table 3.8. A Dirichlet saturation $S_D = 1$ and pressure $p_D = 0$ is set at top and no-flow conditions are imposed on all other boundaries. Thus, we have saturation inflow from the upper boundary which is driven by gravitational forces. In particular, the fracture's permeability is higher than in the surrounding bulk porous medium.

One can see in the time series in Figure 3.16 how the fracture inclusions act as preferred paths for the fluid flow. This example shows that the reduced model can be used also for more complex 2d-3d fracture networks.

3.5.6 Case 5: Fracture Propagation with Two Interfering Fractures

Another exploratory example of propagating fractures demonstrates the strong influence of fracture propagation on the fluid flow. We consider the following geometrical setup. Two horizontally aligned fractures are placed in a domain $\Omega = (0, 2) \times (0, 1)$. The upper fracture is defined by $\Gamma_1 = (0.2, 2) \times \{0.75\}$ and is kept static. In contrast, the tip of the lower fracture $\Gamma_2 = (0, 0.2) \times \{0.25\}$ moves with speed s in direction of the x-axis. We choose both fast and slow movement, $s = 0.1$ and $s = 1.0$, respectively, and compare the two numerical solutions at different time steps, see Figure 3.17. At $t = 1.8$, $t = 18$ respectively, the moving fracture tip reaches the right boundary. All physical parameters are chosen as in the examples above, the fractures' apertures are fixed at $d = 0.01$. Boundary conditions are chosen as follows. We set no-flow boundary conditions on all bulk boundaries, as well as at the tips of the fractures immersed within the domain. Dirichlet values $p_D = 1 \cdot 10^8$ Pa and $S_D = 1$ are chosen for the left fracture boundary, zero Dirichlet values at the right fracture boundary.

We clearly see the propagation of discontinuous saturation fronts through fracture and bulk. From $t = 1.5$ on, the front has reached the upper fracture for both tip propagation speeds. The upper fracture acts as a kind of barrier for further vertical distribution as it transports the wetting-phase to the right boundary. In the long term, i.e., $t = 18$ for $s = 0.1$, the wetting-phase concentration has increased in almost the entire domain. In this example, we can clearly see the influence of fracture propagation on the saturation distribution.

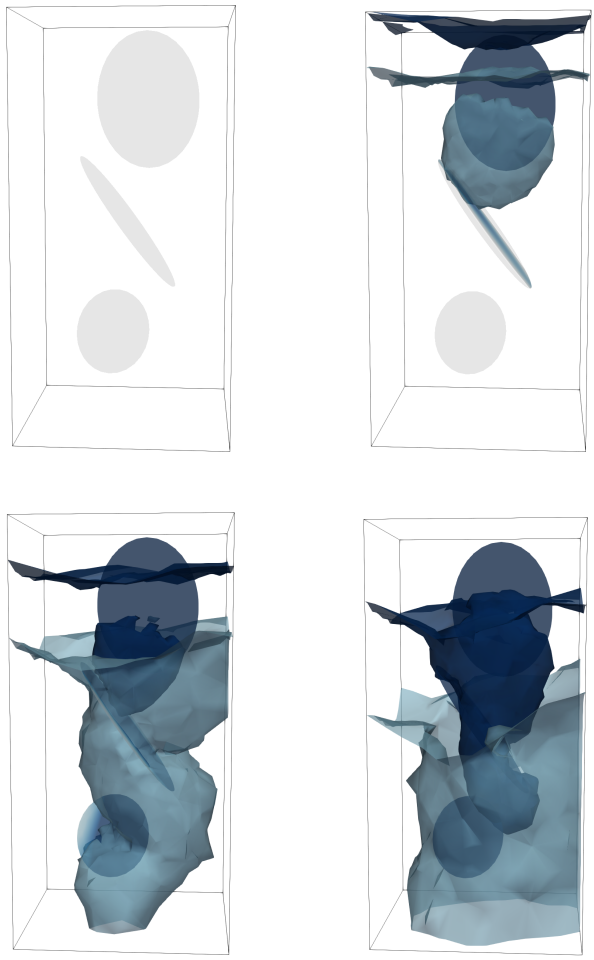

Figure 3.16: Saturation for Case 4 with two-dimensional fractures in a three-dimensional porous medium. Visualized are two contour levels at S=0.1 and S=0.4 for $t \in \{0.0, 0.2, 0.6, 1.0\}$.

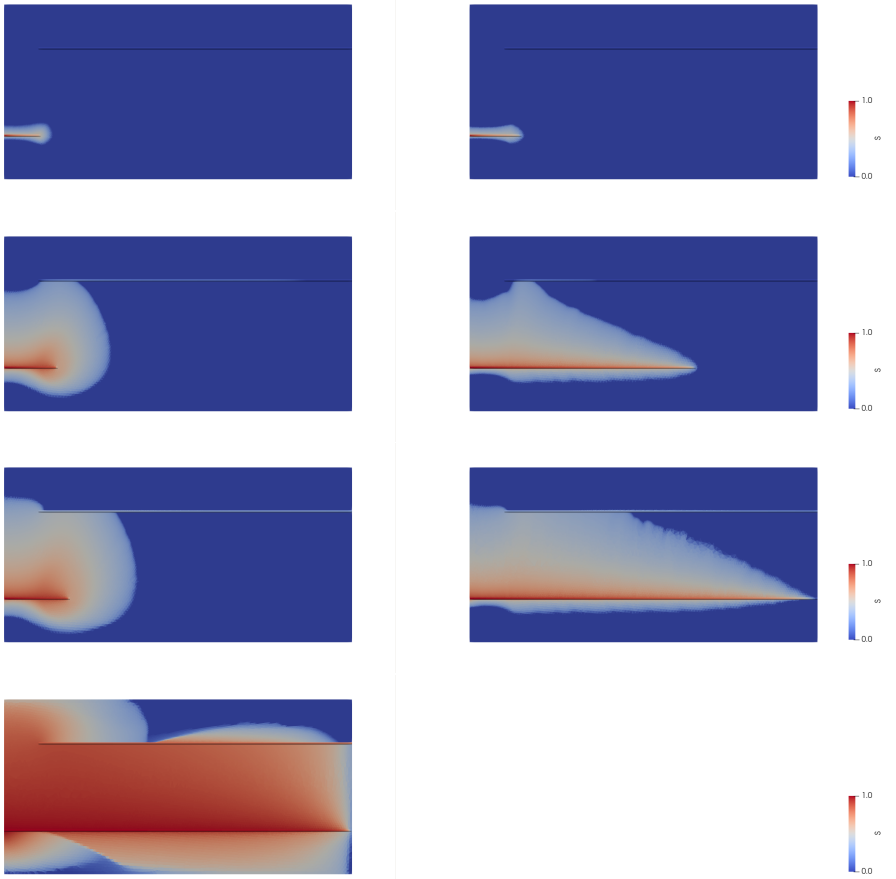

Figure 3.17: Saturation distribution for Case 5 with two interfering fractures and a tip propagating at different speeds. Visualized is s=0.1 (left) and s=1.0 (right) at $T = 0.1, 1.5, 1.8$ *and* 18 *(only* $s = 0.1$*) seconds from top to bottom.*

3.5.7 Bifurcating Fracture Network

Let us apply our method to a more complex fracture propagation scenario where fracture tips also bifurcate. In this example, the movement of the tips and the time of bifurcation is fully prescribed by a randomized generator. If one fracture crosses another, the network is topologically connected again. We can clearly observe how the fluid flow follows the propagating fracture paths, cf. Figure 3.18 and 3.19. Furthermore, the mesh adaptation is visualized which refines the grid around the propagating, lower-dimensional fracture network.

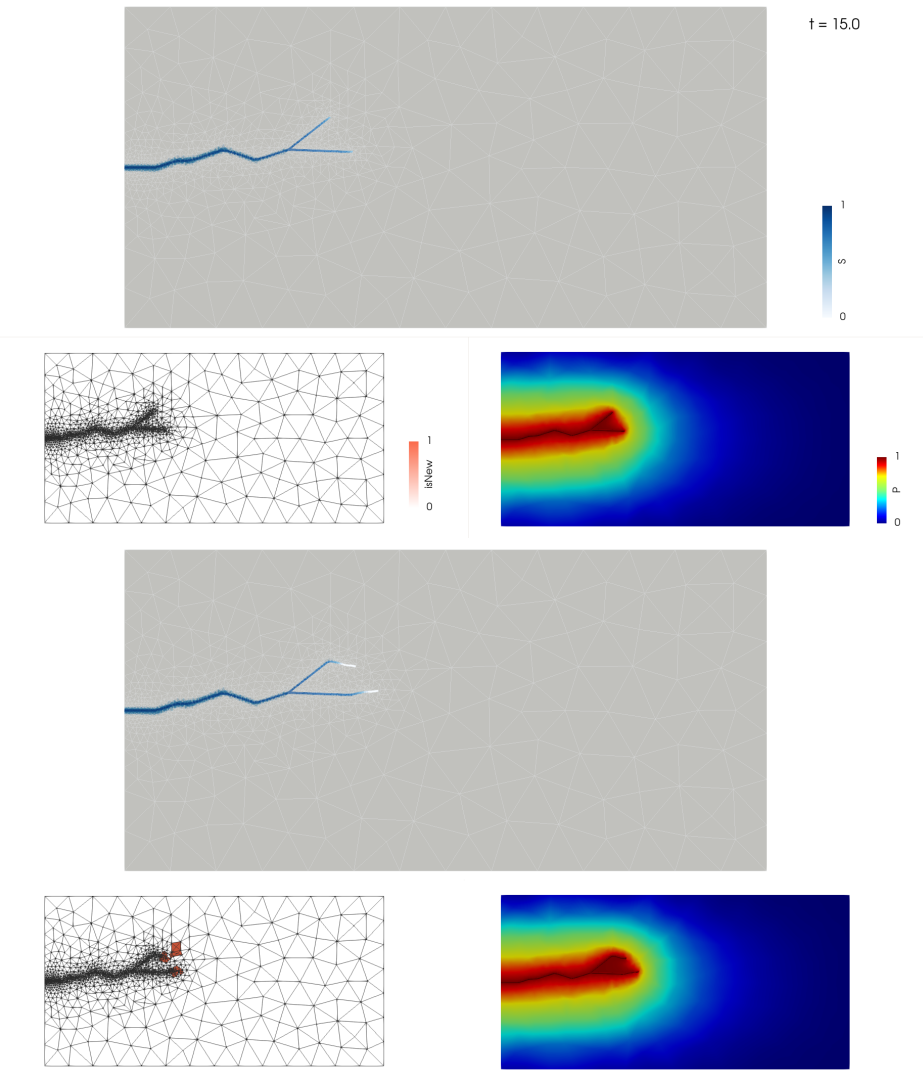

Figure 3.18: Two-phase flow in a randomly generated fracture propagation scenario with bifurcations. Visualized is the saturation, the mesh and the pressure at time steps 150 *and* 159.

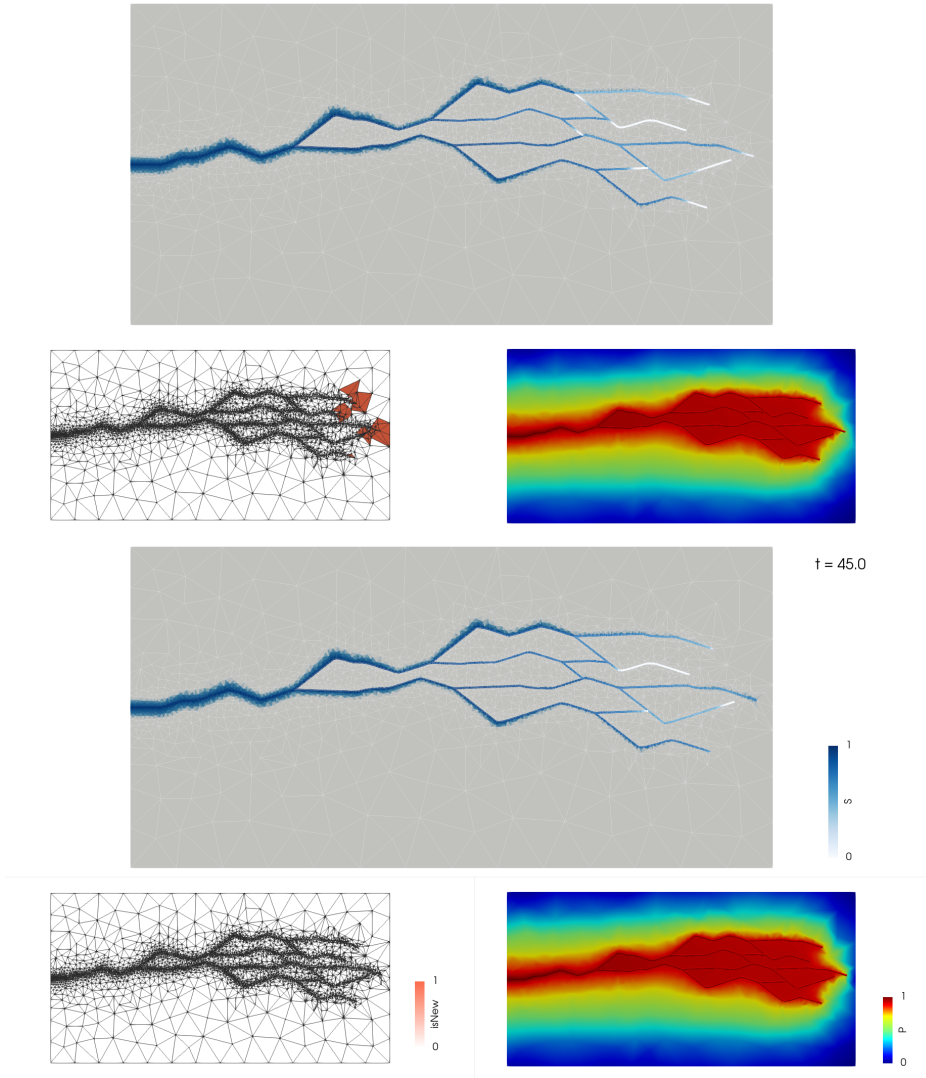

Figure 3.19: (continued) *Time steps* 429 *and* 450.

Modeling Flow in Porous Media with Fractures of Varying Aperture

4

The content of the following chapter led to the manuscript ”Flow in Porous Media with Fractures of Varying Aperture” submitted to ”SIAM Journal on Scientific Computing” [22]. All source code and the data of the simulation results have been published [42]. Most of the ideas are mine and the Dune-MMesh module is the basis for the implementation of the numerical scheme. Maximilian Hörl performed the numerical calculations and worked out some of the theoretical details.

In this chapter, the derivation of a generalized mixed-dimensional model for single-phase flow in fractured porous media is presented that incorporates the effect of non-constant fracture apertures. Dune-MMesh with its Python bindings, presented in Chapter 2, was crucial for the implementation of the corresponding mixed-dimensional discontinuous Galerkin discretization. The implementation has been used to validate the new model against a full-dimensional reference solution.

4.1 Introduction

As already described in Chapter 1, a common macroscopic modeling approach for flow in fractured porous media is discrete fracture modeling where fractures

are described explicitly as $(n-1)$-dimensional interfaces between n-dimensional bulk domains [3, 9, 43, 47, 51]. In contrast to a full-dimensional representation of fractures, this avoids thin full-dimensional subdomains which require highly resolved grids in numerical methods. Typically, discrete fracture models are based on the idealized conception of a planar fracture geometry with constant aperture. In this case, the resulting reduced model is not able to account for curvilinear fractures and, for instance, it does not properly incorporate the effect of surface roughness. Instead, it might be advantageous to describe the geometry of a fracture by spatially varying aperture functions. In this chapter, we describe an approach to model fractures as lower-dimensional manifolds that includes the effect of non-constant apertures.

Let us consider single-phase flow in a fractured porous medium governed by Darcy's law, cf. (1.1). We suggest a new mixed-dimensional model that accounts for asymmetric fractures with spatially varying aperture and, thereby, propose an extension and alternative derivation of a model well-known in literature [51] that was derived for fractures with constant aperture. For the derivation of the new model, we proceed from a domain-decomposed system for Darcy's flow with a full-dimensional fracture as proposed in [51]. In contrast, we employ a weak formulation of the model when averaging across the fracture which allows to address the central issue of non-constant apertures. In fact, the central issue is that the normal vectors at the internal boundaries of the initial full-dimensional fracture are generally not aligned with the normal vector of the $(n-1)$-dimensional fracture and depend on the aperture gradients instead.

Section 4.2 introduces the initial model problem with full-dimensional fracture in a weak formulation. In Section 4.3, we present the derivation of the new reduced model with a lower-dimensional fracture that accounts for a spatially varying aperture. The reduced model is summarized and discussed in Section 4.4. Section 4.5 introduces a discontinuous Galerkin (DG) discretization of the new model. Finally, we present numerical results in Section 4.6.

4.2 Darcy Flow with Full-Dimensional Fracture

Let $\Omega \subset \mathbb{R}^n, n \geq 2$, be a bounded domain that is occupied by an n-dimensional porous medium. We suppose that the single-phase flow in Ω is governed by Darcy's law and mass conservation, cf. Section 1.3.1. In this section, we neglect gravity and the symmetric and positive definite permeability matrix $\mathbf{K} = \mathbf{K}(\mathbf{x}) \in \mathbb{R}^{n\times n}$ $[\mathrm{m}^3\,\mathrm{s}\,\mathrm{kg}^{-1}]$ is assumed to include the dynamic viscosity of the fluid. For the sake of simplicity, we will impose homogeneous Dirichlet boundary conditions, but the extension to the inhomogeneous case and Neumann boundary conditions is straight forward. Then, a weak formulation of the Darcy system (1.1) is given by the following problem. Find $p \in H_0^1(\Omega)$ such that

$$\int_\Omega \mathbf{K}\nabla p \cdot \nabla\phi \,\mathrm{d}V = \int_\Omega q\phi \,\mathrm{d}V \qquad \text{for all } \phi \in H_0^1(\Omega).$$

Considering the case of a single fracture as an n-dimensional open subdomain $\Omega_\mathrm{f} \subset \Omega$ crossing the entire domain Ω, the domain Ω is cut into two disjoint connected subdomains Ω_1 and Ω_2, i.e., $\Omega \setminus \overline{\Omega}_\mathrm{f} = \Omega_1 \dot\cup \Omega_2$. Moreover, we suppose that the fracture domain Ω_f can be parameterized by a hyperplane Γ and two functions $d_i : \Gamma \to \mathbb{R},\ i \in \{1, 2\}$, which describe the aperture of the fracture on the left and right side of Γ such that

$$\Omega_\mathrm{f} = \big\{\gamma + \lambda\mathbf{n} \in \Omega \,\big|\, \gamma \in \Gamma,\ \lambda \in (-d_1(\gamma), d_2(\gamma))\big\}. \tag{4.1}$$

In Eq. (4.1), the vector $\mathbf{n}$ denotes the unit normal of the hyperplane Γ that points into the direction of Ω_2. Further, we write $d := d_1 + d_2 > 0$ for the total aperture of the fracture. We only require the total aperture d to be positive, not the functions d_1 and d_2, i.e, the hyperplane Γ is not necessarily required to be fully immersed within the fracture domain Ω_f. This is, in particular, convenient for the description of curvilinear fractures. Without loss of generality, the hyperplane Γ is represented by

$$\Gamma = \{\mathbf{x} \in \Omega \mid \mathbf{n} \cdot \mathbf{x} = 0\}.$$

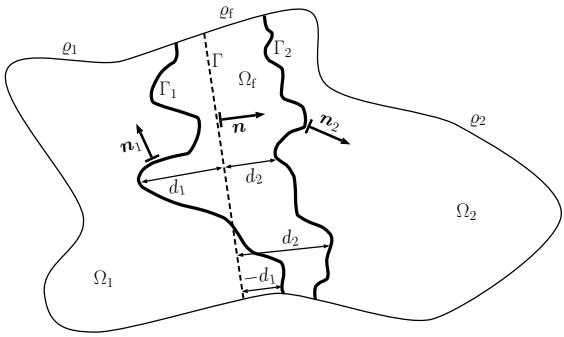

Figure 4.1: Sketch of the geometry for the full-dimensional Darcy problem (4.2).

In addition, we denote by $\rho_i := \partial\Omega_i \cap \partial\Omega$ the exterior boundary of the overall domain Ω inside the subdomain Ω_i for $i \in \{1, 2, \mathrm{f}\}$ and by $\Gamma_i := \partial\Omega_i \cap \partial\Omega_\mathrm{f}$ the interface between the bulk domain Ω_i and the fracture domain Ω_f for $i \in \{1, 2\}$. The specified geometric situation is sketched schematically in Figure 4.1. We remark that it is required that the connecting lines between the interfaces Γ_1 and Γ_2 along $\mathbf{n}$ exist and are contained in the fracture domain Ω_f.

Next, for $i \in \{1, 2, \mathrm{f}\}$ and functions $f : \Omega \to \cdot$ and $\bar{f} : \partial\Omega \to \cdot$, we introduce the notation

$$f_i := f\big|_{\Omega_i} \quad \text{and} \quad \bar{f}_i := \bar{f}\big|_{\rho_i}.$$

Following a domain decomposition approach, this allows us to reformulate the Darcy problem (1.1) as

$$-\operatorname{div}(\mathbf{K}_i \nabla p_i) = q_i \qquad \text{in } \Omega_i, \quad i \in \{1, 2, \mathrm{f}\}, \tag{4.2a}$$

$$p_i = 0 \qquad \text{on } \rho_i, \quad i \in \{1, 2, \mathrm{f}\}, \tag{4.2b}$$

$$p_i = p_\mathrm{f} \qquad \text{on } \Gamma_i, \quad i \in \{1, 2\}, \tag{4.2c}$$

$$\mathbf{K}_i \nabla p_i \cdot \mathbf{n}_i = \mathbf{K}_\mathrm{f} \nabla p_\mathrm{f} \cdot \mathbf{n}_i \qquad \text{on } \Gamma_i, \quad i \in \{1, 2\}. \tag{4.2d}$$

Here, for $i \in \{1, 2\}$, we denote by $\mathbf{n}_i$ the unit normal to the interface Γ_i that points into the bulk domain Ω_i. More specifically, $\mathbf{n}_1$ and $\mathbf{n}_2$ can be expressed by

$$\mathbf{n}_1 = \frac{-\mathbf{n} - \nabla d_1}{\sqrt{1 + |\nabla d_1|^2}}, \qquad \mathbf{n}_2 = \frac{\mathbf{n} - \nabla d_2}{\sqrt{1 + |\nabla d_2|^2}}.$$

Next, we set up a weak formulation for the domain-decomposed Darcy problem in Eq. (4.2). For $i \in \{1, 2, \mathrm{f}\}$, we define the space V_i by

$$V_i := \left\{ p_i \in H^1_{0,\rho_i}(\Omega_i) \;\middle|\; \mathbf{K}_i \nabla p_i \in H_{\mathrm{div}}(\Omega_i) \right\},$$

where H^1_{0,ρ_i} denotes the Sobolev space with homogeneous Dirichlet boundary condition on ρ_i and

$$H_{\mathrm{div}}(\Omega) = \{\mathbf{u} \in L^2(\Omega) \mid \operatorname{div} \mathbf{u} \in L^2(\Omega)\}.$$

Further, we define the domain-decomposed spaces

$$V_{\mathrm{dd}} := \left\{ (p_1, p_2, p_\mathrm{f}) \in \bigtimes_{i=1,2,\mathrm{f}} V_i \;\middle|\; p_i = p_\mathrm{f} \text{ a.e. on } \Gamma_i,\ i \in \{1, 2\} \right\}, \tag{4.3}$$

$$\Phi_{\mathrm{dd}} := \bigtimes_{i=1,2,\mathrm{f}} H^1_{0,\rho_i}(\Omega_i).$$

Then, a weak formulation of the domain-decomposed Darcy problem (4.2) is given by the following problem. Find $p = (p_1, p_2, p_\mathrm{f}) \in V_{\mathrm{dd}}$ such that

$$\mathscr{B}_{\mathrm{dd}}(p, \phi) = \mathscr{L}_{\mathrm{dd}}(\phi) \qquad \text{for all } \phi = (\phi_1, \phi_2, \phi_\mathrm{f}) \in \Phi_{\mathrm{dd}}. \tag{4.4}$$

In Eq. (4.4), given $p = (p_1, p_2, p_\mathrm{f}) \in V_{\mathrm{dd}}$ and $\phi = (\phi_1, \phi_2, \phi_\mathrm{f}) \in \Phi_{\mathrm{dd}}$, the bilinear form $\mathscr{B}_{\mathrm{dd}} : V_{\mathrm{dd}} \times \Phi_{\mathrm{dd}} \to \mathbb{R}$ and the linear form $\mathscr{L}_{\mathrm{dd}} : \Phi_{\mathrm{dd}} \to \mathbb{R}$ are defined by

$$\mathscr{B}_{\mathrm{dd}}(p, \phi) := \sum_{i=1,2,\mathrm{f}} \int_{\Omega_i} \mathbf{K}_i \nabla p_i \cdot \nabla \phi_i \, \mathrm{d}V - \sum_{i=1,2} \int_{\Gamma_i} \left[\phi_\mathrm{f} - \phi_i\right] \mathbf{K}_i \nabla p_i \cdot \mathbf{n}_i \, \mathrm{d}\sigma, \tag{4.5a}$$

$$\mathscr{L}_{\mathrm{dd}}(\phi) := \sum_{i=1,2,\mathrm{f}} \int_{\Omega_i} q_i \phi_i \, \mathrm{d}V. \tag{4.5b}$$

For the well-posedness of this weak formulation we refer to [21].

4.3 Derivation of a Reduced Model

Proceeding from the weak domain-decomposed Darcy problem (4.4), we will derive a new reduced model in which the fracture cutting the domain Ω is solely described by the hyperplane Γ between the two bulk subdomains Ω_1 and Ω_2. The reduced model is obtained by introducing fracture-averaged effective quantities, splitting integrals over Ω_f into a surface integral over Γ and a line integral in normal direction, and transforming integrals over the interfaces Γ_i into integrals over Γ. Two coupling conditions on Γ can be obtained by approximating curve integrals across the fracture domain Ω_f using a quadrature rule and polynomial interpolation.

4.3.1 Geometrical Setting and Notation

We start by expanding the normal vector $\mathbf{n}$ of the hyperplane Γ to an orthonormal basis $\mathscr{N} := (\mathbf{n}, \boldsymbol{\tau}_1, \dots, \boldsymbol{\tau}_{n-1})$ in the space $\mathbb{R}^n$. Further, we write the position vector $\mathbf{x}$ as

$$\mathbf{x} = \eta \mathbf{n} + \sum_{i=1}^{n-1} t_i \boldsymbol{\tau}_i =: (\eta, t_1, \dots, t_{n-1})_{\mathscr{N}}^\top = \left(\eta, \mathbf{t}^\top\right)_{\mathscr{N}}^\top.$$

Then, for a function f defined on Ω, we introduce the notation

$$f(\mathbf{x}) =: f(\eta, t_1, \dots, t_{n-1}) = f(\eta, \mathbf{t}), \tag{4.6}$$

If f in Eq. (4.6) is a function defined on Γ, we usually omit the first argument and write $f(\mathbf{x}) = f(0, \mathbf{t}) =: f(\mathbf{t})$. Besides, we define the maximum aperture D by

$$D := \sup\{ d(\mathbf{t}) \,|\, (0, \mathbf{t}^\top)^\top_{\mathscr{N}} \in \Gamma \}.$$

In addition, we introduce the notation

$$f^1\big|_{\Gamma_1}(\mathbf{t}) = f^1\big|_{\Gamma_1}(t_1, \dots, t_{n-1}) := f^1(-d_1(\mathbf{t}), \mathbf{t}), \tag{4.7a}$$

$$f^2\big|_{\Gamma_2}(\mathbf{t}) = f^2\big|_{\Gamma_2}(t_1, \dots, t_{n-1}) := f^2(d_2(\mathbf{t}), \mathbf{t}). \tag{4.7b}$$

Then, for $i \in \{1, 2\}$, a surface integral over Γ_i can be transformed into an integral over Γ according to the relation

$$\int_{\Gamma_i} f^i \,\mathrm{d}\sigma = \int_\Gamma f^i\big|_{\Gamma_i} \sqrt{1 + |\nabla d_i|^2} \,\mathrm{d}\sigma. \tag{4.8}$$

It is convenient to introduce jump and average operators across Γ. Let $f : \Omega \to \mathbb{R}$ and $\mathbf{F} : \Omega \to \mathbb{R}^n$, and fix $(0, \mathbf{t}^\top)^\top_{\mathscr{N}} \in \Gamma$. Using the notation from Eq. (4.7), we define by

$$[\![f]\!](\mathbf{t}) := f\big|_{\Gamma_2}(\mathbf{t}) - f\big|_{\Gamma_1}(\mathbf{t}), \tag{4.9a}$$

$$[\![\mathbf{F}]\!](\mathbf{t}) := \mathbf{F}\big|_{\Gamma_1}(\mathbf{t}) \cdot [\mathbf{n} + \nabla d_1(\mathbf{t})] - \mathbf{F}\big|_{\Gamma_2}(\mathbf{t}) \cdot [\mathbf{n} - \nabla d_2(\mathbf{t})] \tag{4.9b}$$

the jump operators of f and $\mathbf{F}$ and by

$$\{\!\{f\}\!\}(\mathbf{t}) := \frac{1}{2}\Big(f\big|_{\Gamma_1}(\mathbf{t}) + f\big|_{\Gamma_2}(\mathbf{t}) \Big), \tag{4.10a}$$

$$\{\!\{\mathbf{F}\}\!\}(\mathbf{t}) := \frac{1}{2}\Big(\mathbf{F}\big|_{\Gamma_1}(\mathbf{t}) \cdot [\mathbf{n} + \nabla d_1(\mathbf{t})] + \mathbf{F}\big|_{\Gamma_2}(\mathbf{t}) \cdot [\mathbf{n} - \nabla d_2(\mathbf{t})] \Big) \tag{4.10b}$$

the average operators of f and $\mathbf{F}$ across Γ. For vector-valued functions, the jump and average operators explicitly depend on the geometry of the fracture since they involve gradients of the aperture functions d_1 and d_2.

It is evident that a reduced model cannot capture all information from the full-dimensional model (4.4). In particular, inside the fracture domain Ω_f, we will restrict ourselves to a subspace of test functions

$$\Phi_f := \left\{ \phi_f \in H^1_{0,\rho_f}(\Omega_f) \;\middle|\; \partial_\eta \phi_f = 0 \right\} \subsetneq H^1_{0,\rho_f}(\Omega_f), \tag{4.11}$$

i.e., we will only consider test functions $\phi_f \in \Phi_f$ that are invariant perpendicular to Γ. We introduce new reduced quantities on the interface Γ that are obtained by averaging along straight lines perpendicular to Γ in Ω_f. Specifically, for $(0, \mathbf{t}^\top)^\top_{\mathcal{N}} \in \Gamma$, we define the average pressure p_Γ inside the fracture, the total source term q_Γ, and, for any test function $\phi_f \in \Phi_f$, the averaged test function ϕ_Γ by

$$p_\Gamma(\mathbf{t}) := \frac{1}{d(\mathbf{t})} \int_{-d_1(\mathbf{t})}^{d_2(\mathbf{t})} p_f(\eta, \mathbf{t}) \, \mathrm{d}\eta, \tag{4.12a}$$

$$q_\Gamma(\mathbf{t}) := \int_{-d_1(\mathbf{t})}^{d_2(\mathbf{t})} q_f(\eta, \mathbf{t}) \, \mathrm{d}\eta, \tag{4.12b}$$

$$\phi_\Gamma(\mathbf{t}) := \frac{1}{d(\mathbf{t})} \int_{-d_1(\mathbf{t})}^{d_2(\mathbf{t})} \phi_f(\eta, \mathbf{t}) \, \mathrm{d}\eta. \tag{4.12c}$$

Then, due to the definition of the space Φ_f in Eq. (4.11), we have $\phi_\Gamma(\mathbf{t}) = \phi_f(\eta, \mathbf{t})$ for almost all $(\eta, \mathbf{t}^\top)^\top_{\mathcal{N}} \in \Omega_f$. Further, we define the effective permeability $\mathbf{K}_\Gamma$ of the fracture as the mean of $\mathbf{K}_f$ in normal direction, i.e.,

$$\mathbf{K}_\Gamma(\mathbf{t}) := \frac{1}{d(\mathbf{t})} \int_{-d_1(\mathbf{t})}^{d_2(\mathbf{t})} \mathbf{K}_f(\eta, \mathbf{t}) \, \mathrm{d}\eta. \tag{4.13a}$$

Then, for $(\eta, \mathbf{t}^\top)^\top_{\mathcal{N}} \in \Omega_f$, we have

$$\mathbf{K}_f(\eta, \mathbf{t}) = \mathbf{K}_\Gamma(\mathbf{t}) + \mathcal{O}(d(\mathbf{t})) \tag{4.13b}$$

if $\mathbf{K}_f$ is continuously differentiable with respect to η. For any $(0, \mathbf{t}^\top)^\top_{\mathcal{N}} \in \Gamma$, we denote by $\mathbf{r}_\mathbf{t} : (-d_1(\mathbf{t}), d_2(\mathbf{t})) \to \mathbb{R}^n$ a continuously differentiable path such

that

$$\mathbf{r}_\mathbf{t}(-d_1(\mathbf{t})) = \left(-d_1(\mathbf{t}),\, \mathbf{t}^\top\right)_{\mathscr{M}}^\top, \qquad \mathbf{r}_\mathbf{t}(d_2(\mathbf{t})) = \left(d_2(\mathbf{t}),\, \mathbf{t}^\top\right)_{\mathscr{M}}^\top, \tag{4.14a}$$

$$\dot{\mathbf{r}}_\mathbf{t}(-d_1(\mathbf{t})) = -\mathbf{n}_1(\mathbf{t})\sqrt{1 + |\nabla d_1(\mathbf{t})|^2}, \qquad \dot{\mathbf{r}}_\mathbf{t}(d_2(\mathbf{t})) = \mathbf{n}_2(\mathbf{t})\sqrt{1 + |\nabla d_2(\mathbf{t})|^2}. \tag{4.14b}$$

Additionally, we assume that $\dot{\mathbf{r}}_\mathbf{t}(s) = \frac{\mathrm{d}}{\mathrm{d}s}\mathbf{r}_\mathbf{t}(s)$ is an eigenvector of the permeability $\mathbf{K}_\mathrm{f}(\mathbf{r}_\mathbf{t}(s))$ with eigenvalue $K_\mathrm{f}^\perp(\mathbf{r}_\mathbf{t}(s))$ for $s \in (-d_1(\mathbf{t}), d_2(\mathbf{t}))$. Then, we can define the effective permeability $K_\Gamma^\perp$ in normal direction as the mean value

$$K_\Gamma^\perp(\mathbf{t}) \coloneqq \frac{1}{L(\mathbf{r}_\mathbf{t})} \int_{\mathbf{r}_\mathbf{t}} K_\mathrm{f}^\perp \,\mathrm{d}r, \tag{4.15a}$$

where $L(\mathbf{r}_\mathbf{t})$ denotes the arc length of the path $\mathbf{r}_\mathbf{t}$. Further, we have

$$K_\mathrm{f}^\perp(\mathbf{r}_\mathbf{t}(s)) = K_\Gamma^\perp(\mathbf{t}) + \mathcal{O}(d(\mathbf{t})) \tag{4.15b}$$

for $s \in (-d_1(\mathbf{t}), d_2(\mathbf{t}))$ if $K_\mathrm{f}^\perp \circ \mathbf{r}_\mathbf{t}$ is continuously differentiable.

4.3.2 Averaging Across the Fracture

Starting from the weak formulation (4.4) of the domain-decomposed Darcy problem (4.2), we derive a relation that governs the effective pressure p_Γ inside the reduced fracture Γ.

Let $\phi_\mathrm{f} \in \Phi_\mathrm{f}$. By splitting the integral over Ω_f in Eq. (4.5b) into an integral over Γ and a line integral in normal direction, we obtain

$$\int_{\Omega_\mathrm{f}} q_\mathrm{f}\phi_\mathrm{f} \,\mathrm{d}V = \int_\Gamma \phi_\mathrm{f} \int_{-d_1(\mathbf{t})}^{d_2(\mathbf{t})} q_\mathrm{f} \,\mathrm{d}\eta\mathrm{d}\mathbf{t} = \int_\Gamma q_\Gamma\phi_\Gamma \,\mathrm{d}\sigma. \tag{4.16}$$

Likewise, splitting the integral over Ω_f in Eq. (4.5a) and using Eq. (4.13) results in

$$\begin{aligned}\int_{\Omega_\mathrm{f}} \mathbf{K}_\mathrm{f}\nabla p_\mathrm{f}\cdot\nabla\phi_\mathrm{f}\,\mathrm{d}V &= \int_\Gamma \nabla\phi_\mathrm{f}\cdot\int_{-d_1(\mathbf{t})}^{d_2(\mathbf{t})} \mathbf{K}_\mathrm{f}\nabla p_\mathrm{f}\,\mathrm{d}\eta\mathrm{d}\mathbf{t}\\ &= \int_\Gamma \mathbf{K}_\Gamma\nabla\phi_\mathrm{f}\cdot\int_{-d_1(\mathbf{t})}^{d_2(\mathbf{t})} \nabla p_\mathrm{f}\,\mathrm{d}\eta\mathrm{d}\mathbf{t} \;+\; \mathcal{O}(D)\\ &= \int_\Gamma \mathbf{K}_\Gamma\nabla\phi_\Gamma\cdot\Big[\nabla(d\,p_\Gamma) - p_1\big|_{\Gamma_1}\nabla d_1 - p_2\big|_{\Gamma_2}\nabla d_2\Big]\,\mathrm{d}\sigma\\ &\quad + \mathcal{O}(D).\end{aligned} \tag{4.17}$$

Here, we have utilized the continuity condition for the pressure from the definition of the space V_dd in Eq. (4.3) and we used Lemma 3.1 in [22] given the assumption that $d_1, d_2 \in W^{1,\infty}(\Gamma)\cap H^2(\Gamma)$. The calculation in Eq. (4.17) is exact if the permeability $\mathbf{K}_\mathrm{f}$ is constant perpendicular to Γ.

By transforming the integrals over the interfaces Γ_i in Eq. (4.4), $i\in\{1,2\}$, into integrals over Γ according to Eq. (4.8), one finds

$$\begin{aligned}&\sum_{i=1,2}\int_{\Gamma_i}\big[\phi_\mathrm{f}-\phi_i\big]\mathbf{K}_i\nabla p_i\cdot\mathbf{n}_i\,\mathrm{d}\sigma\\ &\qquad=\sum_{i=1,2}\int_\Gamma\Big[\phi_\Gamma-\phi_i\big|_{\Gamma_i}\Big](\mathbf{K}_i\nabla p_i)\big|_{\Gamma_i}\cdot\mathbf{n}_i\sqrt{1+|\nabla d_i|^2}\,\mathrm{d}\sigma.\end{aligned} \tag{4.18}$$

In summary, the weak formulation of the reduced model so far is given by the following problem. Find $p = (p_1, p_2, p_\Gamma)$ such that

$$\begin{aligned}\sum_{i=1,2} \int_{\Omega_i} \mathbf{K}_i \nabla p_i \cdot \nabla \phi_i \, \mathrm{d}V + \int_\Gamma \mathbf{K}_\Gamma \nabla \phi_\Gamma \cdot \Big[\nabla(d\, p_\Gamma) - \sum_{i=1,2} p_i\big|_{\Gamma_i} \nabla d_i \Big] \, \mathrm{d}\sigma \\ - \sum_{i=1,2} \int_\Gamma \Big[\phi_\Gamma - \phi_i\big|_{\Gamma_i} \Big] (\mathbf{K}_i \nabla p_i)\big|_{\Gamma_i} \cdot \mathbf{n}_i \sqrt{1 + |\nabla d_i|^2} \, \mathrm{d}\sigma \\ = \sum_{i=1,2} \int_{\Omega_i} q_i \phi_i \, \mathrm{d}V + \int_\Gamma q_\Gamma \phi_\Gamma \, \mathrm{d}\sigma\end{aligned} \tag{4.19}$$

holds for all test functions $\phi = (\phi_1, \phi_2, \phi_\Gamma)$.

Moreover, the weak problem in Eq. (4.19) corresponds to the following strong formulation. Find $p = (p_1, p_2, p_\Gamma)$ such that

$$-\operatorname{div}(\mathbf{K}_i \nabla p_i) = q_i \qquad \text{in } \Omega_i, \quad i \in \{1,2\}, \tag{4.20a}$$

$$-\operatorname{div}\Big[\mathbf{K}_\Gamma \Big(\nabla(d\, p_\Gamma) - \sum_{i=1,2} p_i\big|_{\Gamma_i} \nabla d_i \Big) \Big] = q_\Gamma - [\![\mathbf{K} \nabla p]\!] \qquad \text{in } \Gamma, \tag{4.20b}$$

$$p_i = 0 \qquad \text{on } \rho_i, \quad i \in \{1,2\}, \tag{4.20c}$$

$$p_\Gamma = 0 \qquad \text{on } \partial\Gamma. \tag{4.20d}$$

The system as it is in Eq. (4.20) is decoupled. Given a solution (p_1, p_2) of the bulk problem (4.20a), (4.20c), which, so far, is independent of p_Γ, the effective pressure p_Γ inside the fracture is obtained from the solution of the problem (4.20b), (4.20d). However, in order to obtain a well-posed problem, we will supplement the bulk problem (4.20a), (4.20c) by two additional boundary conditions at the fracture Γ. In general, these conditions will rely on the effective pressure p_Γ inside the fracture, which is why we refer to them as coupling conditions.

4.3.3 Coupling Conditions

4.3.3.1 First Coupling Condition

For the derivation of a first coupling condition, we fix $(0, \mathbf{t}^\top)^\top_{\mathcal{N}} \in \Gamma$ and consider the line integral of $\mathbf{K}_\mathrm{f}\nabla p_\mathrm{f}$ along the curve $\mathbf{r_t}$ specified in Eq. (4.14). Applying the trapezoidal rule yields

$$\int_{\mathbf{r_t}} \mathbf{K}_\mathrm{f}\nabla p_\mathrm{f} \cdot \mathrm{d}\mathbf{r} = d(\mathbf{t})\{\!\{\mathbf{K}\nabla p\}\!\}(\mathbf{t}) + \mathcal{O}\big(D^3\big), \tag{4.21}$$

where we use continuity condition (4.2d). Using that $\dot{\mathbf{r}}_\mathbf{t}$ is an eigenvector of $\mathbf{K}_\mathrm{f}$, we obtain

$$\begin{aligned}\int_{\mathbf{r_t}} \mathbf{K}_\mathrm{f}\nabla p_\mathrm{f} \cdot \mathrm{d}\mathbf{r} &= \int_{-d_1(\mathbf{t})}^{d_2(\mathbf{t})} \mathbf{K}_\mathrm{f}(\mathbf{r_t}(s))\nabla p_\mathrm{f}(\mathbf{r_t}(s)) \cdot \dot{\mathbf{r}}_\mathbf{t}(s)\,\mathrm{d}s \\ &= K_\Gamma^\perp(\mathbf{t}) \int_{\mathbf{r_t}} \nabla p_\mathrm{f} \cdot \mathrm{d}\mathbf{r} \;+\; \mathcal{O}(D) = K_\Gamma^\perp(\mathbf{t})[\![p]\!](\mathbf{t}) \;+\; \mathcal{O}(D),\end{aligned} \tag{4.22}$$

where we use Eq. (4.15) and the pressure continuity from Eq. (4.3). Combining the Eqs. Eqs. (4.21) and (4.22) suggests the coupling condition

$$\{\!\{\mathbf{K}\nabla p\}\!\} = \frac{K_\Gamma^\perp}{d}[\![p]\!]. \tag{4.23}$$

By Equation (4.9b), the coupling condition (4.23) depends on the gradients of the aperture functions d_1 and d_2.

4.3.3.2 Second Coupling Condition

For the derivation of a second coupling condition along Γ, we fix $(0, \mathbf{t}^\top)^\top_{\mathcal{N}} \in \Gamma$ and consider the definition of the mean pressure p_Γ in Eq. (4.12a).

Let $\psi_1, \psi_2 \in \mathscr{C}^\infty(\mathbb{R})$ with $0 \le \psi_1, \psi_2 \le 1$, $\psi_1(-d_1(\mathbf{t})) = \psi_2(d_2(\mathbf{t})) = 1$, and $\operatorname{supp}(\psi_1) \subset B_1(-d_1(\mathbf{t}))$, $\operatorname{supp}(\psi_2) \subset B_1(d_2(\mathbf{t}))$ where $B_r(z) \coloneqq (z-r, z+r)$. Further, for $\epsilon > 0$, define

$$\psi_1^\epsilon(s) \coloneqq \psi_1\bigg(\frac{s + d_1(\mathbf{t})}{\epsilon} - d_1(\mathbf{t})\bigg), \qquad \psi_2^\epsilon(s) \coloneqq \psi_2\bigg(\frac{s - d_2(\mathbf{t})}{\epsilon} + d_2(\mathbf{t})\bigg)$$

such that $\operatorname{supp}\big(\psi_1^\epsilon\big) \subset B_\epsilon(-d_1(\mathbf{t}))$ and $\operatorname{supp}\big(\psi_2^\epsilon\big) \subset B_\epsilon(d_2(\mathbf{t}))$. In addition, for $\epsilon > 0$, let Ψ_1^ϵ and Ψ_2^ϵ be antiderivatives of ψ_1^ϵ and ψ_2^ϵ such that $\Psi_1^\epsilon(s) \to 0$ for $s \to \infty$ and $\Psi_2^\epsilon(s) \to 0$ for $s \to -\infty$. Then, for $s \in (-d_1(\mathbf{t}), d_2(\mathbf{t}))$, we define the curve $\mathbf{c}_\mathbf{t}^\epsilon : (-d_1(\mathbf{t}), d_2(\mathbf{t})) \to \mathbb{R}^n$ by

$$\mathbf{c}_\mathbf{t}^\epsilon(s) \coloneqq \big(s, \mathbf{t}^\top\big)_{\mathscr{M}}^\top + \Psi_1^\epsilon(s)\nabla d_1(\mathbf{t}) - \Psi_2^\epsilon(s)\nabla d_2(\mathbf{t}).$$

We remark that, since Ψ_1^ϵ and Ψ_2^ϵ vanish as $\epsilon \to 0$, the curve $\mathbf{c}_\mathbf{t}^\epsilon$ runs inside the fracture domain Ω_f if $\epsilon > 0$ is sufficiently small. Besides, one can observe that

$$\dot{\mathbf{c}}_\mathbf{t}^\epsilon(s) = \mathbf{n} + \psi_1^\epsilon(s)\nabla d_1(\mathbf{t}) - \psi_2^\epsilon(s)\nabla d_2(\mathbf{t})$$

for $s \in (-d_1(\mathbf{t}), d_2(\mathbf{t}))$. Consequently, if $\epsilon > 0$ is sufficiently small, we have

$$\dot{\mathbf{c}}_\mathbf{t}^\epsilon(-d_1(\mathbf{t})) = -\mathbf{n}_1\sqrt{1 + |\nabla d_1(\mathbf{t})|^2}, \qquad \dot{\mathbf{c}}_\mathbf{t}^\epsilon(d_2(\mathbf{t})) = \mathbf{n}_2\sqrt{1 + |\nabla d_2(\mathbf{t})|^2}.$$

Further, assuming that p_f is bounded in $\overline{\Omega}_\mathrm{f}$, it is easy to see that

$$\frac{1}{d(\mathbf{t})}\int_{\mathbf{c}_\mathbf{t}^\epsilon} p_\mathrm{f}\,\mathrm{d}r \to p_\Gamma(\mathbf{t}) \qquad \text{for } \epsilon \to 0.$$

Next, we approximate the pressure p_f in Ω_f along the curve $\mathbf{c}_\mathbf{t}^\epsilon$ by means of the third-order Hermite interpolation polynomial $\pi_\mathbf{t}^\epsilon$ defined by the following conditions.

$$\pi_\mathbf{t}^\epsilon(-d_1(\mathbf{t})) = p_1\big|_{\Gamma_1}(\mathbf{t}), \tag{4.24a}$$

$$\pi^\epsilon_{\mathbf{t}}(d_2(\mathbf{t})) = p_2\big|_{\Gamma_2}(\mathbf{t}), \tag{4.24b}$$

$$\dot{\pi}^\epsilon_{\mathbf{t}}(-d_1(\mathbf{t})) = \nabla p_{\mathrm{f}}\big(\mathbf{c}^\epsilon_{\mathbf{t}}(s)\big) \cdot \dot{\mathbf{c}}^\epsilon_{\mathbf{t}}(s)\big|_{s=-d_1(\mathbf{t})}, \tag{4.24c}$$

$$\dot{\pi}^\epsilon_{\mathbf{t}}(d_2(\mathbf{t})) = \nabla p_{\mathrm{f}}\big(\mathbf{c}^\epsilon_{\mathbf{t}}(s)\big) \cdot \dot{\mathbf{c}}^\epsilon_{\mathbf{t}}(s)\big|_{s=d_2(\mathbf{t})}. \tag{4.24d}$$

Assuming that $K_{\mathrm{f}}^{\perp}\big|_{\Gamma_i}$ and $[\mathbf{K}_i \nabla p_i]\big|_{\Gamma_i}$ are continuous for $i \in \{1, 2\}$, we have

$$K_{\mathrm{f}}^{\perp}\big|_{\Gamma_i}(\mathbf{t} + \Delta\mathbf{t}) = K_{\mathrm{f}}^{\perp}\big|_{\Gamma_i}(\mathbf{t}) + \mathcal{O}\big(|\Delta\mathbf{t}|^0\big), \tag{4.25a}$$

$$[\mathbf{K}_i \nabla p_i]\big|_{\Gamma_i}(\mathbf{t} + \Delta\mathbf{t}) = [\mathbf{K}_i \nabla p_i]\big|_{\Gamma_i}(\mathbf{t}) + \mathcal{O}\big(|\Delta\mathbf{t}|^0\big) \tag{4.25b}$$

for $(0, \mathbf{t}^\top)^\top_{\mathcal{N}}$, $(0, \mathbf{t}^\top + \Delta\mathbf{t}^\top)^\top_{\mathcal{N}} \in \Gamma$. Thus, using Eq. (4.15) and Eq. (4.25), we can express the interpolation conditions (4.24c) and (4.24d) as

$$\dot{\pi}^\epsilon_{\mathbf{t}}(-d_1(\mathbf{t})) = -\frac{[\mathbf{K}_1 \nabla p_1]\big|_{\Gamma_1}(\mathbf{t})}{K_\Gamma^\perp(\mathbf{t})} \cdot \mathbf{n}_1(\mathbf{t}) \sqrt{1 + |\nabla d_1(\mathbf{t})|^2} + \mathcal{O}(D) + \mathcal{O}\big(\epsilon^0\big), \tag{4.26a}$$

$$\dot{\pi}^\epsilon_{\mathbf{t}}(d_2(\mathbf{t})) = \frac{[\mathbf{K}_2 \nabla p_2]\big|_{\Gamma_2}(\mathbf{t})}{K_\Gamma^\perp(\mathbf{t})} \cdot \mathbf{n}_2(\mathbf{t}) \sqrt{1 + |\nabla d_2(\mathbf{t})|^2} + \mathcal{O}(D) + \mathcal{O}\big(\epsilon^0\big). \tag{4.26b}$$

if $\epsilon > 0$ is sufficiently small. Further, for $s \in (-d_1(\mathbf{t}), d_2(\mathbf{t}))$, one has

$$\pi^\epsilon_{\mathbf{t}}(s) \coloneqq \sum_{i=0}^{3} \alpha^\epsilon_{\mathbf{t},i} s^i = p_{\mathrm{f}}\big(\mathbf{c}^\epsilon_{\mathbf{t}}(s)\big) + \mathcal{O}\big(D^4\big)$$

if p_{f} is four times continuously differentiable along $\mathbf{c}^\epsilon_{\mathbf{t}}$. Since the polynomial $\pi^\epsilon_{\mathbf{t}}$ is uniquely defined by the conditions in Eq. (4.24), we can determine explicit expressions for the coefficients $\alpha^\epsilon_{\mathbf{t},i}$, $i \in \{0, \dots, 3\}$. Specifically, we obtain

$$\alpha^\epsilon_{\mathbf{t},3} = \mathcal{O}\big(d(\mathbf{t})^{-1}\big) + \mathcal{O}\big(\epsilon^0\big),$$

$$\alpha^\epsilon_{\mathbf{t},2} = -\frac{1}{2K_\Gamma^\perp(\mathbf{t}) d(\mathbf{t})} [\![\mathbf{K} \nabla p]\!](\mathbf{t}) + \mathcal{O}\big(d(\mathbf{t})^0\big) + \mathcal{O}\big(\epsilon^0\big),$$

$$\alpha^\epsilon_{\mathbf{t},1} = \frac{1}{d(\mathbf{t})} [\![p]\!](\mathbf{t}) - \big[d_2(\mathbf{t}) - d_1(\mathbf{t})\big] \alpha_{\mathbf{t},2} + \mathcal{O}\big(d(\mathbf{t})\big) + \mathcal{O}\big(\epsilon^0\big),$$

$$\alpha^{\epsilon}_{\mathbf{t},0} = \{\!\{p\}\!\}(\mathbf{t}) - d_1(\mathbf{t})d_2(\mathbf{t})\alpha_{\mathbf{t},2} - \frac{d_2(\mathbf{t}) - d_1(\mathbf{t})}{2K_\Gamma^\perp(\mathbf{t})}\{\!\{\mathbf{K}\nabla p\}\!\}(\mathbf{t}) + \mathcal{O}\big(d(\mathbf{t})^2\big) + \mathcal{O}\big(\epsilon^0\big),$$

where we have utilized the first coupling condition (4.23) as well as Eq. (4.26). As a result, we can approximate the mean pressure p_Γ by

$$p_\Gamma(\mathbf{t}) = \lim_{\epsilon\to 0}\frac{1}{d(\mathbf{t})}\int_{\mathbf{c}^\epsilon_\mathbf{t}} p_\mathrm{f}\,\mathrm{d}r = \lim_{\epsilon\to 0}\frac{1}{d(\mathbf{t})}\int_{-d_1(\mathbf{t})}^{d_2(\mathbf{t})}\pi^\epsilon_\mathbf{t}(s)\,\mathrm{d}s + \mathcal{O}\big(D^4\big). \tag{4.28a}$$

With Simpson's rule, we have

$$\frac{1}{d(\mathbf{t})}\int_{-d_1(\mathbf{t})}^{d_2(\mathbf{t})}\pi^\epsilon_\mathbf{t}(s)\,\mathrm{d}s = \frac{1}{6}\left[\pi^\epsilon_\mathbf{t}(-d_1(\mathbf{t})) + 4\pi^\epsilon_\mathbf{t}\left(\frac{d_2(\mathbf{t}) - d_1(\mathbf{t})}{2}\right) + \pi^\epsilon_\mathbf{t}(d_2(\mathbf{t}))\right]. \tag{4.28b}$$

Now, substituting the explicit form of the polynomial $\pi^\epsilon_\mathbf{t}$ into Eq. (4.28) suggests the coupling condition

$$[\![\mathbf{K}\nabla p]\!] = \frac{12K_\Gamma^\perp}{d}\big(p_\Gamma - \{\!\{p\}\!\}\big). \tag{4.29}$$

We remark that, for a symmetric fracture with constant aperture, i.e., $d_1 = d_2 = d/2 \equiv \text{const.}$, the coupling conditions (4.23) and (4.29) coincide with the coupling conditions formulated in [51] for $\xi = \frac{2}{3}$. In fact, the general form of their coupling conditions is given by

$$\{\!\{\mathbf{K}\nabla p\}\!\} = \frac{K_\Gamma^\perp}{d}[\![p]\!], \qquad [\![\mathbf{K}\nabla p]\!] = \frac{4K_\Gamma^\perp}{(2\xi-1)d}\big(p_\Gamma - \{\!\{p\}\!\}\big) \tag{4.30}$$

with a coupling parameter $\xi > \frac{1}{2}$. The second coupling condition in Eq. (4.30) arises in [51] after a motivation of the cases $\xi = \frac{1}{2}, \xi = \frac{3}{4}$ and $\xi = 1$ by approximating the pressure and velocity inside or at the fracture by means of mean values or differential quotients. For $\xi = \frac{3}{4}$ and $\xi = 1$, this motivation does not immediately transfer to our situation with a fracture of varying aperture due to different normal vectors on the interfaces Γ_1, Γ_2, and Γ. Besides, the case $\xi = \frac{1}{2}$,

where $p_\Gamma = \{\!\{p\}\!\}$ is assumed, was found to be unstable [51]. Nonetheless, to highlight the analogy to the model in [51], we may also write our coupling condition in Eq. (4.29) with a general coupling parameter $\xi > \frac{1}{2}$ and, for convenience, introduce the abbreviation

$$\beta_\Gamma := \frac{4K_\Gamma^\perp}{(2\xi - 1)d}. \tag{4.31}$$

The derivation above labels the case $\xi = \frac{2}{3}$ as a reasonable choice in the sense that the unique lowest-order interpolation polynomial satisfying the conditions in Eq. (4.24) has been taken.

By rearranging Eqs. (4.23) and (4.29) and with β_Γ as defined in Eq. (4.31), we find that the coupling conditions can also be written as

$$\mathbf{K}_1 \nabla p_1\big|_{\Gamma_1} \cdot \mathbf{n}_1 \sqrt{1 + |\nabla d_1|^2} = \frac{\beta_\Gamma}{2}\big(\{\!\{p\}\!\} - p_\Gamma\big) - \frac{K_\Gamma^\perp}{d}[\![p]\!], \tag{4.32a}$$

$$\mathbf{K}_2 \nabla p_2\big|_{\Gamma_2} \cdot \mathbf{n}_2 \sqrt{1 + |\nabla d_2|^2} = \frac{\beta_\Gamma}{2}\big(\{\!\{p\}\!\} - p_\Gamma\big) + \frac{K_\Gamma^\perp}{d}[\![p]\!]. \tag{4.32b}$$

Then, the coupling conditions as given in Eq. (4.32) can be substituted directly into Eq. (4.18). This results in the relation

$$\begin{aligned} &- \sum_{i=1,2} \int_{\Gamma_i} \big[\phi_\mathrm{f} - \phi_i\big] \mathbf{K}_i \nabla p_i \cdot \mathbf{n}_i \,\mathrm{d}\sigma \\ &\quad = \int_\Gamma \frac{K_\Gamma^\perp}{d} [\![p]\!][\![\phi]\!] \,\mathrm{d}\sigma + \int_\Gamma \beta_\Gamma \big(p_\Gamma - \{\!\{p\}\!\}\big)\big(\phi_\Gamma - \{\!\{\phi\}\!\}\big) \,\mathrm{d}\sigma. \end{aligned} \tag{4.33}$$

Concluding the model derivation, we can now substitute Eq. (4.33) in Eq. (4.19) and summarize the resulting model.

4.4 Darcy Flow with Lower-Dimensional Fracture

In this section, we summarize the new reduced model derived in Section 4.3. Besides, in Section 4.4.1, we introduce different variants of the new model with a simplified, less accurate description of the varying fracture aperture. The geometry of the reduced problem is sketched schematically in Figure 4.2.

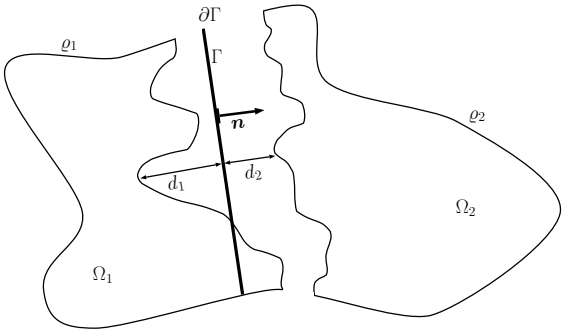

Figure 4.2: Sketch of the geometry for the reduced Darcy problem (4.34).

We define the solution and test function spaces

$$\Phi_b := \bigtimes_{i=1,2} H^1_{0,\rho_i}(\Omega_i), \qquad \Phi_\Gamma := H^1_0(\Gamma), \qquad \Phi := \Phi_b \times \Phi_\Gamma.$$

A weak formulation of the reduced interface model derived in Section 4.3 is given by the following problem. Find $p = (p_b, p_\Gamma) \in \Phi$ such that

$$\mathcal{A}(p, \phi) = \mathcal{R}(\phi) \qquad \text{for all } \phi = (\phi_b, \phi_\Gamma) \in \Phi. \tag{4.34}$$

For $p = (p_\mathrm{b}, p_\Gamma)$, $\phi = (\phi_\mathrm{b}, \phi_\Gamma) \in \Phi$ with $p_\mathrm{b} = (p_1, p_2)$, $\phi_\mathrm{b} = (\phi_1, \phi_2) \in \Phi_\mathrm{b}$, the bilinear form $\mathscr{A} : \Phi \times \Phi \to \mathbb{R}$ and the linear form $\mathscr{R} : \Phi \to \mathbb{R}$ are defined by

$$\begin{aligned}\mathscr{A}(p, \phi) &\coloneqq \mathscr{A}_\mathrm{b}(p_\mathrm{b}, \phi_\mathrm{b}) + \mathscr{A}_\Gamma(p, \phi_\Gamma) + \mathscr{J}(p, \phi),\\ \mathscr{R}(\phi) &\coloneqq \mathscr{R}_\mathrm{b}(\phi_\mathrm{b}) + \mathscr{R}_\Gamma(\phi_\Gamma).\end{aligned}$$

The bilinear forms $\mathscr{A}_\mathrm{b} : \Phi_\mathrm{b} \times \Phi_\mathrm{b} \to \mathbb{R}$, $\mathscr{A}_\Gamma : \Phi \times \Phi_\Gamma \to \mathbb{R}$, and $\mathscr{J} : \Phi \times \Phi \to \mathbb{R}$, which in this order represent the flow in the bulk domain, the effective flow inside the fracture, and the lower-dimensional coupling between them, as well as the corresponding linear forms $\mathscr{R}_\mathrm{b} : \Phi_\mathrm{b} \to \mathbb{R}$ and $\mathscr{R}_\Gamma : \Phi_\Gamma \to \mathbb{R}$, are given by

$$\begin{aligned}\mathscr{A}_\mathrm{b}(p_\mathrm{b}, \phi_\mathrm{b}) &\coloneqq \sum_{i=1,2} \int_{\Omega_i} \mathbf{K}_i \nabla p_i \cdot \nabla \phi_i \,\mathrm{d}V,\\ \mathscr{A}_\Gamma(p, \phi_\Gamma) &\coloneqq \int_\Gamma \mathbf{K}_\Gamma \nabla \phi_\Gamma \cdot \Big[\nabla(d\, p_\Gamma) - p_1\big|_{\Gamma_1} \nabla d_1 - p_2\big|_{\Gamma_2} \nabla d_2\Big] \,\mathrm{d}\sigma,\\ \mathscr{J}(p, \phi) &\coloneqq \int_\Gamma \frac{K_\Gamma^\perp}{d} [\![p_\mathrm{b}]\!][\![\phi_\mathrm{b}]\!] \,\mathrm{d}\sigma + \int_\Gamma \beta_\Gamma \big(p_\Gamma - \{\!\{p_\mathrm{b}\}\!\}\big)\big(\phi_\Gamma - \{\!\{\phi_\mathrm{b}\}\!\}\big) \,\mathrm{d}\sigma,\\ \mathscr{R}_\mathrm{b}(\phi_\mathrm{b}) &\coloneqq \sum_{i=1,2} \int_{\Omega_i} q_i \phi_i \,\mathrm{d}V,\\ \mathscr{R}_\Gamma(\phi_\Gamma) &\coloneqq \int_\Gamma q_\Gamma \phi_\Gamma \,\mathrm{d}\sigma.\end{aligned}$$

The well-posedness of this model is proved in [22] and, for the sake of completeness, we give a short summary of the result.

For $i \in \{1, 2\}$, let $q_i \in L^2(\Omega_i)$, $q_\Gamma \in L^2(\Gamma)$, and $d_1, d_2 \in W^{1,\infty}(\Gamma)$ with $d_1 + d_2 > d_\mathrm{min}$ for a constant $d_\mathrm{min} > 0$. Besides, let $\mathbf{K}_i \in L^\infty(\Omega_i; \mathbb{R}^{n\times n})$ for $i \in \{1, 2\}$ and $\mathbf{K}_\Gamma \in L^\infty(\Gamma; \mathbb{R}^{n\times n})$ as well as $K_\Gamma^\perp \in L^\infty(\Gamma)$. In addition, let $\mathbf{K}_1$, $\mathbf{K}_2$, and $\mathbf{K}_\Gamma$ be symmetric and uniformly elliptic, i.e., there exist constants $\kappa_\mathrm{max}^\mathrm{b} \geq \kappa_\mathrm{min}^\mathrm{b} > 0$

and $\kappa_{\max}^{\Gamma} \geq \kappa_{\min}^{\Gamma} > 0$ such that

$$\kappa_{\min}^{\mathrm{b}} |\mathbf{z}|_2^2 \leq \mathbf{K}_i(\mathbf{x}_i)\mathbf{z} \cdot \mathbf{z} \leq \kappa_{\max}^{\mathrm{b}} |\mathbf{z}|_2^2,$$
$$\kappa_{\min}^{\Gamma} |\mathbf{z}|_2^2 \leq \mathbf{K}_{\Gamma}(\mathbf{t})\mathbf{z} \cdot \mathbf{z} \leq \kappa_{\max}^{\Gamma} |\mathbf{z}|_2^2$$

for all $\mathbf{z} \in \mathbb{R}^n$. Besides, we require that

$$\kappa_{\min}^{\Gamma} \leq K_{\Gamma}^{\perp}(\mathbf{t}) \leq \kappa_{\max}^{\Gamma}.$$

Then, the following theorem states the well-posedness of our new model.

Theorem 4.1: *Given the condition*

$$\left[\frac{\kappa_{\max}^{\Gamma}}{\kappa_{\min}^{\Gamma}}\right]^2 \frac{D}{d_{\min}} \left[(2\xi - 1) \| \nabla d \|_{L^{\infty}(\Gamma;\mathbb{R}^n)}^2 + \| \nabla d_1 - \nabla d_2 \|_{L^{\infty}(\Gamma;\mathbb{R}^n)}^2 \right] < 16, \tag{4.38}$$

the reduced Darcy problem (4.34) *has a unique solution* $(p_{\mathrm{b}}, p_{\Gamma}) \in \Phi$.

Proof. See [22]. □

In case of a classical solution, a corresponding strong formulation of the weak system Eq. (4.34) is given by

$$-\operatorname{div}(\mathbf{K}_i \nabla p_i) = q_i \qquad \text{in } \Omega_i,\ i \in \{1,2\}, \tag{4.39a}$$
$$-\operatorname{div}\left[\mathbf{K}_{\Gamma}\Big(\nabla(d p_{\Gamma}) - \sum_{i=1,2} p_i|_{\Gamma_i} \nabla d_i\Big)\right] = q_{\Gamma} - [\![\mathbf{K}\nabla p]\!] \qquad \text{in } \Gamma, \tag{4.39b}$$
$$\{\!\{\mathbf{K}\nabla p\}\!\} = \frac{K_{\Gamma}^{\perp}}{d} [\![p]\!] \qquad \text{on } \Gamma, \tag{4.39c}$$
$$[\![\mathbf{K}\nabla p]\!] = \beta_{\Gamma}\big(p_{\Gamma} - \{\!\{p\}\!\}\big) \qquad \text{on } \Gamma, \tag{4.39d}$$
$$p_i = 0 \qquad \text{on } \rho_i,\ i \in \{1,2\}, \tag{4.39e}$$
$$p_{\Gamma} = 0 \qquad \text{on } \partial\Gamma. \tag{4.39f}$$

Note that the quantity

$$\mathbf{u}_\Gamma := -\mathbf{K}_\Gamma\Big(\nabla(d p_\Gamma) - p_1\big|_{\Gamma_1}\nabla d_1 - p_2\big|_{\Gamma_2}\nabla d_2\Big)$$

in Eq. (4.39b) takes the role of the effective velocity inside the reduced fracture Γ. Further, for a symmetric fracture with constant aperture, i.e., $d_1 = d_2 = d/2 \equiv$ const., the model in Eq. (4.39) coincides with the model proposed in [51]. Therefore, the new model Eq. (4.39) can be viewed as an extension of the model in [51] for general asymmetric fractures with spatially varying aperture.

4.4.1 Model Variants

According to the derivation of the reduced model (4.39) in Section 4.3, there should be a gap between the bulk domains Ω_1 and Ω_2 on either side of the fracture as illustrated in Figure 4.2. However, for numerical calculations in practice, the bulk domains Ω_1 and Ω_2 are usually rectified such that the interface Γ is part of their boundary, i.e., $\partial\Omega_1^{\text{rct.}} \cap \partial\Omega_2^{\text{rct.}} = \overline{\Gamma}$. The corresponding reduced model with simplified bulk geometry is obtained from the model in Eq. (4.39) by replacing the bulk domains Ω_1 and Ω_2 with the domains

$$\Omega_1^{\text{rct.}} = \big\{\gamma + \lambda\mathbf{n} \in \Omega \,\big|\, \gamma \in \Gamma,\ \lambda < 0\big\}, \tag{4.40a}$$

$$\Omega_2^{\text{rct.}} = \big\{\gamma + \lambda\mathbf{n} \in \Omega \,\big|\, \gamma \in \Gamma,\ \lambda > 0\big\}. \tag{4.40b}$$

This kind of bulk rectification requires one to neglect the terms containing aperture gradients ∇d_1, ∇d_2 in the coupling conditions (4.39c) and (4.39d). The geometrical difference between the full-dimensional model in Eq. (4.2), the reduced model in Eq. (4.39), and the corresponding reduced model with bulk rectification is illustrated in Figure 4.3.

In contrast to the model in [51], the new model Eq. (4.39) contains aperture gradients ∇d_1, ∇d_2 in the effective flow equation (4.39b) and in the coupling conditions (4.39c) and (4.39d). In order to study the effect of the aperture gradients

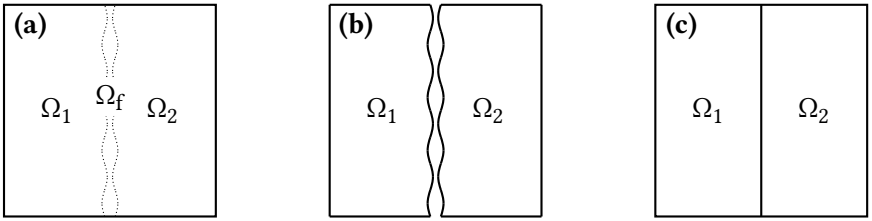

*Figure 4.3: Bulk domains **(a)** in the full-dimensional model* (4.2)*, **(b)** in the reduced model* (4.39) *without rectification, **(c)** in the reduced model* (4.39) *with rectification.*

as well as the effect of a rectified bulk geometry as discussed above, we define simplified variants of the reduced model (4.39). On the one hand, we can neglect the aperture gradients ∇d_1, ∇d_2 in Eq. (4.39b), i.e., Eq. (4.39b) is replaced by the equation

$$-\operatorname{div}\left[\mathbf{K}_\Gamma \nabla (d p_\Gamma)\right] = q_\Gamma - [\![\mathbf{K}\nabla p]\!] \qquad \text{in } \Gamma. \tag{4.41}$$

On the other hand, the aperture gradients ∇d_1, ∇d_2 could be neglected in the coupling conditions (4.39c) and (4.39d), which corresponds to a rectification of the bulk domains Ω_1 and Ω_2. This suggests to define the following model variants.

Model I: The new model (4.39) without change.

Model I-R: The model (4.39) with the bulk domains Ω_1 and Ω_2 replaced by the rectified domains $\Omega_1^{\text{rct.}}$ and $\Omega_2^{\text{rct.}}$ from Eq. (4.40). Terms containing ∇d_1, ∇d_2 are neglected in Eqs. (4.39c) and (4.39d) but not in Eq. (4.39b).

Model II: The model (4.39) with unchanged bulk domains. Terms containing ∇d_1, ∇d_2 are neglected in Eq. (4.39b) but not in Eq. (4.39c) and (4.39d).

Model II-R: The model (4.39) with the bulk domains Ω_1 and Ω_2 replaced by the rectified domains $\Omega_1^{\text{rct.}}$ and $\Omega_2^{\text{rct.}}$ from Eq. (4.40). Terms containing ∇d_1, ∇d_2 are neglected completely.

Model II-R is basically the model proposed in [51] with the only difference that the aperture d in Eq. (4.41) can still be a function that is not necessarily constant as assumed in [51]. In particular, in model II-R, there is no information about the aperture gradients ∇d_1, ∇d_2 and the bulk geometry at the fracture. In contrast, the new model I includes all this information. The models I-R and II are intermediate models.

4.5 Discontinuous Galerkin Discretization

In this section, following [10], we formulate three DG discretizations, one for the full-dimensional model (4.2), one for the reduced models II and II-R, and one for the reduced models I and I-R from Section 4.4, where, in this order, each discretization extends the previous one. The choice of a DG scheme as discretization for the reduced fracture models comes naturally as it can easily deal with discontinuities across the fracture and suits the formulation of the coupling conditions (4.39c) and (4.39d) in terms of jump and average operators. For simplicity, we assume that Ω is a polytopal domain. Besides, we consider inhomogeneous Dirichlet boundary conditions for all discretizations.

4.5.1 Meshes and Notation

Let $\mathcal{I}$ be the index family of bulk domains, i.e., $\mathcal{I} = \{1, 2, \mathrm{f}\}$ in the full-dimensional case and $\mathcal{I} = \{1, 2\}$ for the reduced models. Further, for $i \in \mathcal{I}$, let $\mathcal{T}_{h,i}$ be a polytopal mesh of the bulk domain Ω_i of open and disjoint elements $T_{h,i} \in \mathcal{T}_{h,i}$. Besides, we write $\mathcal{T}_h := \bigcup_{i\in\mathcal{I}} \mathcal{T}_{h,i}$ for the overall bulk mesh. Moreover, we denote by $\mathcal{F}_h$ the facet grid induced by $\mathcal{T}_h$ which contains all one-codimensional intersections between grid elements $T \in \mathcal{T}_h$ with neighboring grid elements or the domain boundary $\partial\Omega$. For the reduced models, we denote by $\mathcal{F}_h^\Gamma$ a one-codimensional mesh of the interface Γ induced by the bulk grids $\mathcal{T}_{h,1}$ and $\mathcal{T}_{h,2}$. Specifically, for the reduced models I-R and II-R, i.e., in case of a reduced model with rectified bulk domains as defined in Eq. (4.40), the fracture mesh $\mathcal{F}_h^\Gamma$ is part of the facet grid $\mathcal{F}_h$ and given by

$$\mathcal{F}_h^\Gamma := \{F \in \mathcal{F}_h \mid F \subset \Gamma\}. \tag{4.42a}$$

In the other case, for the reduced models I and II without bulk rectification, the fracture mesh $\mathcal{F}_h^\Gamma$ can be defined by

$$\mathcal{F}_h^\Gamma := \left\{ \mathscr{P}_\Gamma(F_1) \cap \mathscr{P}_\Gamma(F_2) \;\middle|\; F_i = \partial T_i \cap \Gamma_i \neq \emptyset,\ T_i \in \mathcal{T}_{h,i} \ \text{ for } i \in \{1,2\} \right\}. \tag{4.42b}$$

In Eq. (4.42b), $\mathscr{P}_\Gamma$ denotes the orthogonal projection onto the hyperplane Γ given by

$$\mathscr{P}_\Gamma : \Omega \to \Omega, \ \ \left(\eta, \mathbf{t}^\top\right)_{\mathcal{N}}^\top \mapsto \left(0, \mathbf{t}^\top\right)_{\mathcal{N}}^\top. \tag{4.43}$$

Regarding the facet grid $\mathcal{F}_h$, we distinguish between the set of facets $\mathcal{F}_h^\partial$ on the domain boundary $\partial\Omega$ and the set of facets $\mathcal{F}_h^\circ$ in the interior of Ω excluding the interface grid $\mathcal{F}_h^\Gamma$, i.e., we can write $\mathcal{F}_h$ as the disjoint union

$$\mathcal{F}_h = \mathcal{F}_h^\circ \,\dot\cup\, \mathcal{F}_h^\partial \,\dot\cup\, \left(\mathcal{F}_h^\Gamma \cap \mathcal{F}_h\right).$$

In addition, for the reduced models, we denote by $\mathscr{E}_h^\Gamma$ the set of edges of the interface grid $\mathscr{F}_h^\Gamma$, i.e., the set of two-codimensional intersections between elements $F \in \mathscr{F}_h^\Gamma$ or the boundary $\partial\Gamma$. More specifically, we distinguish between the set of edges $\mathscr{E}_h^\circ$ in the interior of the interface Γ and the set of edges $\mathscr{E}_h^\partial$ at the boundary $\partial\Gamma$ such that $\mathscr{E}_h^\Gamma = \mathscr{E}_h^\circ \dot\cup \mathscr{E}_h^\partial$.

For $A \subset \mathbb{R}^n$, let $\mathscr{P}_k(A)$ denote the space of polynomials on A whose degrees do not exceed $k \in \mathbb{N}_0$. Then, we define the finite-dimensional function spaces

$$\Phi_h^\mathrm{b} := \{\phi_h \in L^2(\Omega) \mid \phi_h|_T \in \mathscr{P}_{k_T}(T) \text{ for all } T \in \mathscr{T}_h\}, \tag{4.44a}$$

$$\Phi_h^\Gamma := \{\phi_h^\Gamma \in L^2(\Gamma) \mid \phi_h^\Gamma|_F \in \mathscr{P}_{k_F}(F) \text{ for all } F \in \mathscr{F}_h^\Gamma\}, \tag{4.44b}$$

$$\Phi_h := \Phi_h^\mathrm{b} \times \Phi_h^\Gamma \tag{4.44c}$$

with individual polynomial degrees $k_T \in \mathbb{N}$ and $k_F \in \mathbb{N}$ for each bulk element $T \in \mathscr{T}_h$ and interface element $F \in \mathscr{F}_h^\Gamma$.

For an internal facet $S \in \mathscr{F}_h^\circ$ (or $\mathscr{E}_h^\circ$, respectively) with adjacent mesh elements $M_1 \neq M_2 \in \mathscr{M}_h$ and outer normals $\mathbf{n}_{M_1}$ and $\mathbf{n}_{M_2}$, we define

$$[\![\phi_h]\!]|_S := \phi_h|_{M_1}\mathbf{n}_{M_1} + \phi_h|_{M_2}\mathbf{n}_{M_2}, \tag{4.45a}$$

$$[\![\boldsymbol{\zeta}_h]\!]|_S := \boldsymbol{\zeta}_h|_{M_1} \cdot \mathbf{n}_{M_1} + \boldsymbol{\zeta}_h|_{M_2} \cdot \mathbf{n}_{M_2}, \tag{4.45b}$$

$$\{\!\{\phi_h\}\!\}|_S := \frac{1}{2}\Big(\phi_h|_{M_1} + \phi_h|_{M_2}\Big), \tag{4.45c}$$

$$\{\!\{\boldsymbol{\zeta}_h\}\!\}|_S := \frac{1}{2}\Big(\boldsymbol{\zeta}_h|_{M_1} + \boldsymbol{\zeta}_h|_{M_2}\Big), \tag{4.45d}$$

for $\phi_h \in \Phi_h^\mathrm{b}$ and $\boldsymbol{\zeta}_h \in \left[\Phi_h^\mathrm{b}\right]^n$ (or $\phi_h \in \Phi_h^\Gamma$ and $\boldsymbol{\zeta}_h \in \left[\Phi_h^\Gamma\right]^n$, respectively).

4.5.2 Discrete Model with Full-Dimensional Fracture

Let g denote the given pressure on the boundary $\partial\Omega$ for the Dirichlet condition in Eq. (4.2b). Then, in order to obtain a DG discretization of the full-dimensional

model (4.2), we define the bilinear form $\mathscr{A}_h^{\mathrm{b}} : \Phi_h^{\mathrm{b}} \times \Phi_h^{\mathrm{b}} \to \mathbb{R}$ associated with bulk flow and the corresponding linear form $\mathscr{R}_h^{\mathrm{b}} : \Phi_h^{\mathrm{b}} \to \mathbb{R}$ by

$$\begin{aligned}\mathscr{A}_h^{\mathrm{b}}(p_h^{\mathrm{b}}, \phi_h^{\mathrm{b}}) = &\sum_{T_\in \mathscr{T}_h} \int_T \mathbf{K}\nabla p_h^{\mathrm{b}} \cdot \nabla \phi_h^{\mathrm{b}} \,\mathrm{d}V + \sum_{F\in\mathscr{F}_h^\circ} \int_F \mu_F [\![p_h^{\mathrm{b}}]\!] \cdot [\![\phi_h^{\mathrm{b}}]\!] \,\mathrm{d}\sigma \\ &- \sum_{F\in\mathscr{F}_h^\circ} \int_F \Big[[\![\phi_h^{\mathrm{b}}]\!] \cdot \{\!\{ \mathbf{K}\nabla p_h^{\mathrm{b}} \}\!\} + [\![p_h^{\mathrm{b}}]\!] \cdot \{\!\{ \mathbf{K}\nabla \phi_h^{\mathrm{b}} \}\!\} \Big] \,\mathrm{d}\sigma \qquad (4.46a) \\ &+ \sum_{F\in\mathscr{F}_h^\partial} \int_F \mu_F^{\mathrm{b}} p_h^{\mathrm{b}} \phi_h^{\mathrm{b}} \,\mathrm{d}\sigma - \sum_{F\in\mathscr{F}_h^\partial} \int_F \big[p_h^{\mathrm{b}} \mathbf{K}\nabla \phi_h^{\mathrm{b}} + \phi_h^{\mathrm{b}} \mathbf{K}\nabla p_h^{\mathrm{b}} \big] \cdot \mathrm{d}\boldsymbol{\sigma}, \\ \mathscr{R}_h^{\mathrm{b}}(\phi_h^{\mathrm{b}}) = &\sum_{T\in\mathscr{T}_h} \int_T q \phi_h^{\mathrm{b}} \,\mathrm{d}V + \sum_{F\in\mathscr{F}_h^\partial} \Big[\int_F \mu_F^{\mathrm{b}} g \phi_h^{\mathrm{b}} \,\mathrm{d}\sigma - \int_F g \mathbf{K}\nabla \phi_h^{\mathrm{b}} \cdot \mathrm{d}\boldsymbol{\sigma} \Big]. \qquad (4.46b)\end{aligned}$$

In Eq. (4.46), μ_F^{b} is a penalty parameter which we define facet-wise, for $F \in \mathscr{F}_h \setminus \mathscr{F}_h^\Gamma$, by

$$\mu_F^{\mathrm{b}} := \begin{cases} \mu_0^{\mathrm{b}} \frac{(k_T+1)(k_T+n)}{h_T}, & \text{if } F \in \mathscr{F}_h^\partial,\ F \subset \partial T,\ T \in \mathscr{T}_h, \\ \mu_0^{\mathrm{b}} \max\limits_{T=T_1,T_2} \Big\{ \frac{(k_T+1)(k_T+n)}{h_T} \Big\}, & \text{if } F \in \mathscr{F}_h^\circ,\ F \subset \partial T_1 \cap \partial T_2,\ T_1 \neq T_2 \in \mathscr{T}_h. \end{cases} \qquad (4.47)$$

In Eq. (4.47), $\mu_0^{\mathrm{b}} > 0$ is a sufficiently large constant and h_T denotes the maximum edge length of a grid element $T \in \mathscr{T}_h$.

A DG discretization of the full-dimensional system (4.2) is now given by the following problem. Find $p_h^{\mathrm{b}} \in \Phi_h^{\mathrm{b}}$ such that

$$\mathscr{A}_h^{\mathrm{b}}(p_h^{\mathrm{b}}, \phi_h^{\mathrm{b}}) = \mathscr{R}_h^{\mathrm{b}}(\phi_h^{\mathrm{b}}) \qquad \text{for all } \phi_h^{\mathrm{b}} \in \Phi_h^{\mathrm{b}}. \qquad (4.48)$$

4.5.3 Discrete Model with Lower-Dimensional Fracture

Let g_Γ and $g = (g_1, g_2)$ denote the given pressure functions on the external boundaries for the Dirichlet conditions (4.39e) and (4.39f). We continue to extend

the DG discretization in Eq. (4.48) to a discretization of the reduced interface models I, I-R, II, and II-R from Section 4.4. Here, the models I and I-R and the models II and II-R can be treated together, respectively, since they only differ in their bulk geometry with otherwise identical weak formulation.

We define the bilinear forms $\mathscr{A}_h^{\Gamma_1} : \Phi_h^\Gamma \times \Phi_h^\Gamma \to \mathbb{R}$, $\mathscr{A}_h^{\Gamma_2} : \Phi_h^\mathrm{b} \times \Phi_h^\Gamma$, and $\mathscr{I}_h : \Phi_h \times \Phi_h \to \mathbb{R}$, as well as the linear form $\mathscr{R}_h^\Gamma : \Phi_h^\Gamma \to \mathbb{R}$, by

$$\begin{aligned}
\mathscr{A}_h^{\Gamma_1}(p_h^\Gamma, \phi_h^\Gamma) = &\sum_{F\in F_h^\Gamma}\int_F \mathbf{K}_\Gamma \nabla(d\, p_h^\Gamma)\cdot\nabla\phi_h^\Gamma \,\mathrm{d}\sigma + \sum_{E\in\mathscr{E}_h^\circ}\int_E \mu_E^\Gamma [\![p_h^\Gamma]\!]\cdot[\![\phi_h^\Gamma]\!]\,\mathrm{d}r \\
&- \sum_{E\in\mathscr{E}_h^\circ}\int_E \Big[[\![\phi_h^\Gamma]\!]\cdot\{\!\{\mathbf{K}_\Gamma\nabla(d\,p_h^\Gamma)\}\!\} + [\![d\,p_h^\Gamma]\!]\cdot\{\!\{\mathbf{K}_\Gamma\nabla\phi_h^\Gamma\}\!\}\Big]\,\mathrm{d}r \qquad (4.49a)\\
&+ \sum_{E\in\mathscr{E}_h^\partial}\Big[\int_E \mu_E^\Gamma p_h^\Gamma\phi_h^\Gamma\,\mathrm{d}r - \int_E\Big[\phi_h^\Gamma\mathbf{K}_\Gamma\nabla(d\,p_h^\Gamma) - d\,p_h^\Gamma\mathbf{K}_\Gamma\nabla\phi_h^\Gamma\Big]\cdot\mathrm{d}\mathbf{r}\Big],\\
\mathscr{A}_h^{\Gamma_2}(p_h^\mathrm{b}, \phi_h^\Gamma) = &-\sum_{F\in F_h^\Gamma}\int_F\Big[p_h^{(1)}\nabla d_1 + p_h^{(2)}\nabla d_2\Big]\cdot\mathbf{K}_\Gamma\nabla\phi_h^\Gamma\,\mathrm{d}\sigma \\
&+ \sum_{E\in\mathscr{E}_h^\circ}\int_E \{\!\{p_h^\mathrm{b}\}\!\}[\![\phi_h^\Gamma]\!]\cdot\mathbf{K}_\Gamma\nabla d\,\mathrm{d}r + \sum_{E\in\mathscr{E}_h^\partial}\int_E\phi_h^\Gamma\big[p_h^{(1)}\nabla d_1 + p_h^{(2)}\nabla d_2\big]\cdot\mathrm{d}\mathbf{r}, \qquad (4.49b)\\
\mathscr{I}_h(p_h,\phi_h) = &\sum_{F\in\mathscr{F}_h^\Gamma}\int_F \frac{K_\Gamma^\perp}{d}[\![p_h^\mathrm{b}]\!]\cdot[\![\phi_h^\mathrm{b}]\!]\,\mathrm{d}\sigma \\
&+ \sum_{F\in\mathscr{F}_h^\Gamma}\int_F \beta_\Gamma\big(p_h^\Gamma - \{\!\{p_h^\mathrm{b}\}\!\}\big)\big(\phi_h^\Gamma - \{\!\{\phi_h^\mathrm{b}\}\!\}\big)\,\mathrm{d}\sigma, \qquad (4.49c)\\
\mathscr{R}_h^\Gamma(\phi_h) = &\sum_{F\in F_h^\Gamma}\int_F q_\Gamma\phi_h^\Gamma\,\mathrm{d}\sigma + \sum_{E\in\mathscr{E}_h^\partial}\Big[\int_E \mu_\Gamma g_\Gamma\phi_h^\Gamma\,\mathrm{d}r - \int_E d\,g_\Gamma\mathbf{K}_\Gamma\nabla\phi_h^\Gamma\cdot\mathrm{d}\mathbf{r}\Big], \qquad (4.49d)
\end{aligned}$$

where $p_h = (p_h^\mathrm{b}, p_h^\Gamma)$, $\phi_h = (\phi_h^\mathrm{b}, \phi_h^\Gamma) \in \Phi_h$ with $p_h^\mathrm{b} = \big(p_h^{(1)}, p_h^{(2)}\big) \in \Phi_h^\mathrm{b}$. For the reduced models I and II without bulk rectification, the evaluation of bulk functions in Φ_h^b on the interface Γ in the Eqs. (4.49b) and (4.49c) is to be understood

in the sense of restrictions to the interfaces Γ_1 and Γ_2 as defined in Eq. (4.7). Besides, in Eq. (4.49a), μ_E^Γ is a penalty parameter on the interface Γ in analogy to Eq. (4.47).

A DG discretization of the the reduced interface models II and II-R is now given by the following problem. Find $p_h = (p_h^\mathrm{b}, p_h^\Gamma) \in \Phi_h$ such that

$$\mathscr{A}_h^\mathrm{b}(p_h^\mathrm{b}, \phi_h^\mathrm{b}) + \mathscr{A}_h^{\Gamma_1}(p_h^\Gamma, \phi_h^\Gamma) + \mathscr{J}_h(p_h, \phi_h) = \mathscr{R}_h^\mathrm{b}(\phi_h^\mathrm{b}) + \mathscr{R}_h^\Gamma(\phi_h^\Gamma) \tag{4.50}$$

holds for all $\phi_h = (\phi_h^\mathrm{b}, \phi_h^\Gamma) \in \Phi_h$.

Finally, a DG discretization of the reduced models I and I-R extending the discretization in Eq. (4.50) can be formulated as follows. Find $p_h = (p_h^\mathrm{b}, p_h^\Gamma) \in \Phi_h$ so that

$$\mathscr{A}_h^\mathrm{b}(p_h^\mathrm{b}, \phi_h^\mathrm{b}) + \mathscr{A}_h^{\Gamma_1}(p_h^\Gamma, \phi_h^\Gamma) + \mathscr{A}_h^{\Gamma_2}(p_h^\mathrm{b}, \phi_h^\Gamma) + \mathscr{J}_h(p_h, \phi_h) \tag{4.51}$$

$$= \mathscr{R}_h^\mathrm{b}(\phi_h^\mathrm{b}) + \mathscr{R}_h^\Gamma(\phi_h^\Gamma) \tag{4.52}$$

holds for all $\phi_h = (\phi_h^\mathrm{b}, \phi_h^\Gamma) \in \Phi_h$.

4.6 Numerical Experiments

In the following, we present a few numerical results to validate the new reduced interface model (4.39) and explore its capabilities. In particular, we investigate how the use of a simplified bulk geometry and the disregard of aperture gradients ∇d_1, ∇d_2 affects the accuracy of the reduced model. For this, numerical solutions of the reduced models I, I-R, II, and II-R from Section 4.4.1 are compared with a numerical reference solution of the full-dimensional model (4.2). Specifically, for the full-dimensional reference solution, the average pressure $p_\Gamma^\mathrm{ref.}$ across the fracture is computed according to Eq. (4.12a). Then, the different reduced models are assessed in terms of their solution for the effective pressure p_Γ

inside the fracture and its deviation from the averaged reference solution $p_\Gamma^{\text{ref.}}$, particularly, by calculating the discrete L^2-error over the interface Γ.

All subsequent test problems are performed on the computational domain $\Omega = (0,1)^n \subset \mathbb{R}^n$ with $n = 2$ or $n = 3$ and feature a single fracture with sinusoidal aperture that is represented by the interface $\Gamma = \{\mathbf{x} \in \Omega \mid x_1 = \frac{1}{2}\}$ in the reduced model (4.39) and its variants. For the reduced models, the coupling parameter ξ is chosen as $\xi = \frac{2}{3}$ as suggested by the derivation in Section 4.3. Further, all test problems feature a vanishing source term $q \equiv 0$ so that the flow is determined only by the choice of boundary conditions. In addition, the bulk permeability is defined as $\mathbf{K}_1 = \mathbf{K}_2 \equiv \mathbf{I}$, where $\mathbf{I} \in \mathbb{R}^{n\times n}$ denotes the identity matrix. The fracture permeability $\mathbf{K}_\text{f}$ differs depending on the test case.

The results in this section were obtained from an implementation of the DG schemes (4.48), (4.50), and (4.52) in Dune [11]. The program code is openly available [42]. Specifically, the implementation relies on Dune-MMesh [21], a grid module tailored for applications with interfaces. In particular, Dune-MMesh is a useful tool for mixed-dimensional models, such as the DG schemes (4.50) and (4.52), as it allows to export a predefined set of facets from the bulk grid as separate interface grid and provides coupled solution strategies to simultaneously solve bulk and interface schemes. Further, the implementation depends on Dune-Fem [28], a discretization module providing the capabilities to implement efficient solvers for a wide range of partial differential equations. We access it through its Python interface, where, using the Unified Form Language (UFL) [5], the description of models is close to their variational formulation.

4.6.1 Flow Perpendicular to a Fracture with Constant Total Aperture

4.6.1.1 Two-Dimensional Test Problem

For the first test problem, we consider a fracture with a serpentine geometry in the two-dimensional domain $\Omega = (0,1)^2$. Nonetheless, the fracture is chosen

such that it exhibits a constant total aperture d. Specifically, we define the aperture functions d_1 and d_2 by

$$d_1(x_2) = d_0 + \tfrac{1}{2} d_0 \sin(8\pi x_2), \qquad d_2(x_2) = d_0 - \tfrac{1}{2} d_0 \sin(8\pi x_2),$$

where $d_0 > 0$ is a free parameter. Then, the total aperture is constant and given by $d(x_2) = 2d_0$. Further, on the whole boundary $\partial\Omega$, we impose Dirichlet conditions and require the pressure p to be equal to $g(\mathbf{x}) = 1 - x_1$. Thus, the flow direction will be from left to right, perpendicular to the fracture. For the full-dimensional model (4.2), the permeability inside the fracture is defined by $\mathbf{K}_\mathrm{f} = \frac{1}{2}\mathbf{I}$. As a consequence, the effective fracture permeabilities in the reduced model (4.39) and its variants are given by $\mathbf{K}_\Gamma = \frac{1}{2}\mathbf{I}$ and $K_\Gamma^\perp = \frac{1}{2}$. In particular, the fracture is less permeable than the bulk domains Ω_1 and Ω_2. The fracture geometry and the resulting full-dimensional solution are illustrated in Figure 4.4 for the case of $d_0 = 10^{-1}$. The relatively large aperture is intended to show the capabilities of our new model.

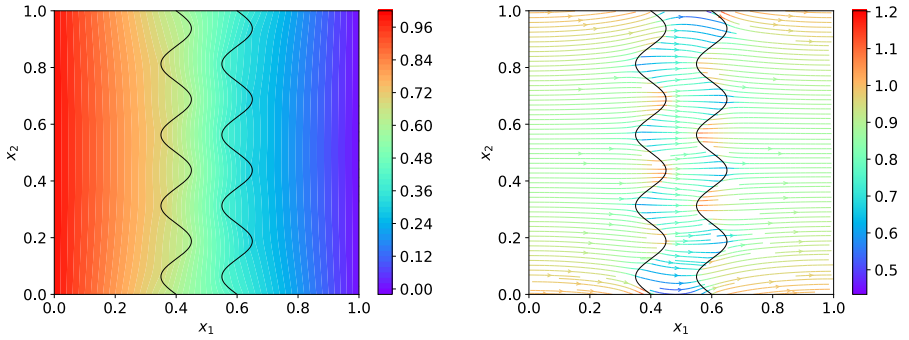

Figure 4.4: Full-dimensional numerical reference solution for the pressure p (left) and the velocity $-\mathbf{K}\nabla p$ (right) for the case of $d_0 = 10^{-1}$.

Figure 4.5 shows the DG solutions for the pressure p_Γ in the reduced models I, I-R, II, and II-R in comparison to the full-dimensional reference solution $p_\Gamma^{\mathrm{ref.}}$. On the

one hand, the effective pressure $p_\Gamma = p_\Gamma(x_2)$ is plotted for a fixed valued of $d_0 = 10^{-1}$, where one can see a clear difference between the solutions of the various reduced models. As expected, model I performs best, while model II-R performs worst. On the other hand, Figure 4.5 also displays the L^2-error $\left\| p_\Gamma - p_\Gamma^{\text{ref.}} \right\|_{L^2(\Gamma)}$ as function of the aperture parameter d_0, where, again, the solution of model I sticks out as the most accurate. In Figure 4.5, the L^2-errors of the reduced models I-R and II-R show a similar behavior. In particular, their convergence towards the reference solution $p_\Gamma^{\text{ref.}}$ for a decreasing aperture is considerably slower than the convergence for the models I and II. Thus, in this test problem, it is primarily the rectification of the bulk domains Ω_1 and Ω_2 that negatively affects the model error and rate of convergence with respect to a decreasing aperture. However, comparing the solutions of model I and model II, there is also an undeniable effect on the accuracy of the solution in connection with the inclusion of aperture gradients ∇d_1, ∇d_2 in Eq. (4.39b). For small apertures, the error of model I seems to stagnate. This is attributed to numerical errors in the computation of the full-dimensional reference solution $p_\Gamma^{\text{ref.}}$ and discussed in more detail in Section 4.6.2.

4.6.1.2 Three-Dimensional Test Problem

Next, we extend the test problem from Section 4.6.1.1 to the three-dimensional case. For this, we define the aperture functions d_1 and d_2 by

$$d_1(x_2, x_3) = d_0 + \frac{1}{2} d_0 \big(\sin(8\pi x_2) + \sin(8\pi x_3) \big),$$
$$d_2(x_2, x_3) = d_0 - \frac{1}{2} d_0 \big(\sin(8\pi x_2) + \sin(8\pi x_3) \big)$$

with a parameter $d_0 > 0$ so that the total aperture $d(x_2, x_3) = 2d_0$ is constant. The resulting geometry is illustrated in Figure 4.6. The permeability and boundary conditions are defined as in Section 4.6.1.1.

Figure 4.7 displays the numerical reference solution for the averaged pressure $p_\Gamma^{\text{ref.}}$ for $d_0 = 10^{-1}$. Besides, the DG solutions for the effective pressure p_Γ

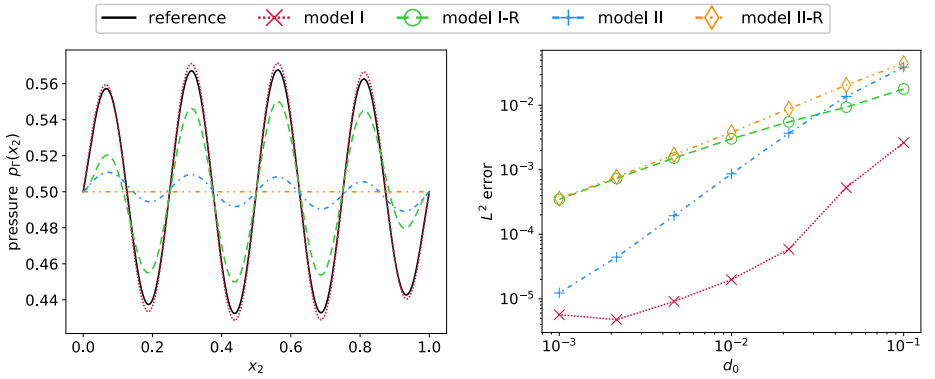

Figure 4.5: Numerical solutions for the effective pressure p_Γ for the reduced model (4.39) and its variants in comparison to the numerical reference solution $p_\Gamma^{\text{ref.}}$ for $d_0 = 10^{-1}$ (left) and L^2-error $\|p_\Gamma - p_\Gamma^{\text{ref.}}\|_{L^2(\Gamma)}$ as function of d_0 (right).

in the reduced model (4.39) and its variants are shown in Figure 4.8. Here, in comparison with the reference solution in Figure 4.7, a behavior analogous to the two-dimensional case in Figure 4.5 becomes apparent. The solution of model I matches well with the reference solution, whereas the solutions of the models I-R and II reproduce the sine-like pattern of the reference solution at a too low amplitude and the solution of model II-R is virtually constant. This is also reflected by the L^2-error $\left\|p_\Gamma - p_\Gamma^{\text{ref.}}\right\|_{L^2(\Gamma)}$, which is displayed in Figure 4.9 as function of the aperture parameter d_0. The L^2-error shows the same trends for a declining aperture as observed in the two-dimensional case.

4.6.2 Flow Perpendicular to an Axisymmetric Fracture

For this next test problem, we again consider a sinusoidal fracture in the two-dimensional domain $\Omega = (0, 1)^2$, however, this time with a non-constant total

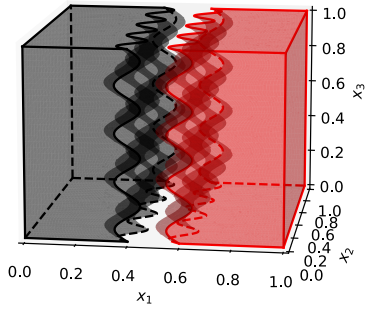

Figure 4.6: Bulk domains Ω_1 (black) and Ω_2 (red) for $d_0 = 10^{-1}$.

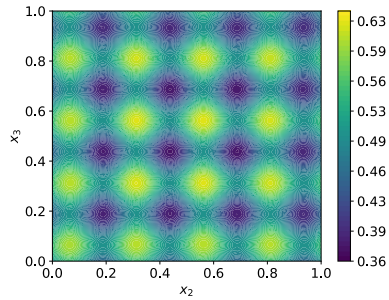

Figure 4.7: Numerical reference solution $p_\Gamma^{\text{ref.}}$ for $d_0 = 10^{-1}$.

aperture d. More particularly, the aperture functions d_1 and d_2 are defined by

$$d_1(x_2) = d_0 + \tfrac{1}{2} d_0 \sin(8\pi x_2), \qquad d_2(x_2) = d_0 + \tfrac{1}{2} d_0 \sin(8\pi x_2) \tag{4.54}$$

with a free parameter $d_0 > 0$. Thus, the interface Γ is the center line of an axisymmetric fracture and the total aperture d ranges between d_0 and $3d_0$. In addition, the permeability $\mathbf{K}_\mathrm{f}$ inside the fracture and the given pressure g at the external boundary $\partial\Omega$ are defined as in Section 4.6.1.1. The fracture geometry and full-dimensional solution from the DG scheme (4.48) are shown in Figure 4.10 for the case of $d_0 = 10^{-1}$.

A comparison between the numerical solution p_Γ of the different reduced models and the averaged full-dimensional reference solution $p_\Gamma^{\text{ref.}}$ inside the fracture can be found in Figure 4.11. Here, it occurs that the solutions of the models I and I-R and the solutions of the models II and II-R respectively show a very similar behavior. While the solutions of model II and II-R slowly display convergence towards the reference solution with declining aperture parameter d_0, there is already a remarkable agreement between the solutions of model I and I-R and the reference solution. As compared to the solutions of model II and II-R, the

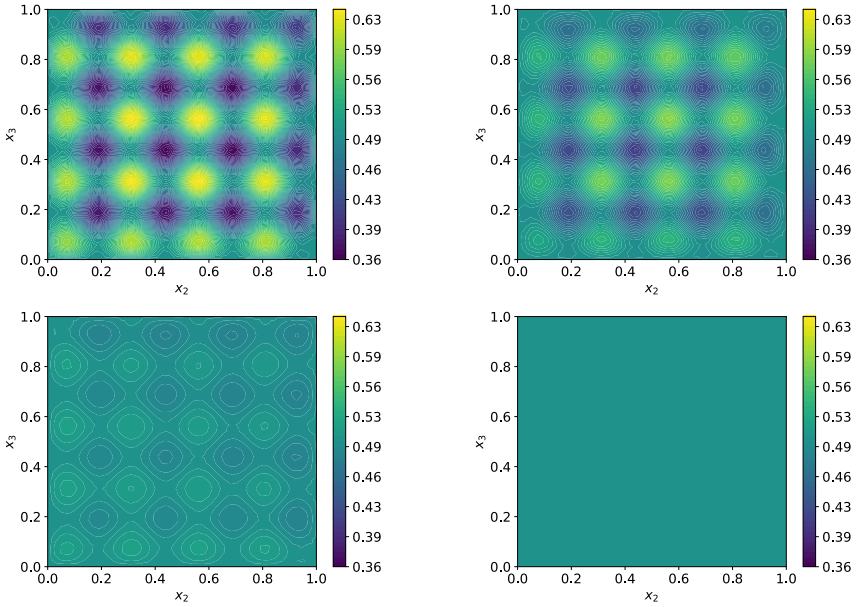

Figure 4.8: Numerical solutions for the effective pressure p_Γ inside the fracture for the reduced model (4.39) *and its variants for $d_0 = 10^{-1}$: model I (top left), model I-R (top right), model II (bottom left), and model II-R (bottom right).*

solutions of model I and I-R are more accurate by several orders of magnitude. Thus, in contrast to the test problem in Section 4.6.1.1, the artificial rectification of the bulk domains Ω_1 and Ω_2 is virtually without effect, while the inclusion of aperture gradients ∇d_1, ∇d_2 in Eq. (4.39b) seems all the more significant in order to obtain accurate solutions. This is probably due to the symmetry of the problem and cannot be expected in general.

Further, it is noticeable in Figure 4.11 that, for the models I and I-R, the L^2-error with respect to the numerical reference solution $p_\Gamma^{\text{ref.}}$ suffers a stop of convergence at small values of the aperture parameter d_0. Inspecting the numerical

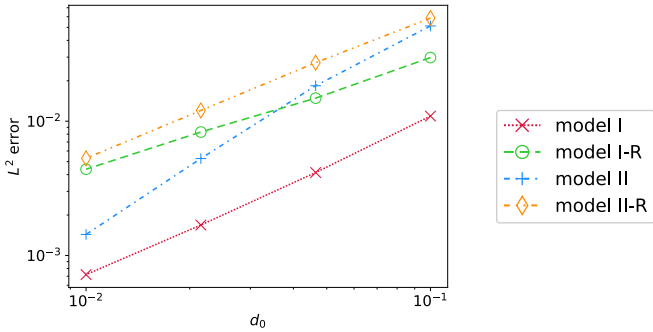

Figure 4.9: L^2-error $\|p_\Gamma - p_\Gamma^{\text{ref.}}\|_{L^2(\Gamma)}$ as function of d_0.

reference solution $p_\Gamma^{\text{ref.}}$ for small apertures, one observes an oscillatory behavior, which might be associated with the integration of the full-dimensional reference solution according to Eq. (4.12a). In particular, these spurious oscillations display amplitudes in the range of 10^{-5} to 10^{-6} and hence can fully explain the total L^2-error and stop of convergence in Figure 4.11. Furthermore, the symmetry of the test problem in this section suggests that the effective pressure inside

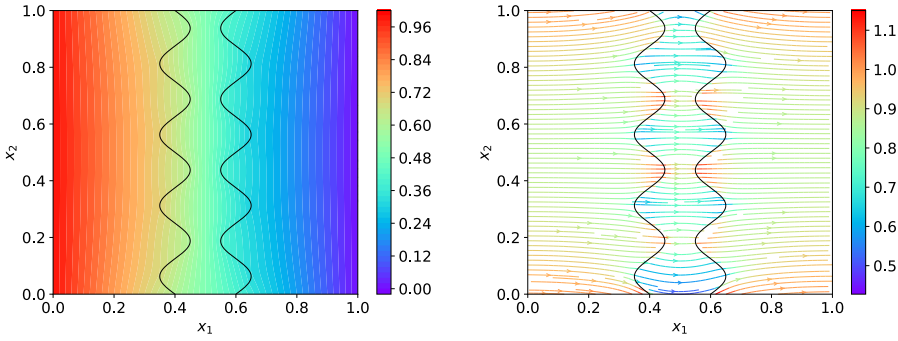

Figure 4.10: Full-dimensional numerical reference solution for the pressure p (left) and the velocity $-\mathbf{K}\nabla p$ (right) for the case of $d_0 = 10^{-1}$.

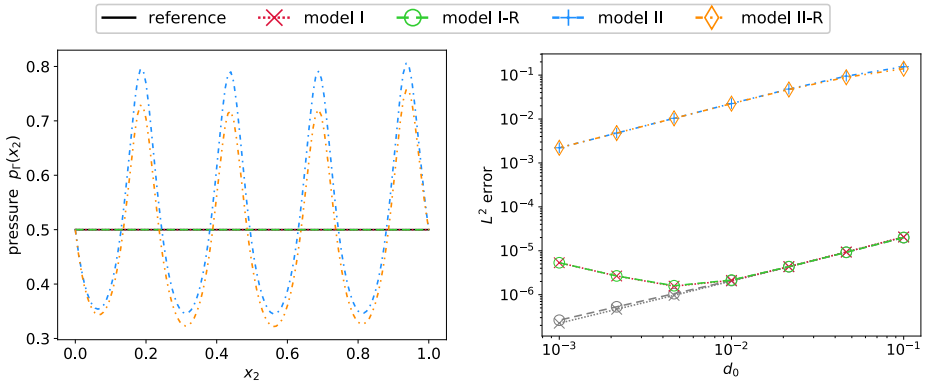

Figure 4.11: Numerical solutions for the effective pressure p_Γ for the reduced model (4.39) and its variants in comparison to the numerical reference solution $p_\Gamma^{\text{ref.}}$ for $d_0 = 10^{-1}$ (left) and L^2-error $\|p_\Gamma - p_\Gamma^{\text{ref.}}\|_{L^2(\Gamma)}$ as function of d_0 (right) with respect to the numerical reference solution $p_\Gamma^{\text{ref.}}$ (in color) and the presumably exact reference solution $p_\Gamma^{\text{ref.}} \equiv \frac{1}{2}$ (gray).

the fracture exactly equals $p_\Gamma^{\text{ref}} \equiv \frac{1}{2}$. Thus, we can consider the L^2-error with respect to this presumably exact solution, which is also shown in Figure 4.11. Remarkably, in this case, one observes unimpeded convergence with the decline of the aperture parameter d_0. This confirms that we are dealing with a numerical error in the computation of the reference solution and not with a systematic model error.

4.6.3 Tangential Flow through an Axisymmetric Fracture

In this test problem, we consider an axisymmetric sinusoidal fracture as in Section 4.6.2 with the aperture functions d_1 and d_2 defined by Eq. (4.54). We define the permeability inside the fracture by $\mathbf{K}_\mathrm{f} = 2\mathbf{I}$ for the full-dimensional model (4.2), which results in the effective permeabilities $\mathbf{K}_\Gamma = 2\mathbf{I}$ and $K_\Gamma^\perp = 2$ for the reduced model (4.39) and its variants. In particular, the fracture permeability

is larger than the bulk permeability. The pressure p at the boundary $\partial\Omega$ is given by the function $g(\mathbf{x}) = 4x_1(1-x_1)(1-x_2)$, what results in an inflow at bottom of the domain with the fracture as the preferential flow path. Figure 4.12 illustrates the fracture geometry and the resulting solution from the DG scheme (4.48) for $d_0 = 10^{-1}$.

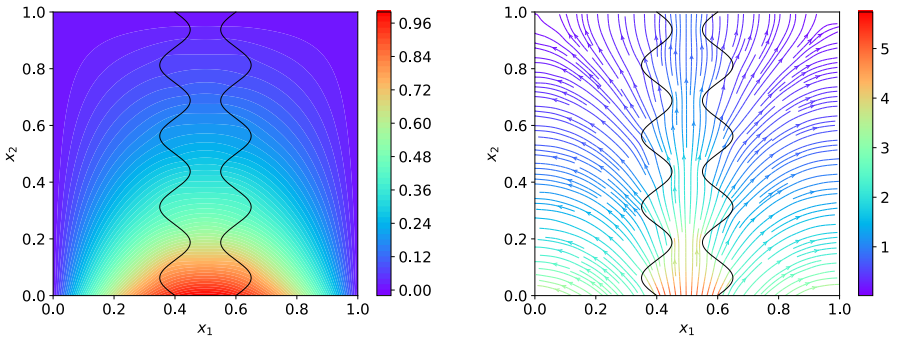

Figure 4.12: Full-dimensional numerical reference solution for the pressure p (left) and the velocity $-\mathbf{K}\nabla p$ (right) for the case of $d_0 = 10^{-1}$.

Figure 4.13 shows the DG solutions p_Γ of the different reduced models in comparison with the numerical reference solution $p_\Gamma^{\text{ref.}}$. In particular, it can be seen that the models II and II-R display a similar behavior and are the least accurate, while model I shows the best match with the reference solution. Further, in Figure 4.13, the L^2-error $\|p_\Gamma - p_\Gamma^{\text{ref.}}\|_{L^2(\Gamma)}$ displays a convergence with the decline of the aperture parameter d_0 for all variants of the reduced model (4.39), where the solution of model I converges faster than the solutions of the other models. However, for model I, the convergence stagnates at small apertures, which is associated with numerical errors in the computation of the reference solution $p_\Gamma^{\text{ref.}}$ as discussed in Section 4.6.2. Notably, for the test problem in this section, one finds by comparing the solution of model I with the solutions of model I-R and model II in Figure 4.13 that both the artificial rectification of the

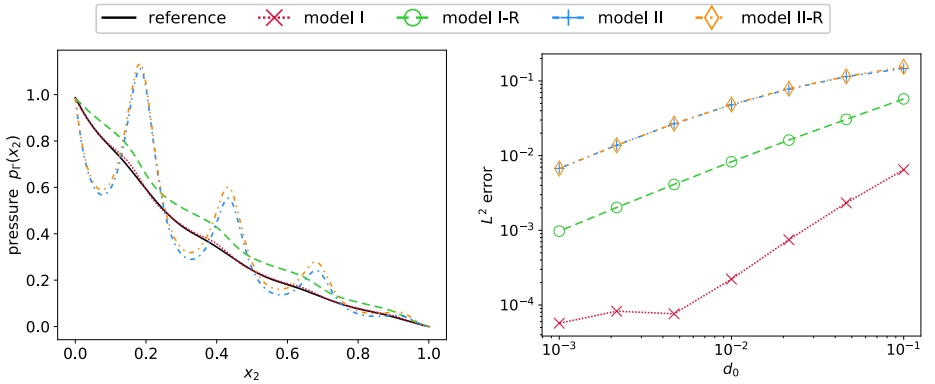

Figure 4.13: Numerical solutions for the effective pressure p_Γ for the reduced model (4.39) and its variants in comparison to the numerical reference solution $p_\Gamma^{\text{ref.}}$ for $d_0 = 10^{-1}$ (left) and L^2-error $\|p_\Gamma - p_\Gamma^{\text{ref.}}\|_{L^2(\Gamma)}$ as function of d_0 (right).

bulk domains Ω_1 and Ω_2 and the negligence of aperture gradients in Eq. (4.39b) significantly impair the accuracy of the solution.

We conclude that, for fractures with non-constant aperture, the solutions of our proposed model provide systematically better approximations to the reference solution as the solutions of previously proposed models. A discontinuous Galerkin discretization has been introduced that is able solve the mixed-dimensional model equations efficiently. In the next chapter, we will apply the presented ideas to the physically more complex model of linear poro-elastic media coupled with fracture propagation.

Fracture Propagation in Poro-elastic Media

5

The content of the following chapter led to the manuscript "Modeling fracture propagation in poro-elastic media combining phase-field and discrete fracture models" submitted to "Computer Methods in Applied Mechanics and Engineering" (under revision). All source code of the implementation is available in a public repository[1]. I conceived of the presented idea, developed the theory and performed the numerical computations.

This chapter describes an advanced application of Dune-MMesh, cf. Chapter 2, to the modeling of fracture propagation in poro-elastic media combining mixed-dimensional discrete fracture models and phase-field modeling.

5.1 Introduction

Modeling flow in dynamically fracturing porous media is of high interest for a wide range of natural and technical processes, in particular in the context of subsurface engineering applications. In all these processes, several physical effects mutually influence each other: variations of the fluid pressure lead to deformation of the porous matrix, which in turn induces variation of the fractures aperture. This, again, alters the fracture's conductivity, and strongly influences

[1] https://github.com/samuelburbulla/pfdfm

the pressure distribution within the fluid system. Thermal effects could also influence the physical properties of fluid and porous matrix. Moreover, when fracture propagation is taken into account, the change in pressure could also modify the fracture networks topology in an irreversible manner. The numerical modeling of flow in fractured porous media represents a serious challenge, not only because of these interfering effects, but also because of the extreme geometrical dimensions of fractures.

For the modeling of fracture propagation, phase-field models have been proposed that approximate sharp fractures by a diffuse indicator-like phase-field function. This variational approach, initially proposed for fractures in elastic material [6], has been applied to various flow models in porous media [48, 52, 53]. However, phase-field models, which are very flexible with regard to different fracture geometries and network topologies, are computationally rather expensive due to the grid resolution required. On the other hand, there are contributions employing sharp representations of the fractures that keep track of the fracture as a geometric discontinuity, e.g., [60, 61]. Numerically coupled approaches as the X-field [36] have been proposed in order to reduce the computational cost by combining sharp and diffuse interface approaches. In particular, in the cited work the authors consider brittle fracture in an elastic media and the phase-field solution is sought only in a portion of the domain around the fracture tip.

In this chapter, we extend the X-field idea to poro-elasticity and propose some adaptations. More precisely, we solve the phase-field equation in the whole domain, even if we actually use the phase-field solution only to describe the evolution of the fracture tips. This way, we overcome the issue in the X-field approach of finding the correct movement of the tips and setting the boundary conditions of the phase-field domain.

With this approach, we combine the desired properties of both phase-field models and discrete fracture models in one mathematical model. On the one hand, we always have an explicit geometrical representation of the fracture network, on the other hand, we retain the geometric flexibility of the phase field approach.

This work is structured as follows. In Section 5.2, we introduce the geometrical setting as well as the poro-elastic equations that provide the basis of our mixed-dimensional phase-field model. Then, in Section 5.3, following the ideas of discrete fracture modeling and phase-field approximation of fractures, we present our new hybrid model in equations (5.15)-(5.25), and we prove that it is thermodynamically consistent. In Section 5.4, we present the weak form of our discontinuous Galerkin discretization which directly incorporates discontinuities across fracture facets as we choose a fully conforming mesh. Finally, in Section 5.5, we present the results of two numerical experiments, and study some properties of our numerical scheme.

5.2 The Fracturing Process in Fluid-Filled Porous Media

In this section, we collect the assumptions and constitutive laws that govern the physical processes relevant for our work. These assumptions are the basis for the formulation of discrete and phase-field representations of fractures in Section 5.3.

5.2.1 The Fractured Domain

Let $\mathscr{D} \subset \mathbb{R}^n$ denote a two- or three-dimensional domain ($n = 2, 3$) partitioned into a poro-elastic domain $\mathscr{B} \subset \mathscr{D}$ and a fracture subset $\mathscr{C} \subset \mathscr{D}$, as depicted in Figure 5.1 (left). We assume that the width of the fracture domain $\mathscr{C}$ is significantly smaller than its longitudinal size. In this case, it is reasonable to approximate the fracture by a one-codimensional regular manifold immersed in $\mathscr{D}$. Precisely, let us assume that we can represent the full-dimensional fracture $\mathscr{C}$ by the one-codimensional manifold $\Gamma \subset \mathscr{C}$ and an aperture function $d : \Gamma \times (0, T) \to d(\mathbf{x}, t) \in (0, \infty)$, as depicted in Figure 5.1 (right).

Note that we will derive a reduced equation on Γ that is supposed to capture the full-dimensional flow effects in $\mathscr{C}$. Furthermore, from the displacement $\mathbf{u} : \Omega \times (0,T) \to \mathbb{R}^n$ of the poro-elastic domain Ω, we will define the time-dependent aperture function by the normal displacement jump, cf. (5.10) below. Note that in the reduced setting the poro-elastic domain is $\Omega = \mathscr{D} \setminus \Gamma$, deformed by the displacement $\mathbf{u}$, which can be now discontinuous across Γ.

Indeed, we assume that Γ is orientable so we can identify the two sides, γ^+ and γ^-, with outer normal vector $\mathbf{n}^+$ and $\mathbf{n}^-$, respectively. Correspondingly, the value of the traces of $\mathbf{u}$ are indicated as $\mathbf{u}^+$ and $\mathbf{u}^-$. Further, we will denote the two-sided inner boundary of Ω by $\gamma := \gamma^+ \cup \gamma^-$.

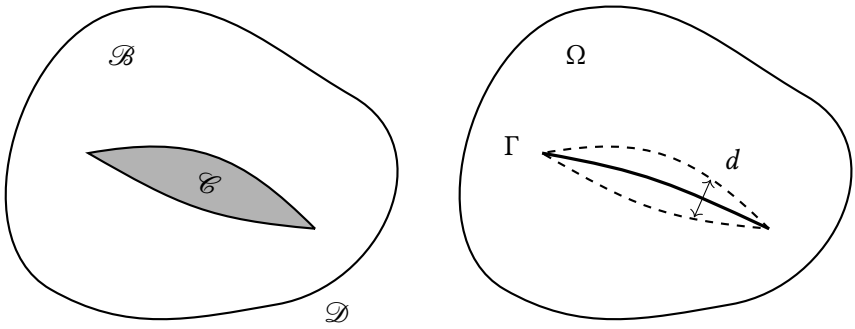

Figure 5.1: The domain $\mathscr{D}$ is partitioned into a poro-elastic domain $\mathscr{B}$ and a fracture domain $\mathscr{C}$. The fracture domain will be represented by one-codimensional manifold Γ and corresponding aperture function d.

We use Biot's model, cf. Section 1.3.3, describing poro-elastic behavior in the bulk domain $\mathscr{B}$.

5.2.2 Fracture Pressure

Within the equi-dimensional fracture domain $\mathscr{C}$, we assume that the fluid motion is described by the following continuity equation for single-phase flow in porous media, cf. [53].

The pressure $p_F : \mathscr{C} \times (0,T) \to \mathbb{R}$ satisfies

$$\left(\frac{p_F}{M}\right)_t - \operatorname{div}\left(\frac{\mathbf{K}_F}{\eta}\nabla p_F\right) = q, \tag{5.1}$$

where $\mathbf{K}_F \in \mathbb{R}^{n\times n}$ $[m^2]$ is the permeability within the fracture.

We assume that the permeability within the fracture can be split into the normal component K_n^f and the tangential tensor K_τ^f. Then, we apply lubrication theory to formulate K_τ^f as a function of the aperture d of the fracture. Under the assumption of plane Poiseuille flow we have

$$K_\tau^f = \frac{d^2}{12}\mathbf{I}$$

as tangential permeability (in all directions) [53]. For the normal permeability component, we choose the normal contribution of the bulk permeability

$$K_n^f = \mathbf{n}^\top \mathbf{K}\mathbf{n}.$$

The pressure within the fracture has to be coupled to the pressure in the porous matrix. For this purpose, we impose pressure continuity, normal stress equilibrium and continuity of normal fluid velocity across the fracture-bulk interface, as described by the subsequent coupling conditions.

At the interface $\partial\mathscr{C} = \partial\mathscr{B} \setminus \partial\mathscr{D}$ between $\mathscr{B}$ and $\mathscr{C}$ we impose

$$p = p_F, \tag{5.2}$$
$$(\sigma(\mathbf{u}) - \alpha p\mathbf{I})\mathbf{n} = -p_F\mathbf{n}, \tag{5.3}$$
$$\mathbf{K}\nabla p \cdot \mathbf{n} = \mathbf{K}_F\nabla p_F \cdot \mathbf{n}, \tag{5.4}$$

with $\mathbf{n}$ denoting the outer normal to $\partial\mathscr{C}$. It remains to formulate boundary and initial conditions for Equations (1.5) and (5.1).

5.2.3 Boundary and Initial Conditions

We impose zero displacement and no-flow conditions at the boundary of $\mathscr{D}$, and set an initial null value for all unknowns, i.e.,

$$\mathbf{u} = 0,\ \nabla p \cdot \mathbf{n} = 0, \qquad \text{on } \partial\mathscr{D} \times (0, T), \tag{5.5}$$
$$p(\cdot, 0) = 0,\ \mathbf{u}(\cdot, 0) = 0, \qquad \text{in } \Omega \times (0, T), \tag{5.6}$$
$$p_F(\cdot, 0) = 0, \qquad \text{in } \mathscr{C} \times (0, T). \tag{5.7}$$

Finally, we have to clarify what we consider as driving force for fracture propagation. For this purpose, we use the criterion of Griffith [38].

5.2.4 Griffith's Criterion and Stress Splitting

Griffith's criterion of fracture mechanics states that in a physical point $x \in \mathscr{D}$ a fracture is created when the elastic energy restitution rate associated to this point exceeds Griffith's critical energy $g_c : \mathscr{D} \to \mathbb{R}$ [$\mathrm{J\,m^{-1}}$], cf. [38]. As propagation of fractures is essentially driven by tensile forces in the poro-elastic medium, we additively decompose the stress tensor

$$\sigma(\mathbf{u}) = \sigma^+(\mathbf{u}) + \sigma^-(\mathbf{u}) \tag{5.8}$$

into a tensile part $\sigma^+(\mathbf{u})$ and a compressive part $\sigma^-(\mathbf{u})$. We use a splitting introduced in [7] where the trace of the stain tensor $\operatorname{tr}(\epsilon(\mathbf{u})) = \operatorname{div}(\mathbf{u})$ is split into positive and negative parts

$$\operatorname{div}^+(\mathbf{u}) = \max(\operatorname{div}(\mathbf{u}), 0), \qquad \operatorname{div}^-(\mathbf{u}) = \min(\operatorname{div}(\mathbf{u}), 0).$$

Consequently, the effective stress tensor is split into

$$\begin{aligned}\sigma^+(\mathbf{u}) &:= K \operatorname{div}^+(\mathbf{u})\mathbf{I} - \frac{2\mu}{n} \operatorname{div}(\mathbf{u})\mathbf{I} + 2\mu\epsilon(\mathbf{u}),\\ \sigma^-(\mathbf{u}) &:= K \operatorname{div}^-(\mathbf{u})\mathbf{I},\end{aligned}$$

where $K = \frac{2\mu}{n} + \lambda$ is the bulk modulus.

On the basis of this stress tensor decomposition, we formulate the elastic energy that is responsible for driving fracture propagation, namely

$$\Psi^+(\mathbf{u}) := \frac{1}{2}\sigma^+(\mathbf{u}) : \epsilon(\mathbf{u}).$$

Following the variational approach of [17], we define the elastic energy associated to the fracture by

$$W_G(\mathbf{u}, \Gamma) := \int_\Omega \Psi^+(\mathbf{u})\, dx + \int_\Gamma g_c\, ds. \tag{5.9}$$

We emphasize that Ω, and therefore $\mathbf{u}$, are dependent on Γ. Finally, the basic principle of the variational approach to fracture is to minimize W_G. This principle will be used in Section 5.3.3 where we approximate Γ using a diffuse phase-field approximation.

5.3 Derivation of the Mixed-Dimensional Phase-Field Model

We proceed with the derivation of our mixed-dimensional phase-field model. This model consists of partial differential equations defined on domains with different dimensions, in our case, Ω and Γ with dimensions d and $d-1$, that form a coupled system. The physical assumptions stated in this section will serve as basis for the mathematical model. For modeling purposes, we divide the fracture into two parts:

1. An initially given fracture manifold Γ^0 with corresponding mixed-dimensional flow model.
2. A propagating part Γ^* that is approximated by a diffuse phase-field representation.

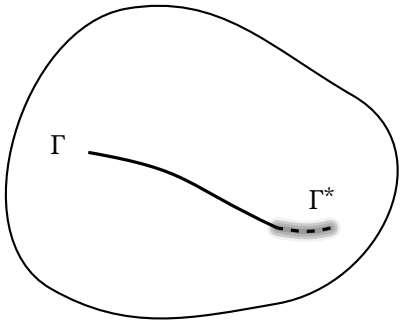

Figure 5.2: We divide fractures into initially given manifold Γ^0 and propagating part Γ^*.

The division is schematically depicted in Figure 5.2. Note that this section is structured as follows. We start with the definition of the fracture aperture induced by the displacement. Then, in Section 5.3.2, based on the full-dimensional equation (5.1), we derive a reduced model equation on Γ^0 with appropriate

coupling conditions between fracture and porous matrix. Afterwards, in Section 5.3.3, we formulate the propagation of the fracture in the diffuse phase-field framework. Finally, in Section 5.3.4, we summarize all equations of our mixed-dimensional phase-field model.

5.3.1 The Fracture Aperture

The displacement of the porous matrix can be used to determine the magnitude of the fracture aperture $d = d(\mathbf{u})$ as a function of the normal displacement of the porous matrix on both sides of the fracture Γ^0. We define the aperture as

$$d(\mathbf{u}) \coloneqq \max(-[\![\mathbf{u} \cdot \mathbf{n}]\!], 0) + d_0, \tag{5.10}$$

where the jump operator $[\![\cdot]\!]$ is given by

$$[\![\psi]\!] \coloneqq \psi|_{\gamma^+} - \psi|_{\gamma^-}, \qquad [\![\mathbf{u} \cdot \mathbf{n}]\!] \coloneqq \mathbf{u}|_{\gamma^+} \cdot \mathbf{n}^+ + \mathbf{u}|_{\gamma^-} \cdot \mathbf{n}^-. \tag{5.11}$$

The residual aperture $d_0 > 0$ ensures the well-posedness of the reduced equation (5.18) below. It can also be physically motivated, for instance, considering surface roughness. Note that we restrict the aperture in (5.10) to the positive part as we will not incorporate contact mechanics constraints.

5.3.2 The Reduced Model

A widely used approach to model fractured porous media, and in particular flow, is to reduce the dimension of the fracture domain to a one-codimensional manifold. The main advantage is the lower computational complexity since it is not necessary to resolve the aperture with the grid. We derive a reduced model on Γ^0 by integrating equation (5.1) along orthogonal line segments

$$L(\mathbf{s}) = \left\{ \mathbf{s} + t\mathbf{n} \;\middle|\; t \in \left(-\frac{d}{2}, \frac{d}{2} \right) \right\}$$

for all $\mathbf{s} \in \Gamma^0$. This idea was initially proposed in [51] and leads to a partial differential equation on Γ^0 formulated in terms of the mean pressure

$$p_\Gamma(\mathbf{s}) := \frac{1}{d}\int_{L(\mathbf{s})} p_F \, dx.$$

Following the derivation as in Chapter 3, using equation (5.1) and the coupling conditions (5.2) and (5.4), we find the reduced model equation on Γ^0 given by

$$d(\mathbf{u})\left(\frac{p_\Gamma}{M}\right)_t - \operatorname{div}\left(d(\mathbf{u})\frac{K_\tau^f}{\eta}\nabla p_\Gamma\right) + [\![\frac{\mathbf{K}}{\eta}\nabla p \cdot \mathbf{n}]\!] = d(\mathbf{u})q,$$

with the coupling condition

$$-\frac{\mathbf{K}}{\eta}\nabla p \cdot \mathbf{n} = -2\frac{K_n^f}{\eta}\frac{p_\Gamma - p}{d(\mathbf{u})} =: C(p, p_\Gamma, \mathbf{u}). \tag{5.12}$$

On the internal boundary γ between Γ^0 and Ω, equation (5.12) realizes a linear relation between the pressure jump and the normal flux. Other choices could be made, as explained in [51].

The next step of the derivation is the description of fracture propagation by a phase-field representation.

5.3.3 Phase-Field Representation

Many approaches to the modeling of fracture propagation represent sharp fractures by diffuse phase-field functions. The general concept behind this idea is briefly described in the following for readers' convenience.

The Ambrosio–Tortorelli functional [6] given by

$$\gamma_l(\varphi) := \frac{1}{2l}(1-\varphi)^2 + \frac{l}{2}|\nabla\varphi|^2, \qquad (l > 0)$$

can be used to approximate the sharp line Γ^* by a diffuse representation $\varphi : \Omega \to [0,1]$. For a sequence of minimizers $\{\varphi_l\}_{l>0}$, i.e.,

$$\varphi_l = \arg\min_{\varphi \in V} \int_\Omega \gamma_l(\varphi)\, dx,$$

where $V = \{\varphi \in H^1(\Omega) \mid \varphi|_{\Gamma^*} = 0\}$, we have the property

$$\int_\Omega \gamma_l(\varphi)\, dx \to |\Gamma^*|, \tag{5.13}$$

for $l \to 0$ in the sense of Γ-convergence [6]. The function φ_l is a smooth function such that $\varphi_l = 1$ indicates the porous matrix Ω and $\varphi_l = 0$ indicates Γ^*, while the phase-field parameter $l > 0$ governs the width of the smooth transition zone, cf. [52].

In order to account for reduced resistance of fractured material, we introduce a convex degradation function $A(\varphi)$ that satisfies $A(0) = k$, $A(1) = 1$, and $A'(1) > 0$, in our case

$$A(\varphi) := (1-k)\varphi^2 + k.$$

Here, the number $k \ll 1$ is some residual resistance to ensure well-posedness of our model. Now, switching from a sharp to a diffuse representation of Γ^* and using (5.13), we reformulate the energy $W_G(\Gamma)$, previously defined in (5.9), in terms of the phase-field variable

$$W_\varphi(\mathbf{u}, \varphi) := \int_\Omega A(\varphi)\Psi^+(\mathbf{u}) + g_c\gamma_l(\varphi)\, dx + \int_{\Gamma^0} g_c\, dx.$$

As we also incorporate poro-elastic effects, we extend the energy to the free energy of the mixed-dimensional poro-elastic medium. For this purpose, we introduce a degraded effective stress tensor $\tilde{\sigma}(\mathbf{u}, \varphi)$ based on stress splitting (5.8)

by

$$\tilde{\sigma}(\mathbf{u}, \varphi) := A(\varphi)\sigma^{+}(\mathbf{u}) + \sigma^{-}(\mathbf{u}),$$

where only the tensile part is degraded with $A(\varphi)$. Then, we introduce the free energy functional

$$\begin{aligned} W(\mathbf{u}, p, \varphi, p_\Gamma) &:= W_\varphi(\mathbf{u}, \varphi) + \int_\Omega \frac{1}{2}\sigma^{-}(\mathbf{u}) : \epsilon(\mathbf{u}) + \frac{p^2}{2M}\, dx \\ &\quad + \int_{\Gamma^0} d(\mathbf{u})\frac{p_\Gamma^2}{2M}\, dx \\ &= \int_\Omega \frac{1}{2}\tilde{\sigma}(\mathbf{u}, \varphi) : \epsilon(\mathbf{u}) + \frac{p^2}{2M} + g_c\gamma_l(\varphi)\, dx \\ &\quad + \int_{\Gamma^0} d(\mathbf{u})\frac{p_\Gamma^2}{2M} + g_c\, dx. \end{aligned} \tag{5.14}$$

The energy functional (5.14) is the base for the system of partial differential equations below.

In the next section, we summarize all equations of our mixed-dimensional phase-field model, and we will prove that our model is thermodynamically consistent.

5.3.4 The Mixed-Dimensional Phase-Field Model

Our mixed-dimensional phase-field model consists in the following system of partial differential equations. For a given $l > 0$, find the displacement $\mathbf{u} : \Omega \times (0,T) \to \mathbb{R}^n$, the phase-field $\varphi : \Omega \times (0,T) \to [0,1]$, the pressure $p : \Omega \times (0,T) \to \mathbb{R}$ and the fracture pressure $p_\Gamma : \Gamma^0 \times (0,T) \to \mathbb{R}$ satisfying

$$-\operatorname{div}(\tilde{\sigma}(\mathbf{u},\varphi) - \alpha p \mathbf{I}) = 0, \qquad \text{in } \Omega \times (0,T), \tag{5.15}$$

$$-\frac{g_c}{l}(1-\varphi) - g_c l \Delta\varphi + A'(\varphi)\Psi^+(\mathbf{u}) = 0, \qquad \text{in } \Omega \times (0,T), \tag{5.16}$$

$$\left(\frac{p}{M} + \alpha \operatorname{div}(\mathbf{u})\right)_t - \operatorname{div}\left(\frac{\mathbf{K}}{\eta}\nabla p\right) = q, \qquad \text{in } \Omega \times (0,T), \tag{5.17}$$

$$d(\mathbf{u})\left(\frac{p_\Gamma}{M}\right)_t - \operatorname{div}\left(d(\mathbf{u})\frac{K_\tau^f}{\eta}\nabla p_\Gamma\right) + d(\mathbf{u})_t + [\![\frac{\mathbf{K}}{\eta}\nabla p \cdot \mathbf{n}]\!] = d(\mathbf{u})q, \qquad \text{in } \Gamma^0 \times (0,T), \tag{5.18}$$

with boundary and initial conditions

$$\mathbf{u} = 0, \quad \nabla\varphi \cdot \mathbf{n} = 0, \quad \nabla p \cdot \mathbf{n} = 0, \qquad \text{on } \partial\mathscr{D} \times (0,T), \tag{5.19}$$

$$\nabla p_\Gamma \cdot \mathbf{n}_\Gamma = 0, \qquad \text{on } \partial\Gamma^0 \times (0,T), \tag{5.20}$$

$$\nabla\varphi \cdot \mathbf{n} = 0, \qquad \text{on } \gamma \times (0,T), \tag{5.21}$$

$$-\frac{\mathbf{K}}{\eta}\nabla p \cdot \mathbf{n} = C(p, p_\Gamma, \mathbf{u}), \qquad \text{on } \gamma \times (0,T), \tag{5.22}$$

$$(\tilde{\sigma}(\mathbf{u},\varphi) - \alpha p \mathbf{I})\mathbf{n} = -\left(p_\Gamma - \frac{p_\Gamma^2}{2M}\right)\mathbf{n}, \qquad \text{on } \gamma \times (0,T), \tag{5.23}$$

$$\mathbf{u}(\cdot,0) = 0, \quad p(\cdot,0) = 0, \qquad \text{in } \Omega, \tag{5.24}$$

$$p_\Gamma(\cdot,0) = 0, \qquad \text{in } \Gamma^0, \tag{5.25}$$

where (5.19) and (5.24)-(5.25) incorporate the initial conditions (5.5) from Section 5.2.3. Note that (5.22)-(5.23) implicitly represent two conditions since γ denotes

the two-sided inner boundary of Ω. The normal $\mathbf{n}_\Gamma$ denotes the outer normal on the boundary of Γ^0.

In our opinion, this mixed-dimensional form has a more straight-forward character than the equivalent phase-field description of the flow problem, cf., for instance, [53]. The model is clearly separated into a bulk flow problem, a flow equation within the lower-dimensional fracture, and coupling conditions between those two domains.

5.3.5 Weak Formulation of the Model

Let us state the weak formulation of model (5.15)-(5.25). This form is useful for the proof of the thermodynamical consistency, and will be the basis of the discretization scheme.

As admissible functional spaces for displacement, phase-field and the pressures, we choose

$$\begin{aligned}
&\Phi^u := \left\{ \mathbf{v} \in \left[H^1(\Omega)\right]^n \mid \mathbf{v}|_{\partial\mathscr{D}} = 0 \right\}, \\
&\Phi^\varphi = H^1(\Omega), \quad \Phi^p = H^1(\Omega), \quad \Phi^{p_\Gamma} = H^1(\Gamma^0),
\end{aligned}$$

where the displacement has imposed Dirichlet values on the outer boundary of Ω only. Incorporating boundary conditions (5.5)-(5.7), the model (5.15)-(5.25) in its weak form reads as follows.

For a given $l > 0$ and at each time $t \in (0, T)$, find $\mathbf{u} = \mathbf{u}(t) \in \Phi^u$, $\varphi = \varphi(t) \in \Phi^\varphi$, $p = p(t) \in \Phi^p$ and $p_\Gamma = p_\Gamma(t) \in \Phi^{p_\Gamma}$ such that

$$\int_\Omega (\tilde{\sigma}(\mathbf{u}, \varphi) - \alpha p \mathbf{I}) : \epsilon(\mathbf{v})\, dx + \int_\gamma \left(p_\Gamma - \frac{p_\Gamma^2}{2M} \right) \mathbf{n} \cdot \mathbf{v}\, ds = 0, \tag{5.26}$$

$$\int_\Omega -\frac{g_c}{l}(1-\varphi)\phi + g_c l \nabla\varphi \cdot \nabla\phi + A'(\varphi)\Psi^+(\mathbf{u})\phi\, dx = 0, \tag{5.27}$$

$$\int_\Omega \left(\frac{p}{M} + \alpha \operatorname{div}(\mathbf{u}) \right)_t \psi + \left(\frac{\mathbf{K}}{\eta} \nabla p \right) \cdot \nabla\psi\, dx + \int_\gamma C(p, p_\Gamma, \mathbf{u})\psi\, ds = \int_\Omega q\psi\, dx, \tag{5.28}$$

$$\int_{\Gamma^0} d(\mathbf{u}) \left(\frac{p_\Gamma}{M} \right)_t \psi_\Gamma + \left(d(\mathbf{u}) \frac{K_\tau^f}{\eta} \nabla p_\Gamma \right) \cdot \nabla\psi_\Gamma + d(\mathbf{u})_t \psi_\Gamma\, dx - \int_\gamma C(p, p_\Gamma, \mathbf{u})\psi_\Gamma\, ds = \int_{\Gamma^0} d(\mathbf{u}) q \psi_\Gamma\, dx, \tag{5.29}$$

for all $\mathbf{v} \in \Phi^u$, $\phi \in \Phi^\varphi$, $\psi \in \Phi^p$, $\psi_\Gamma \in \Phi^{p_\Gamma}$, and initial conditions (5.24)-(5.25) for $\mathbf{u}$, p and p_Γ. Note that, in the formulation above, we used the notation

$$\int_{\Gamma^0} [\![\mathbf{v} \cdot \mathbf{n}]\!]\, dx = \int_\gamma \mathbf{v} \cdot \mathbf{n}\, ds, \qquad (\mathbf{v} : \Omega \to \mathbb{R}^n)$$

which relates jumps on the interface Γ^0 to inner boundary integrals at γ.

In the next step, we prove that our model (5.15)-(5.25) is thermodynamically consistent.

5.3.6 Thermodynamical Consistency

Any physically meaningful model should be thermodynamically consistent, in the sense that for any solution of the model an appropriate total energy is non-

increasing over time or, in the presence of forcing term, grows in a controlled way as explained later. For our mixed-dimensional phase-field model, we prove this property in the following theorem.

Theorem 5.1 (Thermodynamical consistency)**:** *The model* (5.15)-(5.25)*, is thermodynamically consistent with respect to the free energy* (5.14) *if* $d(\mathbf{u}) > d_0$*. That is, the solution of* (5.26)-(5.29) *fulfills*

$$\frac{d}{dt}W(\mathbf{u}, p, \varphi, p_\Gamma) \leq \int_\Omega pq \, dx + \int_{\Gamma^0} d(\mathbf{u}) p_\Gamma q \, dx. \tag{5.30}$$

Proof. In the following we will indicate with $\partial_{\mathbf{u}} W(\mathbf{u}, p, \varphi, p_\Gamma)[\mathbf{v}]$ the Gateaux (functional) derivative of W with respect to $\mathbf{u}$ applied to a suitable test function $\mathbf{v}$,

$$\partial_{\mathbf{u}} W(\mathbf{u}, p, \varphi, p_\Gamma)[\mathbf{v}] = \lim_{h \to 0^+} \frac{W(\mathbf{u} + h\mathbf{v}, p, \varphi, p_\Gamma) - W(\mathbf{u}, p, \varphi, p_\Gamma)}{h},$$

and analogously for the other components. We have

$$\begin{aligned}\frac{d}{dt}W(\mathbf{u}, p, \varphi, p_\Gamma) = \partial_{\mathbf{u}} W(\mathbf{u}, p, \varphi, p_\Gamma)[\mathbf{u}_t] + \partial_p W(\mathbf{u}, p, \varphi, p_\Gamma)[p_t] \\ + \partial_\varphi W(\mathbf{u}, p, \varphi, p_\Gamma)[\varphi_t] + \partial_{p_\Gamma} W(\mathbf{u}, p, \varphi, p_\Gamma)[p_{\Gamma,t}].\end{aligned}$$

Since, using the given boundary conditions,

$$\begin{aligned}\partial_{\mathbf{u}} W(\mathbf{u}, p, \varphi, p_\Gamma)[\mathbf{u}_t] &= \int_\Omega \tilde{\sigma}(\mathbf{u}, \varphi) : \epsilon(\mathbf{u}_t) \, dx + \int_{\Gamma^0} [\![\mathbf{u}_t \cdot \mathbf{n}]\!] \frac{p_\Gamma^2}{2M} \, dx, \\ \partial_p W(\mathbf{u}, p, \varphi, p_\Gamma)[p_t] &= \int_\Omega \left(\frac{p}{M}\right) p_t \, dx, \\ \partial_\varphi W(\mathbf{u}, p, \varphi, p_\Gamma)[\varphi_t] &= \int_\Omega -\frac{g_c}{l}(1-\varphi)\varphi_t + g_c l \nabla\varphi \cdot \nabla\varphi_t \\ &\qquad + A'(\varphi)\Psi^+(\mathbf{u})\varphi_t \, dx,\end{aligned}$$

$$\partial_{p_\Gamma} W(\mathbf{u}, p, \varphi, p_\Gamma)[p_{\Gamma,t}] = \int_{\Gamma^0} d(\mathbf{u})\Big(\frac{p_\Gamma}{M}\Big) p_{\Gamma,t}\, dx,$$

we obtain, using (5.26)-(5.29),

$$\begin{aligned}
&\frac{d}{dt} W(\mathbf{u}, p, \varphi, p_\Gamma) \\
&\quad = \int_\Omega (\alpha p \mathbf{I}) : \epsilon(\mathbf{u}_t)\, dx - \int_\gamma \left(p_\Gamma - \frac{p_\Gamma^2}{2M}\right)\mathbf{n}\cdot\mathbf{u}_t\, ds + \int_{\Gamma^0} [\![\mathbf{u}_t\cdot\mathbf{n}]\!] \frac{p_\Gamma^2}{2M}\, dx \\
&\qquad - \int_\Omega \alpha \operatorname{div}(\mathbf{u}_t) p + \left(\frac{\mathbf{K}}{\eta}\nabla p\right)\cdot\nabla p\, dx - \int_\gamma C(p, p_\Gamma, \mathbf{u}) p\, ds \\
&\qquad - \int_{\Gamma^0} \left(d(\mathbf{u})\frac{K_\tau^f}{\eta}\nabla p_\Gamma\right)\cdot\nabla p_\Gamma + d(\mathbf{u})_t p_\Gamma\, dx + \int_\gamma C(p, p_\Gamma, \mathbf{u}) p_\Gamma\, ds \\
&\qquad + \int_\Omega pq\, dx + \int_{\Gamma^0} d(\mathbf{u}) p_\Gamma q\, dx \\
&\quad \le -\int_{\Gamma^0} \left(p_\Gamma - \frac{p_\Gamma^2}{2M}\right)[\![\mathbf{u}_t\cdot\mathbf{n}]\!]\, dx - \int_{\Gamma^0} [\![\mathbf{u}_t\cdot\mathbf{n}]\!]\left(p_\Gamma - \frac{p_\Gamma^2}{2M}\right) dx \\
&\qquad - \int_\gamma C(p, p_\Gamma, \mathbf{u})(p - p_\Gamma)\, ds + \int_\Omega pq\, dx + \int_{\Gamma^0} d(\mathbf{u}) p_\Gamma q\, dx \\
&\quad \le \int_\Omega pq\, dx + \int_{\Gamma^0} d(\mathbf{u}) p_\Gamma q\, dx.
\end{aligned}$$

Note that we used the property

$$-C(p, p_\Gamma, \mathbf{u})(p - p_\Gamma) = \frac{2K_n^f}{\eta d(\mathbf{u})}(p_\Gamma - p)(p - p_\Gamma) \le 0.$$

This proves the statement of (5.30). □

5.3.7 Towards Propagating Sharp Fracture

Up to this point, we assumed that Γ^0 is fixed in time, and the propagating part of the fracture Γ^* is only approximated by a diffuse phase-field representation. However, ultimately, one would like to consider a propagating sharp fracture $\Gamma^0 = \Gamma^0(t)$ whose geometry follows the diffuse approximation. This would also allow to update the lower-dimensional domain and equip the propagated part of the fracture with the desired mixed-dimensional flow model. In mathematical terms, this means that

$$\Gamma^0(t) = \Gamma^0(0) \cup \Gamma^*(t),$$

where $\Gamma^*(t)$ is the sharp interface limit of the phase-field representation φ. This evolution of the fracture geometry is not analyzed in a rigorous way at the continuous level in this work. In the numerical approximation section we describe its treatment in a discrete in time framework.

5.4 Mixed-Dimensional Discontinuous Galerkin Discretization

In this section, we present our discontinuous Galerkin (dG) discretization of model (5.26)-(5.29). The choice of discontinuous Galerkin discretizations is motivated by the fact that they can directly represent discontinuities across the fracture interface in the solution function spaces. Hereby, our approach will consider a subset of the grid facets as representation of the lower-dimensional fracture. In other words, we consider an approximation based on conforming grids.

5.4.1 Notation

Before we start with the description of the scheme, let us clarify some notation. Let $\mathcal{T}$ be a conforming triangulation of Ω, $\mathcal{F}$ the set of inner facets, and $\mathcal{F}_D$ the Dirichlet boundary facets. The triangulation $\mathcal{T}$ is assumed to be conforming to the fracture Γ^0, i.e., there is a subset $\mathcal{F}_\Gamma \subset \mathcal{F}$ of facets that can be interpreted as a triangulation $\mathcal{T}_\Gamma$ of Γ^0, cf. Figure 5.3 and Chapter 2. In order to distinguish, we denote the $(d-2)$-dimensional facets of the surface triangulation $\mathcal{T}_\Gamma$ by $\mathcal{F}^\Gamma$.

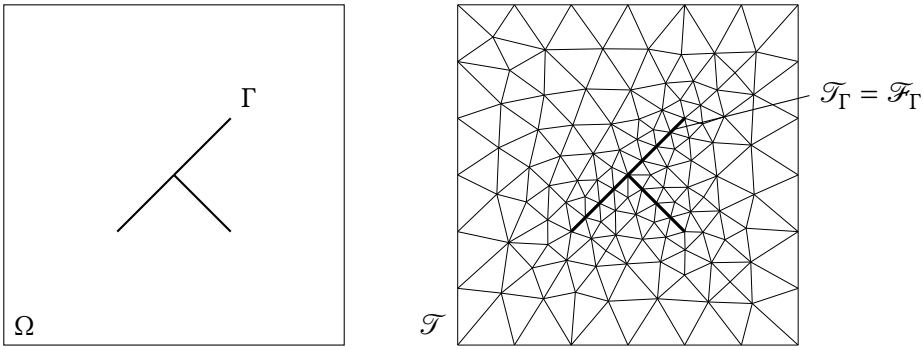

Figure 5.3: A subset of grid facets $\mathcal{F}_\Gamma$ of the bulk triangulation $\mathcal{T}$ coincides with the triangulation $\mathcal{T}_\Gamma$ of the lower-dimensional fracture Γ^0.

We define the finite-dimensional functional spaces of displacement, phase-field variable and the pressures by

$$\begin{aligned}
\Phi_h^u &:= \left\{ \mathbf{v}_h \in \left[L^2(\Omega)\right]^n \,\middle|\, \mathbf{v}_h|_T \in \mathbb{P}_p(T) \; \forall T \in \mathcal{T} \right\}, \\
\Phi_h^\varphi &:= \left\{ \phi_h \in L^2(\Omega) \,\middle|\, \phi_h|_T \in \mathbb{P}_q(T) \; \forall T \in \mathcal{T} \right\}, \\
\Phi_h^p &:= \left\{ \phi_h \in L^2(\Omega) \,\middle|\, \psi_h|_T \in \mathbb{P}_r(T) \; \forall T \in \mathcal{T} \right\}, \text{ and} \\
\Phi_h^{p_\Gamma} &:= \left\{ \psi_{\Gamma,h} \in L^2(\Gamma^0) \,\middle|\, \psi_{\Gamma,h}|_T \in \mathbb{P}_r(T) \; \forall T \in \mathcal{T}_\Gamma \right\},
\end{aligned}$$

where $\mathbb{P}_p(T)$ denotes the set of polynomials on T with degree $\leq p$.

For any $\psi \in \Phi_h^p$ (or the other spaces, respectively) we denote the two values on each side of a facet $F \in \mathscr{F}$ by ψ^+ and ψ^-. Here, the normal $\mathbf{n}$ of facet F is assumed to point from the + to the − side, and we also denote $\mathbf{n}^+ = \mathbf{n}$ and $\mathbf{n}^- = -\mathbf{n}$. The restriction to specific sides of a facet is denoted with the ± superscript. We use the jump operators as defined in (5.11) and the average operator defined as

$$\{\!\{\psi\}\!\} := \frac{1}{2}(\psi^+ + \psi^-).$$

A similar notation can be applied to the traces of bulk functions evaluated on fracture elements $T_\Gamma \in \mathscr{T}_\Gamma$ as each fracture element can be identified with a facet $F_\Gamma \in \mathscr{F}_\Gamma$.

5.4.2 Discontinuous Galerkin Formulation

Let us state the incomplete interior penalty discontinuous Galerkin (IIPDG) forms of our Galerkin finite element (semi-)discretization. For a detailed background on the discontinuous Galerkin method we refer to [29].

The IIPDG forms of our Galerkin finite element (semi-)discretization for our mixed-dimensional phase-field model read

$$\begin{aligned} B_u(\mathbf{u},\mathbf{v}) := &\int_{\mathscr{T}} (\tilde{\sigma}(\mathbf{u},\varphi) - \alpha p\mathbf{I}) \,:\, \epsilon(\mathbf{v})\, dx \\ &+ \int_{\mathscr{F}\setminus\mathscr{F}_\Gamma} \frac{\beta_u}{h}[\![\mathbf{u}]\!]\cdot[\![\mathbf{v}]\!] - \{\!\{(\tilde{\sigma}(\mathbf{u},\varphi) - \alpha p\mathbf{I})\mathbf{n}\}\!\}\cdot[\![\mathbf{v}]\!]\, ds \\ &+ \int_{\mathscr{F}_\mathscr{D}} \frac{\beta_u}{h}(\mathbf{u}-\mathbf{u}_D)\cdot\mathbf{v} - ((\tilde{\sigma}(\mathbf{u},\varphi) - \alpha p\mathbf{I})\mathbf{n})\cdot\mathbf{v}\, ds, \\ &+ \int_{\mathscr{F}_\Gamma} \left(p_\Gamma - \frac{p_\Gamma^2}{2M}\right)\mathbf{n}^+\cdot\mathbf{v}^+ + \left(p_\Gamma - \frac{p_\Gamma^2}{2M}\right)\mathbf{n}^-\cdot\mathbf{v}^-\, ds, \end{aligned} \tag{5.31}$$

$$B_\varphi(\varphi,\phi) \coloneqq \int_{\mathscr{T}} -\frac{g_c}{l}(1-\varphi)\phi + g_c l\nabla\varphi\cdot\nabla\phi + A'(\varphi)\Psi^+(\mathbf{u})\phi\,dx + \int_{\mathscr{F}} \frac{\beta_\varphi}{h}[\![\varphi]\!][\![\phi]\!] - \{\!\{g_c l\nabla\varphi\cdot\mathbf{n}\}\!\}[\![\phi]\!]\,ds, \tag{5.32}$$

$$B_p(p,\psi) \coloneqq \int_{\mathscr{T}} \left(\frac{p}{M} + \alpha\operatorname{div}\mathbf{u}\right)_t\psi + \left(\frac{\mathbf{K}}{\eta}\nabla p\right)\cdot\nabla\psi\,dx + \int_{\mathscr{F}\setminus\mathscr{F}_\Gamma} \frac{\beta_p}{h}[\![p]\!][\![\psi]\!] - \{\!\{\frac{\mathbf{K}}{\eta}\nabla p\}\!\}\cdot\mathbf{n}[\![\psi]\!]\,ds + \int_{\mathscr{F}_\Gamma} C(p^+,p_\Gamma,\mathbf{u})\psi^+ + C(p^-,p_\Gamma,\mathbf{u})\psi^-\,ds - \int_{\mathscr{T}} q\psi\,dx, \tag{5.33}$$

$$B_{p_\Gamma}(p_\Gamma,\psi_\Gamma) \coloneqq \int_{\mathscr{T}_\Gamma} d(\mathbf{u})\left(\frac{p_\Gamma}{M}\right)_t\psi_\Gamma + d(\mathbf{u})\frac{K_\tau^f}{\eta}\nabla p_\Gamma\cdot\nabla\psi_\Gamma + d(\mathbf{u})_t\psi_\Gamma\,dx + \int_{\mathscr{F}^\Gamma} \frac{\beta_{p_\Gamma}}{h_\Gamma}[\![p_\Gamma]\!][\![\psi_\Gamma]\!] - \{\!\{d(\mathbf{u})\frac{K_\tau^f}{\eta}\nabla p_\Gamma\}\!\}\cdot\mathbf{n}[\![\psi_\Gamma]\!]\,ds - \int_{\mathscr{T}_\Gamma} C(p^+,p_\Gamma,\mathbf{u})\psi_\Gamma + C(p^-,p_\Gamma,\mathbf{u})\psi_\Gamma\,dx - \int_{\mathscr{T}_\Gamma} d(\mathbf{u})q\psi_\Gamma\,dx. \tag{5.34}$$

Here, h (resp., h_Γ) denotes the characteristic size of the two cells adjacent to the corresponding facet. The penalty parameters β_u, β_φ, β_p and β_{p_Γ} have to be chosen sufficiently large to ensure well-posedness of the scheme. We choose

$$\beta_u = (\lambda+2\mu)\beta_0,\quad \beta_\varphi = g_c l\beta_0,\quad \beta_p = \frac{\mathbf{n}^\top\mathbf{K}\mathbf{n}}{\eta}\beta_0,\quad \beta_{p_\Gamma} = d(\mathbf{u})\frac{K_\tau^f}{\eta}\beta_0,$$

where $\beta_0 = 100$. In the formulation above, we use $C(p,p_\Gamma,\mathbf{u})$ as defined in (5.22).

The time-derivative is discretized using a backward Euler method.

5.4.3 Iterative Solution Strategy

Due to numerical difficulties related to the indefiniteness of the Jacobian of the non-linear system (5.15)-(5.17), cf. [53], we do not solve it monolithically. Instead, we apply an iterative solution strategy between displacement/pressure equations and the phase-field equation that reads as follows.

1. For given φ_h, find $\mathbf{u}_h \in \Phi_h^u$, $p_h \in \Phi_h^p$ and $p_{\Gamma,h} \in \Phi_{\Gamma,h}^p$ s.t.

$$B_u(\mathbf{u}_h, \mathbf{v}) + B_p(p_h, \psi) + B_{p_\Gamma}(p_{\Gamma,h}, \psi_\Gamma) = 0,$$

   for all $\mathbf{v} \in \Phi_h^u$, $\psi \in \Phi_h^p$ and $\psi_\Gamma \in \Phi^{p_{\Gamma,h}}$.

2. For given $\mathbf{u}_h$, p_h and $p_{\Gamma,h}$, find $\varphi_h \in \Phi_h^\varphi$,

$$B_\varphi(\varphi_h, \phi) = 0,$$

   for all $\phi \in \Phi_h^\varphi$.

3. Repeat step 1 and 2 until convergence.

In our numerical examples, we choose the difference between two iterates of φ_h measured in the L^2-norm as indicator of convergence.

5.4.4 Tracking the Sharp Fracture

In our numerical approach, as already mentioned in Section 5.3.7, we reconstruct the updated sharp fracture that is approximated by the diffuse phase-field rep-

resentation. Therefore, the orders of the spatial discretization of displacement, phase-field and pressure are chosen as

$$p = 2, \quad q = 1, \quad r = 1,$$

because we observe that this choice (in particular, second order displacement, first order phase-field) allows the fracture to propagate along facets of the mesh. Choosing a second order displacement leads to a linear elastic energy $\Psi^+(\mathbf{u})$ in equation (5.16) and, therefore, the phase-field does not necessarily decrease constantly in cells, cf. Figure 5.4.

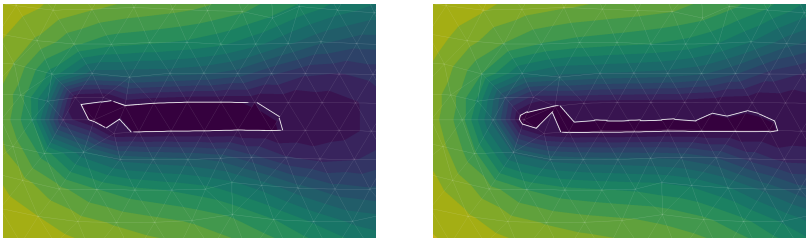

Figure 5.4: The phase-field solution around a propagating fracture tip for different discretization orders of the displacement. The white line shows the $\varphi = 0.01$ contour line that will be used as threshold to add new facets. Left: First order displacement. Right: Second order displacement.

Then, during time stepping, we update the set of fracture facets $\mathcal{F}_\Gamma$. If the value of the phase-field variable at the center of a facet falls below the threshold $\varphi_0 = 0.01$, we add this facet to the set of fracture facets $\mathcal{F}_\Gamma$. Thereby, the discontinuity of the displacement follows the propagation path, and the flow model is incorporated in the propagated fracture. We remark that this approach automatically captures topology changes like joining fractures and, we anticipate due to the nature of our method, also bifurcations. However, we introduce a rather strong mesh-dependency. Note that we only add (and do not remove) new facets to the fracture network which implicitly makes the fracture propagation an irreversible process.

It is important to ensure that the total energy of the system decreases over time, in particular, when we add facets to the fracture. We will investigate this behavior in numerical examples below, cf. Section 5.5.

Table 5.1: Parameters of the numerical experiments.

Symbol	Quantity	Value	Unit
E	Young's modulus	10^8	Pa
ν	Poisson's ratio	0.2	-
M	Biot's modulus	10^8	Pa
α	Biot coefficient	1	-
η	viscosity	10^{-3}	$\mathrm{kg\,m^{-1}\,s^{-1}}$
$\mathbf{K}$	Bulk permeability	$10^{-12}\,\mathbf{I}$	$\mathrm{m^2}$
g_c	Griffith's critical energy	10^3	$\mathrm{J\,m^{-1}}$
d_0	residual aperture	10^{-14}	m
β_0	penalty parameter	100	-
k	residual resistance	10^{-12}	-
p_{inj}	injection pressure	5×10^{-3}	$\mathrm{m^3\,s^{-1}}$
d_0	point source distribution	10^3	$\mathrm{m^{-2}}$
x_0	point source position	$(2, 2)$	m
Δt	time step size	0.1	s
T	end time	10	s
h	mesh size at boundary	0.2	m
h_f	mesh size at fracture	0.01	m
l	phase-field parameter	$2h_f$	m

5.4.5 Implementation

The proposed discontinuous Galerkin discretization has been implemented within the open source framework DUNE [11] on the basis of the discretization module Dune-Fem [27] and our grid implementation Dune-MMesh [21]. The

bilinear forms stated in (5.31)-(5.34) can be directly written in Python using UFL [5] and the Dune-Fem framework generates the corresponding Galerkin schemes as efficient C++ code. The nonlinear problems are solved by a Newton method together with the direct linear solver UMFPack. All conforming triangular grids are generated using the Python API of `Gmsh` [35].

The tools necessary tools to solve the mixed dimensional problem are available in our grid implementation Dune-MMesh. First of all, Dune-MMesh can expose a set of facets of the bulk grid (those which represent the fracture) as a separate computational surface grid, and on this grid, the lower-dimensional forms can also be stated using UFL. Second, Dune-MMesh provides trace operators to access bulk discrete functions from the surface grid, and vice versa, in order to implement the coupling terms. Finally, a specialized Newton method is provided that assembles the coupling blocks of the Jacobian by finite differences and, therefore, makes a mixed-dimensional monolithic solution algorithm available. The source code to reproduce the results presented in Section 5.5 can be found in a public repository[2].

5.5 Numerical Experiments

In this section, we consider two numerical experiments to show the performance of the mixed-dimensional phase-field model (5.15)-(5.25). The setups are inspired by the test cases in [53] and [48], and we consider their results as reference.

5.5.1 Horizontal Fracture

In the first numerical experiment, we investigate the propagation of a single horizontal fracture. Consider a domain $\mathscr{D} = (0, 4)^2\text{m}$ with a single, horizontal fracture $\Gamma^0 = (1.8, 2.2) \times \{2\}\text{m}$ located in the center of the domain, as depicted in

[2]https://github.com/samuelburbulla/pfdfm

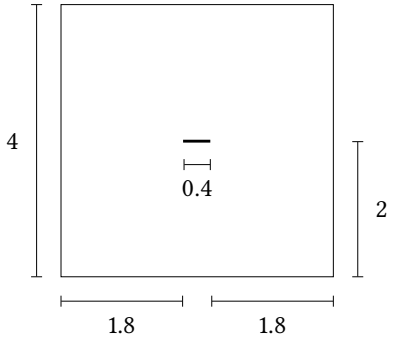

*Figure 5.5: Geometrical setting of first numerical experiment with a centered horizontal fracture. Lengths in [*m*].*

Figure 5.5. The fracture is pressurized by a point source injection that is modeled by

$$q(\mathbf{x}) = p_{\text{inj}} \frac{d_0}{\pi} \exp(-d_0 \|\mathbf{x} - \mathbf{x}_0\|^2). \tag{5.35}$$

All physical and all discretization parameters of our examples are listed in Table 5.1 and are taken from [48]. We will investigate the corresponding displacement, pressure and phase-field distributions, and study some properties of our method.

Our findings for the first example can be observed in Figures 5.7-5.11. The domain Ω is warped by the displacement $3\mathbf{u}$ to visualize the opening of the fracture. The distribution of vertical displacement is displayed in Figure 5.7 and shows the typical elliptical opening of the fracture. The pressure distribution visualized in Figure 5.8 follows, as expected, the propagating fracture thanks to its higher permeability. Here, also the lower-dimensional domain Γ is plotted. We obtain negative pressure values at the tips of the fracture which have been also observed in literature [48, 53]. In Figure 5.9, the phase-field is visualized and indicates the propagation of the fracture tips.

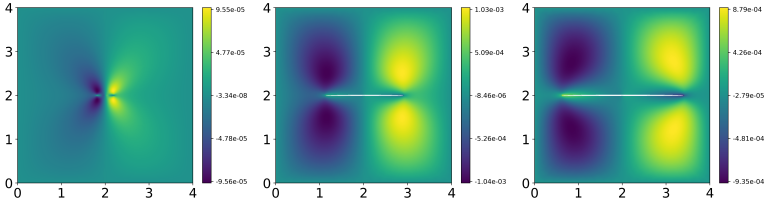

Figure 5.6: Horizontal displacement $\mathbf{u}_x$ *[*m*] for* $t \in \{0.1, 5, 10\}$s.

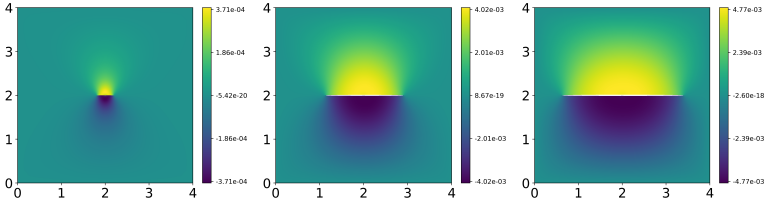

Figure 5.7: Vertical displacement $\mathbf{u}_y$ *[*m*] for* $t \in \{0.1, 5, 10\}$s.

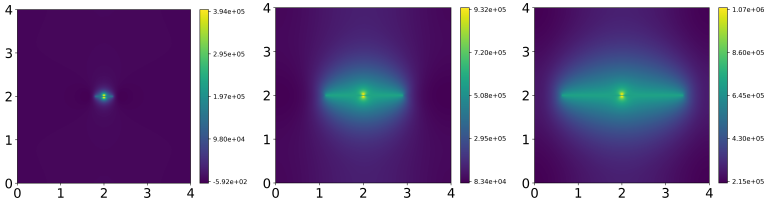

Figure 5.8: Pressure p *[*Pa*] for* $t \in \{0.1, 5, 10\}$s.

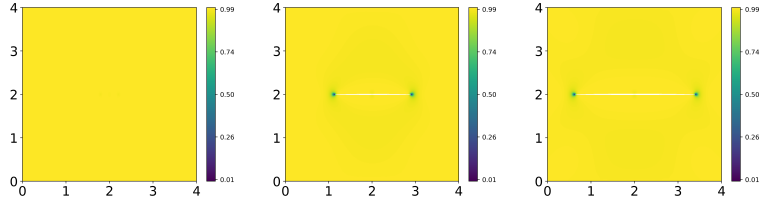

Figure 5.9: Phase-field φ *for* $t \in \{0.1, 5, 10\}$s.

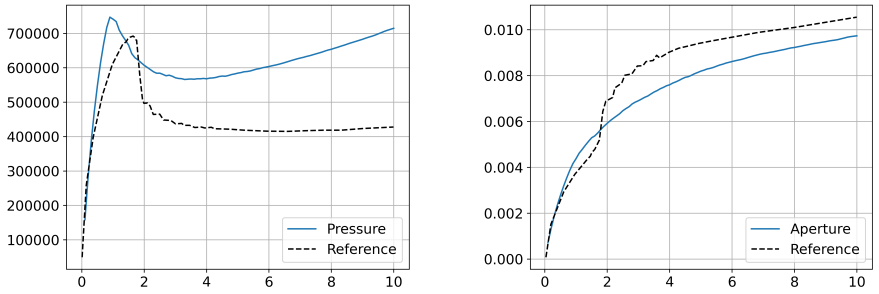

*Figure 5.10: The maximum pressure [*Pa*] and the maximum fracture's aperture [*m*] plotted over time* $t \in [0, 10]$s. *The dashed line shows the reference solution taken from [48] (Example 1).*

In order to observe the maximum pressure and aperture of the fracture over time, we plotted these values in Figure 5.10. In Figure 5.11 (left), we compare the propagation speed of the fracture for three values of $l \in \{0.08, 0.04, 0.02\}$ and observe that it is independent of l and, as we choose $l = 2h_f$, the propagation gets smoother under mesh refinement. The number of iterations between the poro-elastic problem and the phase-field equation can be found in Figure 5.12.

A quantitative comparison shows that our method provides similar values as results in literature, e.g., see [48] (Example 1). In our computation, the fracture's propagation starts at around $t = 1.5$s which is similar to around $t = 1.8$s in the aforementioned reference, see Figure 5.10 (left). The maximum pressure value reaches 750000Pa, while it lies between 600000Pa and 700000Pa in the reference. Further, the maximal fracture aperture approaches 0.01m in both cases, compare Figure 5.10 (right), what suggests that the displacement values are similar. A difference can be observed in the behavior of the maximum pressure where our computations suggest an increase starting from $t = 4$s instead of a plateau-like value in the reference solution. The difference probably comes from the fact that the reference applies the source term exclusively within the diffuse fracture and

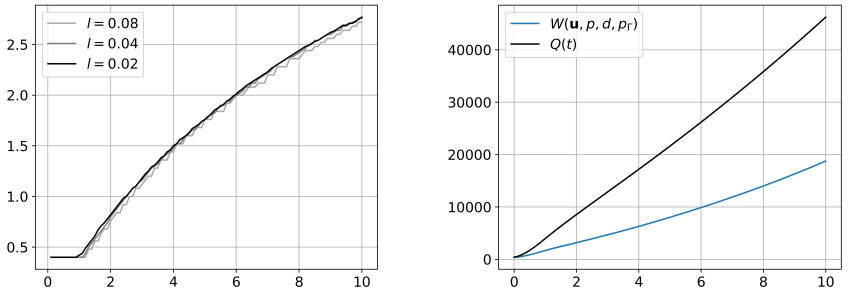

*Figure 5.11: The length of the fracture [*m*] for different values of l and the free energy W compared to the accumulated sources $Q(t)$ for $t \in [0, 10]$*s.

computes the aperture implicitly by a post-processing routine.

Moreover, in Figure 5.11 (right) we visualize the free energy in comparison to the accumulated sources

$$Q(t) := \int_0^t \int_\Omega pq \, dx + \int_{\Gamma^0} d(\mathbf{u}) p_\Gamma q \, dx \, dt.$$

Note that the time derivative of $W(\mathbf{u}, p, \varphi, p_\Gamma)$ is smaller than the one of the accumulated source term on the right hand side of (5.30). This is in accordance with the statement in Theorem 5.1.

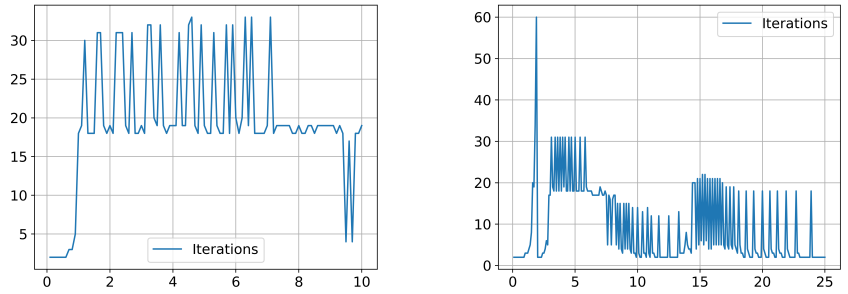

Figure 5.12: The number of iterations between poro-elastic problem and phase-field equation for $t \in [0, 10]$s. Each iteration contains about 2-5 Newton iterations. Left: Example 1. Right: Example 2.

5.5.2 Two Joining Fractures

Consider the domain $\mathscr{D} = (0, 4)^2$m with two fractures $\Gamma^0 = \Gamma_1 \cup \Gamma_2$ where $\Gamma_1 = (1.8, 2.4) \times \{2\}$m and $\Gamma_2 = \{2.6\} \times (1.8, 2.2)$m, cf. Figure 5.13. All physical parameters are chosen as in the first numerical example, and we use the same source term to pressurize the horizontally aligned fracture.

The distribution of the displacement is displayed in Figures 5.14-5.15. The pressure distribution and the phase-field are visualized in Figures 5.16-5.17 respectively.

Due to propagation, the two fractures join and create a connected fracture network. From the tips of the vertical part propagation continues in a diagonal direction as observed in [53]. However, unlike this previous work, we get an explicit geometrical representation of the developed fracture network and we claim that the solution of the flow problem is more accurate. It is hard to compare both modeling approaches in terms of computational time, but we want to

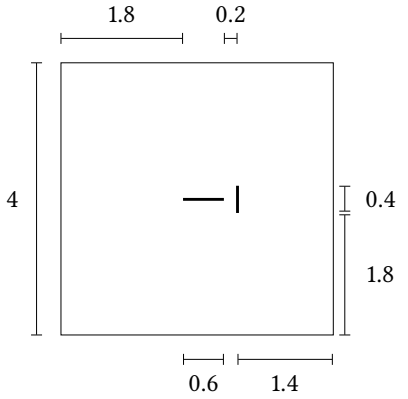

*Figure 5.13: Geometrical setting of the second numerical experiment with two fractures that are supposed to join. Lengths in [*m*].*

highlight that in our approach grid refinement could be restricted to the area around the tips where higher resolution for the phase-field is necessary.

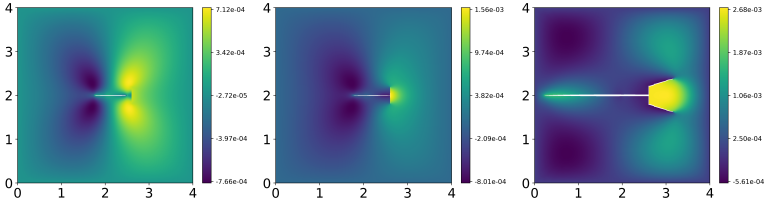

Figure 5.14: Horizontal displacement $\mathbf{u}_x$ *[*m*] for* $t \in \{1.8, 1.9, 25\}$s.

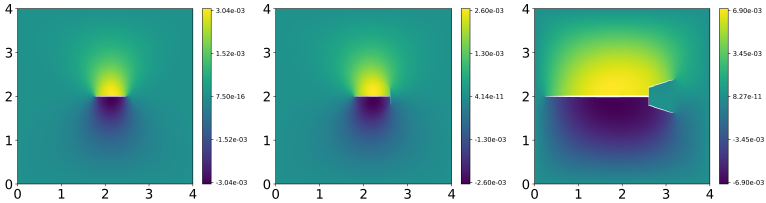

Figure 5.15: Vertical displacement $\mathbf{u}_y$ *[*m*] for* $t \in \{1.8, 1.9, 25\}$s.

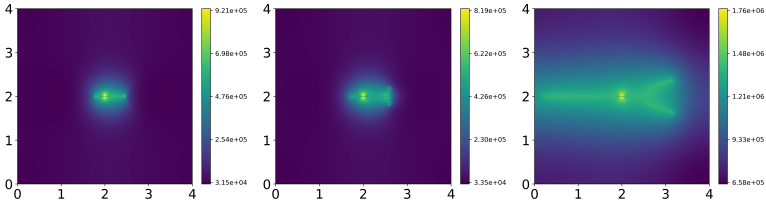

Figure 5.16: Pressure p *[*Pa*] for* $t \in \{1.8, 1.9, 25\}$s.

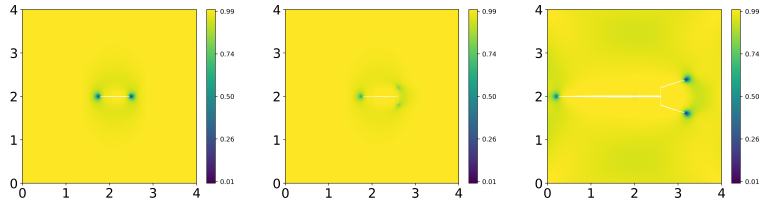

Figure 5.17: Phase-field φ *for* $t \in \{1.8, 1.9, 25\}$s.

Conclusion and Outlook

6

6.1 Conclusion

In this work, we presented new approaches to the mixed-dimensional modeling of flow in fractured and dynamically fracturing porous media.

We started with an overview of our grid module Dune-MMesh that is tailored for the implementation of mixed-dimensional models. The Dune-MMesh module settles the foundations of a completely new way to implement mixed-dimensional models. Furthermore, it creates new capabilities for numerical methods with conforming moving interfaces surrounded by a re-meshing triangulation. A set of examples has been presented including mixed-dimensional problems, the finite-volume moving-mesh algorithm and some flow scenarios in highly branched fractured porous media.

In Chapter 3, we presented the derivation of a dimensionally reduced model for two-phase flow in fractured porous media that takes into account time-dependent fracture growth and changing apertures. The finite-volume moving-mesh algorithm has been proposed to capture dynamic fracture propagation by an explicit geometrical representation of the fracture geometries. The new method is able to track both the movement of lower-dimensional and full-dimensional fractures. Therefore, it has been used to verify the newly derived

model in several benchmark cases by comparing solutions of the reduced and the full-dimensional fracture representations. The solutions showed good agreement and this indicated the validity of the reduced model and the finite-volume moving-mesh algorithm.

In Chapter 4, we derived a new model for single-phase flow in fractured porous media where fractures with non-constant aperture are represented as lower-dimensional interfaces. The model accounts for asymmetric fractures with spatially varying aperture and can be viewed as a generalization of a previous model [51]. The new model allows to study rough-surfaced, possibly curvilinear real-world fracture geometries. In various numerical experiments based on a new mixed-dimensional discontinuous Galerkin method we found a remarkable agreement between the solution of the new interface model and a reference solution. Moreover, it has been observed that neglecting any of the terms in the model associated with a varying fracture aperture can substantially impair the accuracy of the solution.

Finally, in Chapter 5, we presented a new mixed-dimensional phase-field model for modeling fracture propagation in poro-elastic media. Our new model combines ideas from discrete fracture modeling and phase-field models for fracture propagation. The advantage of this new modeling approach is that we have an explicit representation of the fracture network while preserving the geometric flexibility of the phase-field model. It has been proven that the new model is thermodynamically consistent. We proposed a mixed-dimensional interior penalty discontinuous Galerkin discretization on the basis of a fully conforming discretization. The mesh dependency introduced in the combined approach was shown to decrease refining the mesh. Finally, we applied the method to some commonly used fracture propagation scenarios and observed that our numerical solutions reproduce the expected behavior known from literature.

6.2 Outlook

In future work, the proposed models and methods could be applied to more complex flow and fracture propagation scenarios, and they could also be extended to include additional physical effects. Moreover, the analysis of most of the presented models remains open and might be investigated in future work.

Extensions of the proposed models include heterogeneous flow systems with different flow models for bulk and fracture domains, e.g., incorporating the roughness of the fracture walls, using free-flow regimes inside the fracture, or adding thermal transport or precipitation effects. The additional terms derived in Chapter 4 accounting for non-constant apertures can also be included in the model equations for two-phase flow or for poro-elastic media, where the fracture aperture is non-constant in general. Further, the junctions of fractures within the lower-dimensional fracture network represent an issue that can be investigated further. We did not care about coupling conditions at junctions of the fracture network (except once in Chapter 3), as we get mass conservation implicitly from our discontinuous Galerkin discretization. However, non-trivial conditions have been proposed to coupled unknowns at a junction of a network depending on the physical model, and further investigation could focus on the case of intersecting fractures with different physical properties.

The presented methods might also be applied to complex (three-dimensional) real-world scenarios with time-dependent flow problems and dynamically propagating fractures. However, especially considering three-dimensional computations, the performance should be improved. The two-dimensional examples presented in Chapter 5 with several hundred thousands of degrees of freedoms and several hundred time steps already take hours on a single-core machine, and it might be of interest to see more complex fracture propagation patterns, e.g., as depicted in Figure 1.2. For instance, in order to significantly improve the performance of the solver, one could develop an MPI parallel version of Dune-MMesh. Initial work in this direction has been done, but the full functionality of Dune-MMesh, especially the monolithic solving routine and re-meshing, is

non-trivial in parallel and not supported yet. Further, extended continuous finite element spaces with additional degrees of freedoms just at the interface could be implemented as this would reduce the total number of degrees in comparison to the discontinuous discretization. Finally, one could choose suitable iterative solvers for the sub-problems in bulk and lower-dimensional domain and splitting algorithms like fixed-stress splitting to solve the (non-)linear systems more efficiently.

In any case, Dune-MMesh is well-suited for the implementation of discretizations for any complex mixed-dimensional model or for any mathematical problem with a moving interface and we are looking forward to see how others will use this resource.

Bibliography

[1] P. M. Adler, J.-F. Thovert, and V. V. Mourzenko. *Fractured porous media*. Oxford University Press, 2013.

[2] J. Aghili, J.-R. de Dreuzy, R. Masson, and L. Trenty. *A hybrid-dimensional compositional two-phase flow model in fractured porous media with phase transitions and Fickian diffusion*. J. Comput. Phys. 441 (2021). DOI: 10.1016/j.jcp.2021.110452.

[3] E. Ahmed, J. Jaffré, and J. E. Roberts. *A reduced fracture model for two-phase flow with different rock types*. Math. Comput. Simul. 137 (2017). DOI: 10.1016/j.matcom.2016.10.005.

[4] C. Alboin, J. Jaffré, J. E. Roberts, and C. Serres. *Modeling fractures as interfaces for flow and transport in porous media. Fluid flow and transport in porous media: mathematical and numerical treatment (South Hadley, MA, 2001)*. Vol. 295. Amer. Math. Soc., Providence, RI, 2002. DOI: 10.1090/conm/295/04999.

[5] M. S. Alnæs, A. Logg, K. B. Ølgaard, M. E. Rognes, and G. N. Wells. *Unified form language: a domain-specific language for weak formulations of partial differential equations*. ACM Trans. Math. Softw. 40.2 (2014). DOI: 10.1145/2566630.

[6] L. Ambrosio and V. M. Tortorelli. *Approximation of functional depending on jumps by elliptic functional via t-convergence*. Comm. Pure Appl. Math. 43.8 (1990). DOI: 10.1002/CPA.3160430805.

[7] H. Amor, J.-J. Marigo, and C. Maurini. *Regularized formulation of the variational brittle fracture with unilateral contact: numerical experiments.* J. Mech. Phys. Sol. 57.8 (2009). DOI: 10.1016/j.jmps.2009.04.011.

[8] P. Andersen and S. Evje. *A model for reactive flow in fractured porous media.* Chem. Eng. Sci. 145 (2016). DOI: 10.1016/j.ces.2016.02.008.

[9] P. Angot, F. Boyer, and F. Hubert. *Asymptotic and numerical modelling of flows in fractured porous media.* ESAIM: Math. Model. Numer. Anal. 43.2 (2009). DOI: 10.1051/m2an/2008052.

[10] P. Antonietti, C. Facciolà, A. Russo, and M. Verani. *Discontinuous Galerkin approximation of flows in fractured porous media on polytopic grids.* SIAM J. Sci. Comput. 41 (2019). DOI: 10.1137/17M1138194.

[11] P. Bastian, M. Blatt, A. Dedner, N.-A. Dreier, C. Engwer, R. Fritze, C. Gräser, C. Grüninger, D. Kempf, R. Klöfkorn, M. Ohlberger, and O. Sander. *The dune framework: basic concepts and recent developments.* Comput. Math. Appl. 81 (2021). DOI: 10.1016/j.camwa.2020.06.007.

[12] J. Bear, C.-F. Tsang, and G. De Marsily. *Flow and contaminant transport in fractured rock.* Academic Press, 2012.

[13] I. Berre, W. M. Boon, B. Flemisch, A. Fumagalli, D. Gläser, E. Keilegavlen, A. Scotti, I. Stefansson, A. Tatomir, K. Brenner, S. Burbulla, P. Devloo, O. Duran, M. Favino, J. Hennicker, I. Lee, K. Lipnikov, R. Masson, K. Mosthaf, M. G. C. Nestola, C. Ni, K. Nikitin, P. Schädle, D. Svyatskiy, R. Yanbarisov, and P. Zulian. *Verification benchmarks for single-phase flow in three-dimensional fractured porous media.* Adv. Water Res. 147 (2021). DOI: 10.1016/j.advwatres.2020.103759.

[14] I. Berre, F. Doster, and E. Keilegavlen. *Flow in fractured porous media: a review of conceptual models and discretization approaches.* Transp. Porous Med. 130 (1 2019). DOI: 10.1007/s11242-018-1171-6.

[15] M. Biot and I. Tolstoy. *Acoustics, elasticity, and thermodynamics of porous media. Twenty-one papers by M.A. Biot.* Acoustical Society of America, New York, 1992.

[16] W. M. Boon, J. M. Nordbotten, and I. Yotov. *Robust discretization of flow in fractured porous media.* SIAM J. Num. Anal. 56.4 (2018). DOI: 10.1137/17m1139102.

[17] B. Bourdin, G. Francfort, and J. Marigo. *The variational approach to fracture.* J. Elast. 91 (2008). DOI: 10.1007/s10659-007-9107-3.

[18] K. Brenner, J. Hennicker, R. Masson, and P. Samier. *Hybrid-dimensional modelling of two-phase flow through fractured porous media with enhanced matrix fracture transmission conditions.* J. Comput. Phys. 357 (2018). DOI: 10.1016/j.jcp.2017.12.003.

[19] M. Bukac, I. Yotov, and P. Zunino. *Dimensional model reduction for flow through fractures in poroelastic media.* ESAIM: M2AN 51.4 (2017). DOI: 10.1051/m2an/2016069.

[20] S. Burbulla. *Replication Data for: A Finite-Volume Moving-Mesh Method for Two-phase Flow in Fracturing Porous Media.* 2021. DOI: 10.18419/darus-1712.

[21] S. Burbulla, A. Dedner, M. Hörl, and C. Rohde. *Dune-MMesh: the Dune grid module for moving interfaces.* J. Open Source Softw. 7.74 (2022). DOI: 10.21105/joss.03959.

[22] S. Burbulla, M. Hörl, and C. Rohde. *Flow in porous media with fractures of varying aperture.* arXiv (2022). DOI: 10.48550/ARXIV.2207.09301.

[23] S. Burbulla and C. Rohde. *A fully conforming finite volume approach to two-phase flow in fractured porous media.* Fvca ix - meth. theor. asp. ex. Ed. by R. Klöfkorn, E. Keilegavlen, F. A. Radu, and J. Fuhrmann. Springer International Publishing, 2020. DOI: 10.1007/978-3-030-43651-3_51.

[24] S. Burbulla and C. Rohde. *A finite-volume moving-mesh method for two-phase flow in dynamically fracturing porous media.* J. Comput. Phys. 458 (2022). DOI: 10.1016/j.jcp.2022.111031.

[25] C. Chalons, C. Rohde, and M. Wiebe. *A finite volume method for under-compressive shock waves in two space dimensions.* ESAIM: Math. Model. Numer. Anal. 51.5 (2017). DOI: 10.1051/m2an/2017027.

[26] K. Deckelnick, G. Dziuk, and C. M. Elliott. *Computation of geometric partial differential equations and mean curvature flow.* Acta Numerica 14 (2005). DOI: 10.1017/S0962492904000224.

[27] A. Dedner, M. Nolte, and R. Klöfkorn. *Python bindings for the dune-fem module.* Zenodo (2020). DOI: 10.5281/zenodo.3706994.

[28] A. Dedner, R. Klöfkorn, M. Nolte, and M. Ohlberger. *A generic interface for parallel and adaptive discretization schemes: abstraction principles and the DUNE-FEM module.* Comput. 90 (2010). DOI: 10.1007/s00607-010-0110-3.

[29] V. Dolejší and M. Feistauer. *Discontinuous Galerkin method - analysis and applications to compressible flow.* Springer, Cham, 2015. DOI: 10.1007/978-3-319-19267-3.

[30] R. Eymard, T. Gallouët, and R. Herbin. *Finite volume methods.* Handb. Numer. Anal. 7 (2000).

[31] B. Flemisch, A. Fumagalli, and A. Scotti. *A review of the XFEM-based approximation of flow in fractured porous media. Advances in discretization methods.* Vol. 12. Springer, [Cham], 2016. DOI: 10.1007/978-3-319-41246-7_3.

[32] A. Fumagalli and A. Scotti. *A numerical method for two-phase flow in fractured porous media with non-matching grids.* Adv. Water Res. 62 (2013). DOI: 10.1016/j.advwatres.2013.04.001.

[33] A. Fumagalli and A. Scotti. *A mathematical model for thermal single-phase flow and reactive transport in fractured porous media.* J. Comput. Phys. 434 (2021). DOI: 10.1016/j.jcp.2021.110205.

[34] J. Gerstenberger, S. Burbulla, and D. Kröner. *Discontinuous Galerkin method for incompressible two-phase flows.* FVCA IX - Meth. Theor. Asp. Ex. (2020). DOI: 10.1007/978-3-030-43651-3_64.

[35] C. Geuzaine and J.-F. Remacle. *Gmsh: a three-dimensional finite element mesh generator with built-in pre- and post-processing facilities.* Int. J. Num. Meth. Eng. 79.11 (2009). DOI: 10.1002/nme.2579.

[36] B. Giovanardi, A. Scotti, and L. Formaggia. *A hybrid XFEM–phase field (Xfield) method for crack propagation in brittle elastic materials.* Comput, Methods Appl. Mech. Eng. 320 (2017). DOI: 10.1016/j.cma.2017.03.039.

[37] D. Gläser, R. Helmig, B. Flemisch, and H. Class. *A discrete fracture model for two-phase flow in fractured porous media.* Adv. Water Res. 110 (2017). DOI: 10.1016/j.advwatres.2017.10.031.

[38] A. Griffith. *The phenomena of rupture and flow in solids.* Philos. T. Roy. Soc. A.CCXXI-A (1921). DOI: 10.1098/rsta.1921.0006.

[39] A. Harten and J. M. Hyman. *Self adjusting grid methods for one-dimensional hyperbolic conservation laws.* J. Comput. Phys. 50.2 (1983). DOI: 10.1016/0021-9991(83)90066-9.

[40] T. Heister, M. F. Wheeler, and T. Wick. *A primal-dual active set method and predictor-corrector mesh adaptivity for computing fracture propagation using a phase-field approach.* Comput. Meth. Appl. Mech. Eng. 290 (2015). DOI: 10.1016/j.cma.2015.03.009.

[41] R. Helmig. *Multiphase flow and transport processes in the subsurface: a contribution to the modeling of hydrosystems.* Springer-Verlag, 1997.

[42] M. Hörl, S. Burbulla, and C. Rohde. *The mmdgpy Python Package: Source Code and Replication Data for "Flow in Porous Media with Fractures of Varying Aperture".* https://github.com/maximilianhoerl/mmdgpy (2022). DOI: 10.18419/darus-3012.

[43] J. Jaffré, M. Mnejja, and J. Roberts. *A discrete fracture model for two-phase flow with matrix-fracture interaction.* Proc. Comp. Sc. 4 (2011). DOI: 10.1016/j.procs.2011.04.102.

[44] T. Koch, D. Gläser, K. Weishaupt, S. Ackermann, M. Beck, B. Becker, S. Burbulla, H. Class, E. Coltman, S. Emmert, T. Fetzer, C. Grüninger, K. Heck, J. Hommel, T. Kurz, M. Lipp, F. Mohammadi, S. Scherrer, M. Schneider, G. Seitz, L. Stadler, M. Utz, F. Weinhardt, and B. Flemisch. *Dumux 3 – an open-source simulator for solving flow and transport problems in porous media with a focus on model coupling.* Comput. & Math. Appl. 81 (2021). DOI: 10.1016/j.camwa.2020.02.012.

[45] M. Köppel, V. Martin, J. Jaffré, and J. E. Roberts. *A Lagrange multiplier method for a discrete fracture model for flow in porous media.* Comput. Geosci. 23.2 (2019). DOI: 10.1007/s10596-018-9779-8.

[46] D. Kröner. *Numerical schemes for conservation laws.* Wiley-Teubner series in advances in numerical mathematics. Wiley-Teubner, 1997.

[47] K. Kumar, F. List, I. S. Pop, and F. A. Radu. *Formal upscaling and numerical validation of unsaturated flow models in fractured porous media.* J. Comput. Phys. 407 (2020). DOI: 10.1016/j.jcp.2019.109138.

[48] S. Lee, A. Mikelić, M. F. Wheeler, and T. Wick. *Phase-field modeling of two phase fluid filled fractures in a poroelastic medium.* Multisc. Model. Simul. 16.4 (2018). DOI: 10.1137/17M1145239.

[49] L. Li and S. Lee H. *Efficient field-scale simulation of black oil in a naturally fractured reservoir through discrete fracture networks and homogenized media.* SPE Reserv. Eval. & Eng. 11.04 (2008). DOI: 10.2118/103901-PA.

[50] F. List, K. Kumar, I. S. Pop, and F. A. Radu. *Rigorous upscaling of unsaturated flow in fractured porous media.* SIAM J. Math. Anal. 52.1 (2020). DOI: 10.1137/18M1203754.

[51] V. Martin, J. Jaffré, and J. Roberts. *Modeling fractures and barriers as interfaces for flow in porous media.* SIAM J. Sci. Comput. 26 (2005). DOI: 10.1137/S1064827503429363.

[52] C. Miehe, F. Welschinger, and M. Hofacker. *Thermodynamically consistent phase-field models of fracture: variational principles and multi-field FE implementations.* Int. J. Num. Meth. Eng. 83.10 (2010). DOI: 10.1002/nme.2861.

[53] A. Mikelić, M. Wheeler, and T. Wick. *Phase-field modeling of a fluid-driven fracture in a poroelastic medium.* Comput. Geosci. 19 (2015). DOI: 10.1007/s10596-015-9532-5.

[54] F. Morales and R. Showalter. *The narrow fracture approximation by channeled flow.* J. Math. Anal. Appl. 365 (2010). DOI: 10.1016/j.jmaa.2009.10.042.

[55] F. Morales and R. Showalter. *Interface approximation of darcy flow in a narrow channel.* Math. Meth. Appl. Sci. 35 (2012). DOI: 10.1002/mma.1555.

[56] P. Olasolo, M. Juárez, M. Morales, S. D´Amico, and I. Liarte. *Enhanced geothermal systems (egs): a review.* Renew. Sustain. Energy Rev. 56 (2016). DOI: 10.1016/j.rser.2015.11.031.

[57] I. Pop, J. Bogers, and K. Kumar. *Analysis and upscaling of a reactive transport model in fractured porous media with nonlinear transmission condition.* Vietn. J. Math. 45 (2017). DOI: 10.1007/s10013-016-0198-7.

[58] J. Prüss, S. Shimizu, and M. Wilke. *Qualitative behaviour of incompressible two-phase flows with phase transitions: the case of non-equal densities.* Commun. Partial Differ. Equ. 39.7 (2014). DOI: 10.1080/03605302.2013.821131.

[59] V. Reichenberger, H. Jakobs, P. Bastian, and R. Helmig. *A mixed-dimensional finite volume method for two-phase flow in fractured porous media.* Adv. Water Res. 29.7 (2006). DOI: 10.1016/j.advwatres.2005.09.001.

[60] S.-N. Roth, P. Léger, and A. Soulaïmani. *Fully-coupled hydro-mechanical cracking using XFEM in 3d for application to complex flow in discontinuities including drainage system.* Comput Methods Appl Mech Eng 370 (2020). DOI: 10.1016/j.cma.2020.113282.

[61] S.-N. Roth, P. Léger, and A. Soulaïmani. *Strongly coupled XFEM formulation for non-planar three-dimensional simulation of hydraulic fracturing with emphasis on concrete dams.* Comput Methods Appl Mech Eng 363 (2020). DOI: 10.1016/j.cma.2020.112899.

[62] M. Sahimi. *Flow and transport in porous media and fractured rock: from classical methods to modern approaches.* John Wiley & Sons, 2011.

[63] T. Sandve, I. Berre, and J. Nordbotten. *An efficient multi-point flux approximation method for discrete fracture–matrix simulations.* J. Comput. Phys. 231.9 (2012). DOI: 10.1016/j.jcp.2012.01.023.

[64] R. Showalter. *Diffusion in poro-elastic media.* J. Math. Anal. Appl 251.1 (2000). DOI: https://doi.org/10.1006/jmaa.2000.7048.

[65] I. Stefansson, I. Berre, and E. Keilegavlen. *A fully coupled numerical model of thermo-hydro-mechanical processes and fracture contact mechanics in porous media.* Comput. Meth. Appl. Mech. Eng. 386 (2021). DOI: 10.1016/j.cma.2021.114122.

[66] I. Stefansson, E. Keilegavlen, S. Halldórsdóttir, and I. Berre. *Numerical modelling of convection-driven cooling, deformation and fracturing of thermo-poroelastic media.* arXiv:2012.06493 [math.NA] (2020).

[67] M. Ţene, S. Bosma, M. S. Al Kobaisi, and H. Hajibeygi. *Projection-based embedded discrete fracture model (pedfm).* Adv. Water Res. 105 (2017). DOI: 10.1016/j.advwatres.2017.05.009.

[68] The CGAL Project. *CGAL user and reference manual.* 5.3. CGAL Editorial Board, 2021.

Abstract

Modeling flow in dynamically fracturing porous media is of high interest for a wide range of natural and technical applications, for instance, geothermal energy production or carbon capture and storage. In this work, we present new mixed-dimensional models for flow in porous media including fractures with time- and space-dependent geometries. The models are implemented using our new grid implementation Dune-MMesh which is tailored for the discretization of mixed-dimensional partial differential equations with fully conforming interface of codimension one. First, we propose a mixed-dimensional model for capillarity-free two-phase flow in dynamically fracturing porous media. The model is discretized by a fully conforming finite-volume moving-mesh algorithm that explicitly tracks the fracture geometry. Further, generalizing an earlier model for single-phase flow in fractured porous media, we derive a dimensionally reduced model including spatially varying apertures. In several numerical examples, using a mixed-dimensional discontinuous Galerkin discretization, the model demonstrates significant improvements for curvilinear fracture geometries. Finally, we propose a mixed-dimensional phase-field model for fracture propagation in poroelastic media combining discrete fracture and phase-field modeling approaches. The corresponding discontinuous Galerkin discretization tracks the fracture geometry by adding facets to the fracture triangulation according to the phase-field indicator and is validated with results known from literature.